

---

# The interplay between the evolution and dynamics of stellar systems

Pavan Vynatheya

---



München 2024



---

# The interplay between the evolution and dynamics of stellar systems

Pavan Vynatheya

---

Dissertation  
der Fakultät für Physik  
der Ludwig-Maximilians-Universität  
München

vorgelegt von  
Pavan Vynatheya  
aus Bengaluru, Indien

München, den 28.02.2024

Erstgutachter: Prof. Dr. Selma de Mink  
Zweitgutachter: Prof. Dr. Achim Weiß  
Tag der mündlichen Prüfung: 09.04.2024

# Contents

<b>List of Figures</b>	<b>vii</b>
<b>List of Tables</b>	<b>xi</b>
<b>Zusammenfassung</b>	<b>xiii</b>
<b>Abstract</b>	<b>xv</b>
<b>1 Introduction</b>	<b>1</b>
1.1 Evolution of binary stars . . . . .	2
1.2 Evolution and dynamics of multiple-star systems . . . . .	3
1.3 Encounters in star clusters . . . . .	4
1.4 Organization of this thesis . . . . .	5
<b>2 Gravitational wave progenitors in quadruple-star systems</b>	<b>7</b>
2.1 Introduction . . . . .	7
2.2 Methods . . . . .	9
2.2.1 Gravitational dynamics . . . . .	9
2.2.2 Stellar evolution . . . . .	10
2.3 Examples . . . . .	11
2.4 Population synthesis . . . . .	13
2.4.1 Different models . . . . .	13
2.4.2 Initial conditions . . . . .	18
2.4.3 Other parameters and assumptions . . . . .	22
2.5 Results . . . . .	23
2.5.1 Definitions of certain quantities . . . . .	24
2.5.2 2+2 quadruples and isolated binaries . . . . .	24
2.5.3 3+1 quadruples . . . . .	27
2.5.4 Scenarios of mergers . . . . .	30
2.5.5 Merger rate calculation . . . . .	34
2.5.6 Systems not considered . . . . .	35
2.6 Discussion . . . . .	37
2.6.1 Merger rate comparisons . . . . .	37

2.6.2	Caveats . . . . .	39
2.7	Conclusion . . . . .	40
<b>3</b>	<b>Dynamical stability of triple-star systems</b>	<b>43</b>
3.1	Introduction . . . . .	43
3.2	$N$ -body code and stability . . . . .	45
3.3	Data set and initial conditions . . . . .	46
3.4	Updated formula . . . . .	47
3.4.1	Eccentricity dependence . . . . .	49
3.4.2	Mutual inclination dependence . . . . .	49
3.4.3	Mass ratio dependence . . . . .	53
3.5	Machine learning approach . . . . .	53
3.5.1	Multi-layer perceptrons . . . . .	53
3.5.2	Training and testing data sets . . . . .	55
3.5.3	Network architecture and hyper-parameters . . . . .	56
3.6	Results and comparison . . . . .	56
3.7	Discussion . . . . .	57
3.8	Conclusion . . . . .	60
<b>4</b>	<b>Dynamical stability of quadruple-star systems</b>	<b>61</b>
4.1	Introduction . . . . .	61
4.2	$N$ -body code and stability . . . . .	63
4.3	Machine learning classifier . . . . .	65
4.3.1	Data set and initial conditions . . . . .	65
4.3.2	Multi-layer perceptron (MLP) - implementation . . . . .	66
4.4	From a triple to a quadruple . . . . .	67
4.5	Results . . . . .	68
4.5.1	MLP model performances . . . . .	69
4.5.2	Analysing the stability criterion . . . . .	70
4.5.3	Parameter space slices . . . . .	71
4.5.4	The complete parameter space . . . . .	71
4.6	Discussion . . . . .	74
4.7	Conclusion . . . . .	77
<b>5</b>	<b>Tidal disruptions of stars due to stellar-mass black holes</b>	<b>79</b>
5.1	Introduction . . . . .	79
5.2	Methods . . . . .	81
5.2.1	Hydrodynamics . . . . .	81
5.2.2	Stellar models . . . . .	82
5.2.3	Black hole . . . . .	84
5.2.4	Initial conditions . . . . .	85
5.3	Analysis . . . . .	85
5.3.1	Calculation of bound and unbound mass . . . . .	85

---

5.3.2	Calculation of orbital and spin parameters . . . . .	86
5.4	Results . . . . .	86
5.4.1	Effect of density concentration factor . . . . .	86
5.4.2	Post-disruption stellar and BH masses . . . . .	91
5.4.3	Post-disruption stellar spins . . . . .	91
5.4.4	Post-disruption orbital parameters . . . . .	93
5.4.5	Rates of tidal encounters . . . . .	96
5.4.6	Summary of fits . . . . .	97
5.5	Implications . . . . .	99
5.5.1	Low-mass X-ray binaries . . . . .	100
5.5.2	Intermediate-mass black hole growth . . . . .	100
5.5.3	Fast blue optical transients . . . . .	101
5.5.4	Ultra-long gamma-ray bursts and X-ray flares . . . . .	102
5.5.5	Remnants . . . . .	103
5.5.6	Caveats . . . . .	103
5.6	Summary and conclusion . . . . .	104
<b>6</b>	<b>Conclusions</b>	<b>105</b>
	<b>Glossary of abbreviations</b>	<b>107</b>
	<b>Bibliography</b>	<b>109</b>
	<b>Acknowledgements</b>	<b>123</b>





# List of Figures

1.1	Schematic of stable and unstable mass transfer in binary stars . . . . .	3
1.2	Mobile diagrams of a triple and the two types of quadruple-star systems. .	4
1.3	Illustration of the tidal disruption of a star due to a close approach to a stellar-mass black hole. . . . .	5
2.1	Example of a 2+2 quadruple system undergoing essentially isolated binary evolution with CE formation and eventually leading to a NS-NS merger. .	14
2.2	Example of a 2+2 quadruple system where a CE does not form, and the eventual BH-BH merger is solely due to secular evolution. . . . .	15
2.3	Example of a 2+2 quadruple system in which both secular evolution and CE evolution play a key role in the eventual BH-NS merger. . . . .	16
2.4	Example of a 3+1 quadruple system in which both secular evolution and CE evolution play a key role in the eventual BH-BH merger. . . . .	17
2.5	Initial mass distribution of 2+2 quadruple systems for all models. . . . .	19
2.6	Initial mass distribution of 3+1 quadruple systems for all models. . . . .	19
2.7	Initial semi-major axis and eccentricity distribution of 2+2 quadruple systems for all models. . . . .	20
2.8	Initial semi-major axis and eccentricity distribution of 3+1 quadruple systems for all models. . . . .	21
2.9	LIGO-band eccentricities for compact object mergers in isolated binaries, 2+2 and 3+1 quadruples. . . . .	28
2.10	Effective spin parameters for compact object mergers in isolated binaries, 2+2 and 3+1 quadruples. . . . .	29
2.11	Precession spin parameters for compact object mergers in 2+2 and 3+1 quadruples. . . . .	30
2.12	Mass ratios for compact object mergers in 2+2 and 3+1 quadruples. . . . .	31
2.13	Heavier and lighter masses for compact object mergers in 2+2 quadruples. . . . .	32
2.14	Delay time distributions for compact object mergers in 2+2 and 3+1 quadruples. . . . .	33
2.15	Scenario percentages for compact object mergers in 2+2 and 3+1 quadruples. . . . .	34
2.16	Multiplicity fraction as a function of primary mass. . . . .	35
2.17	2+2 and 3+1 quadruple fraction as a function of primary mass. . . . .	36
2.18	Percentage of 2+2 quadruple systems whose run (wall) times exceed 10 hr. . . . .	37

3.1	Number of outer orbits within which unstable triple-star systems become unbound. . . . .	46
3.2	Example 1 parameter space slice where the semimajor axis ratio, and the inner and outer eccentricities are varied. . . . .	50
3.3	Example 2 parameter space slice where the semimajor axis ratio, and the inner and outer eccentricities are varied. . . . .	51
3.4	Example 1 parameter space slice where the semimajor axis ratio and the mutual inclination are varied. . . . .	52
3.5	Example 2 parameter space slice where the semimajor axis ratio, and the mutual inclination are varied. . . . .	52
3.6	Example parameter space slice where the semimajor axis ratio, and the inner and outer mass ratios are varied. . . . .	54
3.7	Schematic of the multi-layer perceptron used for classification. . . . .	55
3.8	Total fraction of ‘false stable’ and ‘false unstable’ systems in the parameter space slice of varying semimajor axis ratio, and inner and outer mass ratios. . . . .	58
3.9	Total fraction of ‘false stable’ and ‘false unstable’ systems in the parameter space slice of varying semimajor axis ratio, and inner and outer eccentricities. . . . .	58
3.10	Total fraction of ‘false stable’ and ‘false unstable’ systems in the parameter space slice of varying semimajor axis ratio and inclination. . . . .	59
4.1	Stability of a 2+2 quadruple system made by splitting the outer star of a stable triple system. . . . .	72
4.2	Stability of a 3+1 quadruple system made by splitting an inner star of a stable triple system. . . . .	73
4.3	Fraction of 2+2 quadruple systems wrongly classified by different classifiers in different zero inclination parameter space slices. . . . .	73
4.4	Fraction of 3+1 quadruple systems wrongly classified by different classifiers in different zero inclination parameter space slices. . . . .	74
4.5	Fraction of all 2+2 quadruple systems in the test data set wrongly classified by the two MLP models ‘2+2 MLP’ and ‘triple MLP’. . . . .	75
4.6	Fraction of all 3+1 quadruple systems in the test data set wrongly classified by the two MLP models ‘3+1 MLP’ and ‘triple MLP’. . . . .	76
5.1	Density and temperature profiles of a $1 M_{\odot}$ MS star. . . . .	81
5.2	Density and temperature profiles of a $0.5 M_{\odot}$ MS star. . . . .	82
5.3	Grid of log density slices of stars undergoing $\mu$ TDEs, with the BH at the center of each panel. . . . .	87
5.4	MESA-derived inverses of density concentration factors for a $1 M_{\odot}$ MS star as a function of stellar age. . . . .	88
5.5	MESA-derived inverses of density mean concentration factors for MS stars of a range of masses and two metallicities. . . . .	88

---

5.6	Post-disruption fractional mass loss, for a star of mass $1 M_{\odot}$ and $0.5 M_{\odot}$ , due to a BH of mass $10 M_{\odot}$ and $40 M_{\odot}$ , as a function of impact parameter and MS age. . . . .	90
5.7	Post-disruption spin angular momentum, for an initially non-rotating star of mass $1 M_{\odot}$ and $0.5 M_{\odot}$ , due to a BH of mass $10 M_{\odot}$ and $40 M_{\odot}$ , as a function of impact parameter and MS age. . . . .	92
5.8	Post-disruption normalized specific orbital energy of the star-BH system, for a star of mass $1 M_{\odot}$ and $0.5 M_{\odot}$ initially in a parabolic orbit, due to a BH of mass $10 M_{\odot}$ and $40 M_{\odot}$ , as a function of impact parameter and MS age. . . . .	94
5.9	Post-disruption normalized orbital eccentricity, for a star of mass $1 M_{\odot}$ and $0.5 M_{\odot}$ initially in a parabolic orbit, due to a BH of mass $10 M_{\odot}$ and $40 M_{\odot}$ , as a function of impact parameter and MS age. . . . .	95



# List of Tables

2.1	Parameters varied in different models of quadruples. . . . .	18
2.2	Initial conditions and parameters of quadruples. . . . .	23
2.3	Number of compact object mergers in 2+2 and 3+1 quadruples, and isolated binaries. . . . .	25
2.4	Merger rates of compact object mergers in 2+2 and 3+1 quadruples. . . . .	36
3.1	Parameter space slices where the semimajor axis ratio, and the inner and outer mass ratios are varied. . . . .	47
3.2	Parameter space slices where the semimajor axis ratio, and the inner and outer eccentricities are varied. . . . .	47
3.3	Parameter space slices where the semimajor axis ratio and the mutual inclination are varied. . . . .	48
3.4	Overall scores, precisions and recalls for the different triple-stability classifiers we compare with. . . . .	57
4.1	Parameter space slices (zero inclination) considered for 2+2 quadruples. . .	68
4.2	Parameter space slices (zero inclination) considered for 3+1 quadruples. . .	68
4.3	Classification results of different classifiers for 2+2 quadruples. . . . .	69
4.4	Classification results of different classifiers for 3+1 quadruples. . . . .	70
5.1	Parameters of the MS star models. . . . .	83
5.2	Initial parameters of our suite of $\mu$ TDE simulations. . . . .	84
5.3	Evaluated values of the impact parameter for the full disruption of a star with uniform density, for polytropic stars. . . . .	89
5.4	Post-disruption parameter values for our 58 $\mu$ TDE simulations. . . . .	99
6.1	Table of abbreviations. . . . .	108



# Zusammenfassung

Ein erheblicher Teil der Sterne im Universum existiert in Doppel- und Mehrfachsystemen, während andere in dichten stellaren Umgebungen wie Sternhaufen leben. Derartige Sterne entwickeln sich anders als ihre isolierten Gegenstücke aufgrund verschiedener Wechselwirkungen mit ihren Begleitern, wie beispielsweise der wechselseitige Transfer von Masse, stellare Gezeitenkräfte, oder gegenseitige Bahnablenkungen und Kollisionen. Viele faszinierende Beobachtungsphänomene, wie die Emission von Gravitationswellen und Gezeiten-Sternzerrissereignis, sind auf diese Wechselwirkungen zurückzuführen. In dieser Arbeit habe ich das Zusammenspiel zwischen Sternentwicklung und -dynamik untersucht und konzentriere mich dabei auf hierarchische Mehrfachsternsysteme und die gravitative Wechselwirkung von Sternen.

Zunächst untersuchte ich die Verschmelzung von kompakten Objekten, d.h. von Schwarzen Löchern und Neutronensternen in Vierfachsternsystemen. Diese Verschmelzungen sind von großem Interesse, da sie die Ursache für die Emission von Gravitationswellen sind. Mithilfe des Populationssynthese-Codes `MSE` habe ich herausgefunden, dass die säkulare Entwicklung in Vierfachsternsystemen, die hohe Exzentrizitäten in den stellaren Umlaufbahnen hervorrufen kann, eine entscheidende Rolle dabei spielt, die kompakten Objekte nah genug aneinander heranzubringen, um innerhalb der Hubble-Zeit zu verschmelzen. Darüber hinaus kann die Verschmelzung von binären Schwarzen Löchern in derartigen Systemen erheblich zu den beobachteten Raten beitragen.

Die Zuverlässigkeit solcher Populationssynthesestudien hängt von Verständnis der Entwicklung von Mehrfachsternsystemen ab, was eine umfassende Analyse ihrer dynamischen Stabilität erfordert. Mit Hilfe von Klassifikationsverfahren für neuronale Netze in Verbindung mit dem  $N$ -Körper code `MSTAR` habe ich Dreifach- und Vierfachsysteme durch die Bewertung ihrer langfristigen Gebundenheit als stabil oder instabil definieren können. Insbesondere für Dreifachsysteme habe ich die Genauigkeit einer bestehenden analytischen Klassifizierungsformel verfeinert und verbessert. Diese Studie erforscht daher eingehend die langfristige Stabilität dieser Systeme und bietet wichtige Einblicke in ihre Entwicklung und Dynamik.

Darüber hinaus untersuchte ich die gravitative Wechselwirkung zwischen Sternen und stellaren Schwarzen Löchern im Kontext von Sternhaufen. Diese Wechselwirkungen führen häufig zu Mikrogezeitenstörungen ( $\mu$ TDEs), welche die Flugbahnen und Massen der beteiligten Objekte verändern. Mit Hilfe detaillierter 3D-Simulationen unter Verwendung des Hydrodynamik-Codes `AREPO` und des Sternentwicklung-Codes `MESA` habe ich die Massen, Spins und Um-

laufbahnen nach partiellen  $\mu$ TDEs bestimmt. Die daraus abgeleiteten analytischen Formeln sind ein wertvolles Werkzeug für die genaue Modellierung von Wechselwirkungen zwischen Sternen und Schwarzen Löchern in Sternhaufenumgebungen.

Diese Studien unterstreichen die Bedeutung externer Faktoren für die Entwicklung von Sternen. Sie zeigen, wie wichtig es ist, neben der Entwicklung einzelner Sterne auch die stellare Dynamik und die Wechselwirkungen des Massentransfers zu verstehen, um ein vollständiges Bild ihres Lebens zu zeichnen.



# Abstract

A significant fraction of stars in the Universe exist within binary and multiple-star systems, while others reside in dense stellar environments like star clusters. These stars evolve quite differently from their isolated counterparts due to various interactions with their companions, some of which include mass transfer, stellar tides, stellar encounters, and collisions. Many fascinating observational phenomena, such as gravitational wave emission and tidal disruption events, occur due to these interactions. In this thesis, I studied this interplay between stellar evolution and dynamics, specifically focusing on hierarchical multiple-star systems and the gravitational encounters of stars.

First, I investigated the mergers of compact objects, i.e., black holes and neutron stars, within quadruple-star systems. These mergers garner considerable interest as the progenitors of gravitational wave emission. Utilizing the population synthesis code `MSE`, I found that secular evolution in quadruples, which can induce high eccentricities in the stellar orbits, plays a pivotal role in bringing the compact objects close enough to merge within a Hubble time. Furthermore, binary black hole mergers in such systems can represent a significant fraction of the observed rates.

The reliability of such population synthesis studies hinges upon understanding the evolution of multiple-star systems, necessitating a comprehensive analysis of their dynamical stability. Using neural network classifiers in conjunction with the  $N$ -body code `MSTAR`, I accurately classified triples and quadruples as stable or unstable by assessing their long-term boundedness. Specifically for triples, I refined and enhanced the accuracy of an existing analytical classification formula. This study sheds light on the long-term stability of these systems, offering crucial insights into their evolution and dynamics.

Additionally, I explored close encounters between stars and stellar-mass black holes within the context of star clusters. These interactions often lead to micro tidal disruption events ( $\mu$ TDEs), which alter the trajectories and masses of the involved objects. By conducting detailed 3D simulations using the hydrodynamics code `AREPO` and the stellar evolution code `MESA`, I determined the masses, spins, and orbital trajectories of the remnants resulting from partial  $\mu$ TDEs. The derived analytical formulae provide a valuable tool for accurately modeling star-black hole interactions within star cluster environments.

These studies underscore the importance of external factors in shaping the evolution of stars. Therefore, it is essential to understand stellar dynamics and mass transfer interactions, in addition to single star evolution, to paint a complete picture of their lives.



# Chapter 1

## Introduction

*"I like the night. Without the dark, we'd never see the stars."*

– Stephanie Meyer, *Twilight*

Stars, the celestial beacons of the night sky, have captivated human curiosity since time immemorial, transcending cultural boundaries. The ancient Chinese meticulously observed celestial phenomena and developed accurate calendar systems based on lunar cycles. The Indians developed the decimal system and the concept of zero, providing astronomers with essential mathematical tools for precise calculations. The ancient Greeks formulated early models of the universe and made important contributions to the measurement of stellar positions. Arab astronomers during the Islamic Golden Age built upon earlier knowledge, developing sophisticated instruments, like the astrolabe, and producing detailed star catalogs. These contributions paved the way for later scientific advancements in the Western world. Since then, each technological leap in observational astronomy has helped to reveal the complexities of stellar birth, life, and ultimate demise.

Stars are powered by thermonuclear fusion reactions occurring in their cores. Throughout their lives, there is a constant struggle between the ever-present inward gravitational force and the outward radiation pressure. When the nuclear fuel is finally exhausted or cannot 'burn' any longer, gravity finally wins and only stellar remnants – compact objects – remain. The evolution, lifetimes, and eventual fates of stars are highly dependent on their initial masses and metallicities. In general, higher-mass stars are brighter, hotter, and short-lived, while lower-mass stars are dimmer, cooler, and long-lived.

In addition to these properties, the environments where stars live are critical to their fates. Luckily for us, and all life on Earth, our Sun is an isolated star and quite steady in its energy radiation. However, a significant fraction of stars (more than  $\sim 50\%$ ) in the Universe either have companions (e.g., [Raghavan et al., 2010](#); [Sana et al., 2012](#); [Moe & Di Stefano, 2017](#)) or are in very dense stellar environments – star clusters. Many notable examples exist in our own stellar backyard. Sirius, the brightest star in the night sky is a binary system ([Bessel, 1844](#); [Flammarion, 1877](#)) consisting of a bright A-type main-sequence star and a faint white dwarf companion. The nearest star to the Sun, Alpha

Centauri, is in fact a triple system (Kameswara-Rao et al., 1984; Innes, 1915) consisting of an inner binary of two Sun-like stars and an outer red dwarf companion. Going further, Capella, the sixth-brightest star as seen from Earth, is a 2+2 quadruple system (Campbell, 1899; Newall, 1899; Furuholm, 1914; Stearns, 1936) consisting of a giant star binary and a red dwarf binary bound together. A final, incredible example is of Castor, one of the Gemini twins, a hierarchical sextuple system (Muller, 1955; Heintz, 1980, 1988) consisting of a 2+2 quadruple and a binary bound together. In addition, strewn across the night sky are clusters of stars, like the bright open cluster Pleiades (Michell, 1767), a collection of thousands of stars, and the immense globular cluster Omega Centauri (Halley, 1715; Dunlop, 1828), a dense spherical mass of over 10 million stars.

Stars in such non-isolated environments evolve quite differently from their single counterparts. Changes in their structure and dynamics can occur in short, dynamical timescales, unlike in the stars like the Sun where these changes take long, thermal or nuclear timescales to manifest. Matter interactions in binary- and multiple-star systems are instrumental in explaining the occurrences of many astronomical curiosities like blue stragglers (e.g. Sandage, 1953), Be stars (e.g. Secchi, 1866; Snow & Marlborough, 1976), cataclysmic variables (e.g. Walker, 1954; Joy, 1954), X-ray binaries (e.g. Sandage et al., 1966), thermonuclear supernovae (e.g. Wheeler & Hansen, 1971), millisecond pulsars (e.g. Backer et al., 1982), kilonovae (e.g. Tanvir et al., 2013; Abbott et al., 2017), and gravitational wave sources (e.g. Abbott et al., 2016). Stars present in dense clusters can have gravitational encounters with black holes and other stars, which can lead to transient phenomena like stellar collisions and (micro) tidal disruption events (e.g., Perets et al., 2016).

All things considered, the evolution of stars is shaped by not only single-star evolution but also stellar dynamics. Thus, it is imperative to study these interactions to properly model the evolution of a system of stars, either binaries and triples in the field or stars in globular and nuclear star clusters. In the following sections, I briefly outline binary- and multiple-stellar evolution, and star cluster dynamics.

## 1.1 Evolution of binary stars

The evolution of binary stars depends not only on their masses and metallicities but also on their radii and the orbital parameters defining the distance between them. Mass transfer, a pivotal aspect of binary star evolution, greatly influences the fates of both stars in the system. A schematic of mass transfer in binary stars is depicted in Figure 1.1.

Mass transfer occurs when one of the stars overfills its tear-shaped gravitational Roche lobe (e.g., Paczyński, 1971; see Figure 1.1). The excess mass is transferred, in a stable manner, to the companion through the inner Lagrangian point between the two stars. This phenomenon is termed Roche Lobe Overflow (RLOF), which transpires when a star expands beyond its Roche lobe due to stellar evolution or orbital shrinkage. In some instances, binary stars may undergo a more dramatic phase known as common envelope evolution (CEE) when the mass transfer is unstable (e.g., Paczynski, 1976; van den Heuvel, 1976). This occurs when one star undergoes significant expansion, engulfing its companion

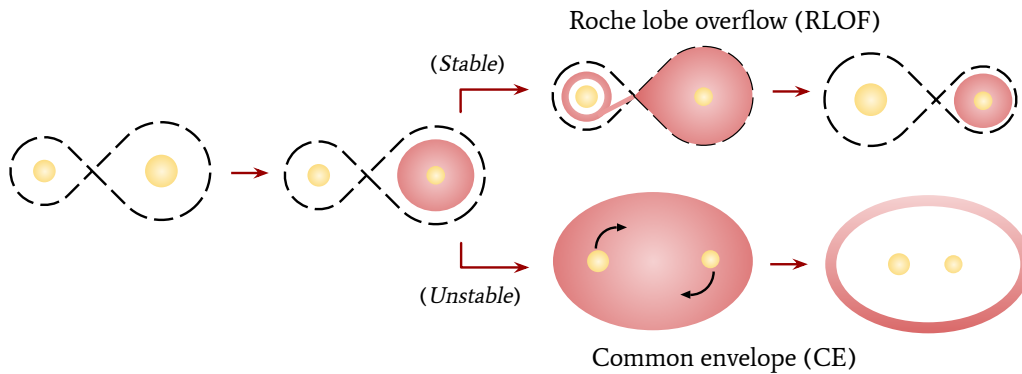


Figure 1.1: Schematic of stable (RLOF) and unstable (CEE) mass transfer in binary stars, with the Roche lobes indicated in dashed lines. RLOF from the donor to the accretor happens at the inner Lagrangian point (where the Roche lobes intersect). CEE results in the inspiraling of the stars and eventual expelling of the envelope.

within a shared gas envelope. Frictional forces dissipating the orbital energy cause the stars to spiral inward, ultimately expelling the envelope (e.g., [Iben & Livio, 1993](#)). This process may lead to the formation of a close binary compact object system capable of merging within the age of the universe through gravitational wave emission. Numerous studies (e.g., [Belczynski et al., 2002](#); [Dominik et al., 2012](#); [de Mink & Mandel, 2016](#)) have examined the properties and rates of compact object mergers using population synthesis approaches. Chapter 2 provides a more detailed discussion of the implications for gravitational waves.

In addition to RLOF and CEE, stellar tides also contribute to structural and dynamical changes in binary star systems (e.g., [Alexander, 1973](#); [Hut, 1981](#)). Tidal forces arise from the proximity between companions, causing deformations and synchronization between the rotational and orbital periods of the stars. This interaction can impact mass transfer rates and lead to the circularization of orbits.

## 1.2 Evolution and dynamics of multiple-star systems

Increasing the number of gravitationally bound objects in a system adds complexity through dynamical perturbations. Using Newtonian mechanics, it is straightforward to derive analytically that two point-masses follow closed, Keplerian orbits and remain stable indefinitely<sup>1</sup>. However, a three-body system is famously chaotic and has been analytically solved only for a few restrictive cases. That being said, 'hierarchical' configurations of triples, as well as higher order multiples, can indeed remain stable for extended periods.

In a hierarchical configuration, stars are organized in 'nested' binaries. For instance, a hierarchical triple comprises two relatively close stars in an 'inner' binary, and a third, distant companion forming an 'outer' binary with the center of mass of the two inner

<sup>1</sup>In reality, binary stars are not point-like objects and experience dissipative forces such as tides. Additionally, post-Newtonian mechanics becomes significant for large masses and close distances.

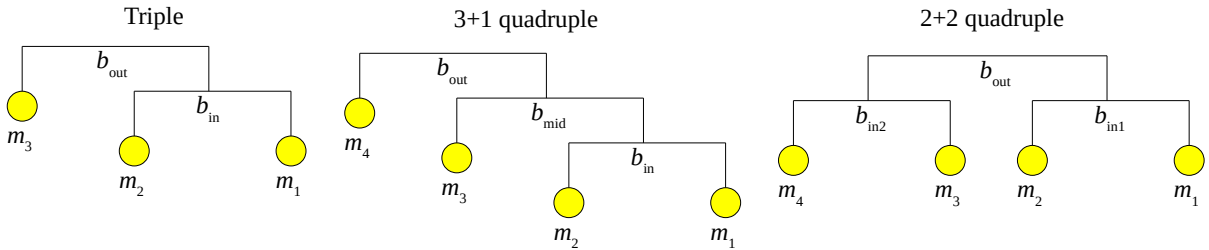


Figure 1.2: Mobile diagrams of a triple and the two types of quadruple-star systems (adapted from [Vynatheya & Hamers, 2022](#)). Here, each internal node  $b_i$  corresponds to a ‘nested’ binary and each leaf node  $m_i$  corresponds to a star.

stars. As the number of stars increases, a multitude of hierarchical configurations become feasible. A hierarchical quadruple, for example, can exist in two configurations: 1) 2+2, where two ‘inner’ binaries orbit each other, and 2) 3+1, where a fourth, even more distant body orbits a triple. These configurations can be represented in simple tree or mobile diagrams as shown in Figure 1.2.

The orbits of stars in (hierarchical) multiple systems are essentially Keplerian at the zeroth order. The presence of additional bodies introduces extra terms to the Lagrangian, determining the magnitude of orbital perturbations and, consequently, the long-term dynamical stability. The quadrupole-order term in a triple leads to (von Zeipel)-Lidov-Kozai oscillations ([Lidov, 1962](#); [Kozai, 1962](#); [von Zeipel, 1910](#)), which entail periodic changes in the stellar orbits’ eccentricities and inclinations. Octupole (e.g., [Naoz, 2016](#)) and higher order terms induce more pronounced eccentricity excitations, thereby increasing the likelihood of collisions and mergers. Quadruples (e.g., [Hamers et al., 2015](#); [Hamers & Lai, 2017](#)) exhibit an even larger parameter space for eccentricity changes and are more chaotic. Chapters 3 and 4 provide comprehensive explanations of the dynamics and stability of triple- and quadruple-star systems, respectively.

As a consequence of these dynamical perturbations, the constituent stars may undergo RLOF and CEE events earlier in their lifetimes. This is due to higher eccentricities resulting in closer periastris approaches, allowing the stars to fill their now-smaller Roche lobes. These close approaches also lead to orbit circularization due to stellar tides. The implications of quadruple-star dynamics on their evolution, particularly on compact object mergers, are discussed extensively in Chapter 2.

### 1.3 Encounters in star clusters

Most stars form within clusters in dense regions of molecular clouds (e.g., [Lada & Lada, 2003](#)), some of which eventually evolve into star clusters. Globular clusters and nuclear star clusters stand out as some of the most massive and dense stellar environments. In these settings, gravitational encounters between stellar objects are not only common but also integral to their dynamic evolution (e.g., [Lin & Tremaine, 1980](#)).

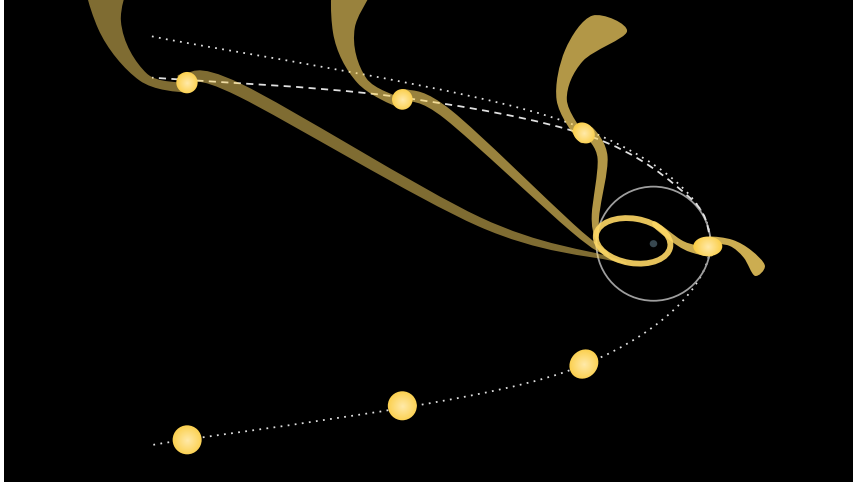


Figure 1.3: Illustration of the tidal disruption of a star due to a close approach (solid circle) to a stellar-mass black hole (right center). Shown here are the tidal streams of matter lost from the star, almost half of which becomes bound to the black hole. Due to this mass loss, the initial trajectory (dotted line) of the star is altered (dashed line).

In Chapter 5, we explore the phenomenon known as a micro-tidal disruption event ( $\mu$ TDE; e.g., [Perets et al., 2016](#)), which emerges from the interaction between a star and a stellar-mass black hole in the dense core of a cluster. The prefix 'micro' is applied to distinguish these occurrences from TDEs caused by supermassive black holes in galactic centers (see [Gezari, 2021](#) for a review). For a tidal disruption event to happen, the star must approach the black hole at a distance close to the 'tidal' radius. If the closest approach distance is sufficiently far, the star undergoes a partial disruption, losing a fraction of its mass due to tidal forces. However, if it approaches even closer, the star is completely ripped apart, termed full disruption. A schematic of a partial micro-tidal disruption event is depicted in Figure 1.3.

Furthermore, dense clusters also contain binary stars (e.g., [Hut et al., 1992](#)), which can engage in binary-single interactions (e.g., [Hut & Bahcall, 1983](#)) and binary-binary interactions (e.g., [Mikkola, 1983](#)). However, these interactions fall outside the scope of this thesis.

## 1.4 Organization of this thesis

Having introduced various aspects of stellar evolution and dynamics, I delve into some interesting aspects of non-isolated stars in this thesis. Each of the next four chapters presents one of my publications.

In Chapter 2, I conduct a population synthesis study of quadruple-star systems to understand their significance in gravitational wave emission. I find that compact object mergers in quadruple-star systems represent a sizeable fraction of currently detected rates

of gravitational wave events. Moreover, secular evolution in quadruples, which is a consequence of gravitational perturbation from companion stars, aids in the merger of compact objects.

In Chapters 3 and 4, I analyze the origin of dynamical stabilities of triple- and quadruple-star systems respectively. Using a machine learning approach to gravitational  $N$ -body dynamics, I accurately classify multiple-star systems into dynamically stable and unstable systems. In the case of triples, I also provide an updated version of an analytical classification criterion to better capture three-body dynamics.

In Chapter 5, I study the effects of tidal disruptions of stars encountering stellar-mass black holes through hydrodynamics simulations. By varying stellar and black hole masses, I simulate a suite of partial tidal disruption events to quantify the dependencies of remnant masses, spins, and orbits on the initial conditions. Furthermore, I provide easy-to-implement fits for these parameters that can be incorporated into cluster codes.

Finally, I provide a brief summary and conclude this thesis in Chapter 6.



# Chapter 2

## Gravitational wave progenitors in quadruple-star systems

This chapter reproduces the paper [Vynatheya & Hamers \(2022\)](#), titled “*How important is secular evolution for black hole and neutron star mergers in 2+2 and 3+1 quadruple-star systems?*”, and published in the journal ApJ. The initial setup, code runs, and final analysis were all conducted by me. The text has been written mainly by me, with contributions from Adrian Hamers.

### 2.1 Introduction

In the past few years, there have been extensive studies of gravitational wave (GW) sources and their progenitors. This has been motivated by recent detections of GWs by LIGO/VIRGO, starting in 2015. [Abbott et al. \(2021a\)](#) introduced the second and latest version of the Gravitational Wave Transient catalog (GWTC-2), which also includes the GW detections from the previous catalog (GWTC-1) of [Abbott et al. \(2019\)](#).

GWs are emitted during the merger of neutron stars (NSs) and black holes (BHs). These compact objects are the final stages in the evolution of massive stars ( $\gtrsim 8 M_{\odot}$ , assuming solar metallicity and single star evolution). Hence, for individual BHs and NSs to merge, the progenitor massive stars must avoid merging before evolving into a compact object binary. Various stages in a star’s life (radius expansion in giant phases, mass-loss due to stellar winds, external encounters, supernova kicks) tend to destroy binary systems before compact object formation. Therefore, systems with binary BHs and NSs are expected to be very rare. Mergers within a Hubble time ( $\sim 14$  Gyr) are even rarer.

Any proposed channel for the merger of compact objects (henceforth used to refer only to BHs and NSs, and not white dwarfs or WDs) must, hence, explain the presence of such systems and their merger within a Hubble time. There have been a number of merger channels proposed in the recent past, which can be divided into: (1) isolated binary evolution (e.g., [Belczynski et al., 2002](#); [Dominik et al., 2012](#); [Belczynski et al., 2016](#); [de Mink & Mandel, 2016](#); [Chruslinska et al., 2018](#); [Giacobbo et al., 2018](#); [Giacobbo &](#)

Mapelli, 2018; Spera et al., 2019); (2) dynamical interactions in star clusters (e.g., Portegies Zwart & McMillan, 2000; Banerjee et al., 2010; Rodriguez et al., 2016; Chatterjee et al., 2017; Banerjee, 2017; Hamers & Samsing, 2019), galactic nuclei (e.g., O’Leary et al., 2009; Antonini & Perets, 2012; Antonini & Rasio, 2016; Petrovich & Antonini, 2017; Hoang et al., 2018; Arca-Sedda & Gualandris, 2018; Hamers et al., 2018; Fragione et al., 2019), and triple and quadruple systems (e.g., Silsbee & Tremaine, 2017; Antonini et al., 2017; Liu & Lai, 2018, 2019; Fragione & Loeb, 2019; Fragione & Kocsis, 2019; Fragione et al., 2020; Arca Sedda et al., 2021; Hamers et al., 2021b); (3) in AGN disks (e.g., Stone et al., 2017a; Bartos et al., 2017; McKernan et al., 2018; Secunda et al., 2019; Tagawa et al., 2020); or (4) primordial BH mergers (e.g., Bird et al., 2016; Sasaki et al., 2016; Raidal et al., 2017; Ali-Haïmoud et al., 2017).

Compact object mergers in triples are interesting for several reasons. Firstly, studies (Raghavan et al., 2010; Moe & Di Stefano, 2017) have found that massive stars, which are the progenitors of BHs and NSs, are most likely found in high-multiplicity star systems. Moe & Di Stefano (2017) showed that for stellar systems in the field with primary components more massive than  $10 M_{\odot}$ , the triple and quadruple fractions each exceed 20%. Secondly, the presence of companion stars can significantly affect the dynamics of triple and quadruple-star systems. Unlike isolated binaries, triple star systems can undergo eccentricity enhancements (if mutual inclinations are large) in the inner binary orbits due to the presence of tertiary companions. These perturbations, to the lowest order, are known as Lidov-Kozai (LK) oscillations<sup>1</sup> (Lidov, 1962; Kozai, 1962; see for reviews Shevchenko, 2017; Naoz, 2016). LK oscillations can accelerate compact object mergers since enhanced eccentricity shortens the coalescence time due to GW-driven orbital inspiral (Blaes et al., 2002; Thompson, 2011). Thus, the study of GW progenitors is incomplete without accounting for multiple-star systems.

Population synthesis is a useful tool to study the statistical properties of such systems. Antonini et al. (2017) used a population synthesis code TRES (Toonen et al., 2016) to combine the effects of orbital dynamics and stellar evolution, in order to estimate merger rates in triples. They derived BH-BH merger rates of  $\sim (0.3\text{--}1.3) \text{ Gpc}^{-3} \text{ yr}^{-1}$ , and showed that mergers from the triple channel have much higher eccentricities in the LIGO band (10 Hz) compared to the isolated binary channel.

In this paper, we concentrate on quadruple-star systems. Quadruples allow for a larger parameter space than triples for eccentricity excitation due to secular (long-term) evolution (Pejcha et al., 2013; Hamers et al., 2015; Hamers, 2017; Hamers & Lai, 2017; Grishin et al., 2018; Hamers, 2018b, 2019; Liu & Lai, 2019). Smaller mutual inclinations can lead to chaotic behavior and extreme eccentricity enhancements if various secular timescales are commensurate. This, coupled with the fact that massive stars are likely to reside in triple and quadruple systems, justifies a detailed investigation into quadruples. Based on their hierarchical configuration, quadruples can be classified into two types – (1) the 2+2, where two binaries orbit each other; and (2) the 3+1, where a triple system is orbited by a distant

---

<sup>1</sup>Also referred to as von Zeipel-Lidov-Kozai oscillations after Ito & Ohtsuka (2019) noted the contribution of von Zeipel (1910)

fourth body (see Figure 1.2).

There have been a few studies on 2+2 quadruples. Fragione & Kocsis (2019) carried out a population synthesis study assuming four BHs in a 2+2 configuration. In reality, the survival of bound quadruple systems consisting of four BHs is rare since gravitational dynamics and stellar evolution tend to destabilize orbits. Supernova (SNe) natal kicks are a major cause of the destruction of potential BH quadruple systems. Therefore, a thorough study self-consistently should combine both these effects to predict merger rates. Nevertheless, the authors found that merger fractions in quadruples can be  $\sim (3-4)$  times higher than in triples. Thus, the quadruple channel cannot be ignored. Hamers et al. (2021b) performed a simplified evolution of 2+2 quadruples, where two binaries are evolved independently, and secular evolution is considered only after compact object formation. They inferred a compact object merger rate of  $\sim (10-100) \text{ Gpc}^{-3} \text{ yr}^{-1}$ , which they mentioned is most likely an overestimation.

In this paper, we go a step further and use the recently-developed population synthesis code *Multiple Stellar Evolution* (MSE), which combines stellar evolution, binary interaction, gravitational dynamics, fly-bys in the field, and other processes seamlessly (Hamers et al., 2021a). Additionally, we study both 2+2 and 3+1 quadruples and compare their merger rates with other channels.

The structure of this paper is as follows. Section 2.2 describes the methods used, Section 2.3 has a few examples of compact object mergers in quadruple systems selected from a large set of population synthesis calculations, Section 2.4 discusses the initial conditions and assumptions made in the population synthesis in detail, Section 2.5 presents the results, Section 2.6 is the discussion, and Section 2.7 concludes.

## 2.2 Methods

For our population synthesis simulations, we use the MSE code (Version 0.84), described thoroughly in Hamers et al. (2021a). A brief overview of MSE is given in the following sub-sections.

### 2.2.1 Gravitational dynamics

MSE uses two methods to model the dynamics of a multi-body system: secular and direct  $N$ -body integration. The code dynamically switches between these two modes depending on the stability of the configuration at a given time step.

The secular (orbit-averaged) approximation is used when the orbit is dynamically stable. It is faster than direct  $N$ -body integration since an orbit-averaged and expanded Hamiltonian is used and orbital phases are not resolved. MSE uses the code SECULARMULTIPLE (Hamers & Portegies Zwart, 2016; Hamers, 2018a, 2020) for this purpose. Tides are included following the equilibrium tide model (Hut, 1981; Eggleton et al., 1998, with the efficiency of tidal dissipation determined by the prescription of Hurley et al., 2002).

Post-Newtonian (PN) terms up to orders 1PN and 2.5PN (ignoring orbit-orbit interaction terms) are considered in the secular integration mode.

In certain situations, however, the secular approximation can break down. This can be due to changes in the orbital parameters due to wind mass-loss from evolving stars, SNe natal kicks, fly-bys, or secular evolution in multiple-star systems (the latter applies particularly to 3+1 quadruple systems). The code then switches to the direct  $N$ -body integration mode, where Newton’s equations of motions are solved using the code `MSTAR` (Rantala et al., 2020). When the switch occurs, the positions and velocities of all bodies are computed under the assumption that the mean anomalies of all orbits evolve linearly with time. The `MSTAR` code uses algorithmic chain regularization for highly accurate integration for a wide range of mass ratios. It includes PN terms, although tidal effects are currently not included.

`MSE` switches modes from secular to direct  $N$ -body in the following cases.

1. The system becomes dynamically unstable according to the stability criterion of Mardling & Aarseth (2001).
2. The system enters the ‘semiseccular regime’ (Antonini & Perets, 2012; Luo et al., 2016; Grishin et al., 2018; Lei et al., 2018; Hamers, 2020) i.e. the timescale of angular momentum change due to secular evolution is shorter than the orbital timescale.
3. Any orbits become unbound due to SNe kicks or mass-loss.
4. After common envelope (CE) evolution and directly following collisions.

The code switches back to the secular mode if it is deemed stable (see Hamers et al., 2021a for details).

### 2.2.2 Stellar evolution

The evolution of isolated stars follows the stellar tracks from the code Single Star Evolution (SSE) (Hurley et al., 2000). The evolution track of a star with given mass and metallicity is fit analytically from a grid of pre-computed tracks of standard masses and metallicities. `MSE` uses SSE at each time step, and the orbital response to stellar mass-loss is calculated, assuming adiabatic wind mass-loss. When a star evolves into an NS or a BH, `MSE` accounts for the mass-loss (assumed to be instantaneous, and with no feedback of the mass lost on the rest of the system) and any natal kicks from the SNe explosion.

In multiple-star systems, however, interactions between stars can become important and binary evolution can play an important role. Many of the assumptions for mass transfer and CE evolution in `MSE` are based on the code Binary Star Evolution (BSE) (Hurley et al., 2002). An exception to this is the way that mass transfer is treated in eccentric orbits. Instead of enforcing circular orbits at the onset of mass transfer, we assume the following

model for the secular orbital changes due to mass transfer in an orbit  $k$ :

$$\frac{\dot{a}_k}{a_k} = -2 \frac{\dot{m}_d}{m_d} \left(1 - \beta \frac{m_d}{m_a}\right) \sqrt{1 - e_k^2} \quad (2.1a)$$

$$\dot{e}_k = -2 \frac{\dot{m}_d}{m_d} \left(1 - \beta \frac{m_d}{m_a}\right) \sqrt{1 - e_k^2} (1 - e_k) e_k \quad (2.1b)$$

where  $a_k$  and  $e_k$  are the orbital semi-major axis and eccentricity, respectively,  $m_d$  and  $m_a$  are the donor and accretor mass, respectively, and  $\beta$  is the mass transfer efficiency. This model is adopted from [Sepinsky et al. \(2007\)](#); [Dosopoulou & Kalogera \(2016\)](#), ignoring finite-size effects, and with an additional factor of  $e_k$  in the equation for  $\dot{e}_k$  to resolve the problem that the equations of motion would otherwise break down as the orbit circularizes due to mass transfer. Our model, although simplified, accommodates the onset and self-consistent treatment of eccentric mass transfer in multiple-star systems.

In addition, MSE includes prescriptions for triple mass transfer and triple CE evolution in the case when an outer star fills its Roche lobe around an inner binary, motivated by more detailed simulations. It also takes into consideration the effect of fly-bys in the field, under the impulsive approximation (see [Hamers et al., 2021a](#) for details).

## 2.3 Examples

In this section, we provide examples of quadruple systems which undergo compact object mergers, using the MSE code. These examples are taken from the population synthesis simulations (Section 2.4). It is important to note that the same systems can evolve differently if different random numbers are generated by the code (for example, the magnitudes and directions of the SNe natal kicks). We describe three qualitatively different scenarios of mergers, in 2+2 quadruples, with examples 1–3. For completeness, we also provide an example of a 3+1 quadruple system undergoing a merger (Scenario 3). Other examples of mergers are briefly mentioned in Section 2.6.

### 1. *Scenario 1: Only CE evolution*

(most of the cases). Figure 2.1 (Model 0) shows a 2+2 quadruple with the inner binaries having relatively small initial semi-major axes ( $a_{\text{in}_1} \simeq 17 \text{ AU}$  and  $a_{\text{in}_2} \simeq 0.1 \text{ AU}$ ), but a much larger outer separation ( $a_{\text{out}} \simeq 3509 \text{ AU}$ , with a periapsis of 807 AU). Owing to the very hierarchical configuration of this quadruple, the inner binaries more or less evolve independently of each other. The ‘interesting’ inner binary, in which the merger occurs, has two massive stars of masses  $16 M_\odot$  and  $17 M_\odot$ . Within  $t \simeq 12.2 \text{ Myr}$ , both stars reach their giant phases, and an RLOF event ensues shortly. After two SNe explosions (which unbind the two binaries from each other, but not the binaries themselves) and CE evolution, the separation between the two new neutron stars reduces significantly. Finally, at  $t \simeq 17.4 \text{ Myr}$ , the NS-NS binary merges due to GW emission. In the meantime, the two stars in the other binary evolve into giants, go through a CE phase of their own and merge into a single

massive star. Eventually, this star evolves into an NS. The bound 2+2 quadruple therefore finally evolves into two single compact objects.

2. *Scenario 2: Only secular evolution*

(extremely rare, only possible with zero SNe kicks). Figure 2.2 (Model 1) shows a 2+2 quadruple with inner binaries with semi-major axes  $a_{\text{in}_1} \simeq 39 \text{ AU}$  and  $a_{\text{in}_2} \simeq 204 \text{ AU}$  (but very high eccentricity of 0.95), and an outer orbit with semi-major axis  $a_{\text{out}} \simeq 3142 \text{ AU}$  and a periapsis of 1288 AU. In the evolution of this system, there are RLOF events, but no CE event to bring inner companions close to each other. The ‘interesting’ binary has two very massive stars of  $41 M_{\odot}$  and  $37 M_{\odot}$ . Since SNe kicks are disabled in this model, the quadruple system remains bound with three BHs and one low-mass main-sequence (MS) star at  $t \simeq 6.0 \text{ Myr}$ . By this time, the BH-BH inner binary is still wide, with a semi-major axis of 696 AU and a periapsis of 90 AU. This is too wide for a merger in a Hubble time. However, secular evolution now shows its capability. The orbit eccentricity is enhanced significantly from 0.87 to almost 1.0 ( $1 - e \simeq 5 \times 10^{-7}$ ) after  $t \simeq 143 \text{ Myr}$ , which leads to a secular breakdown. The two BHs end up making extremely close passes to each other for many million years and ultimately collide at  $t \simeq 1157 \text{ Myr}$ . The LIGO band eccentricity  $e_{\text{LIGO}} = 5 \times 10^{-3}$  is higher than that of Scenario 1. The GW recoil unbinds the merger remnant from the companion binary without strongly interacting with it (i.e., the scenario proposed by Fragione et al., 2020 and Hamers et al., 2021b does not occur here). The companion binary finally becomes a wide BH+WD binary without further interaction (when it was still bound to its companion, it experienced eccentricity excitation).

3. *Scenario 3: (2+2 quadruple) Mixture of both*

(intermediary in occurrence; see Section 2.5.4). Figure 2.3 (Model 0) shows a 2+2 quadruple with wide inner binaries (semi-major axes of  $a_{\text{in}_1} \simeq 217 \text{ AU}$  and  $a_{\text{in}_2} \simeq 405 \text{ AU}$ ) with a large outer separation ( $a_{\text{out}} \simeq 5296 \text{ AU}$ , with a periapsis of 2224 AU). The mutual inclination between the inner and outer orbits is high enough to excite the inner eccentricities from  $e_{\text{in}_1} \simeq 0.04$  to 0.60 and from  $e_{\text{in}_2} \simeq 0.41$  to 0.96 respectively. Chaotic quadruple secular evolution could also play a role here since the two inner semimajor axes are not too distinct from each other (so the LK timescales are similar). This eccentricity enhancement is a key factor for the eventual compact object merger. The periapsis of the ‘interesting’ binary (with masses  $41 M_{\odot}$  and  $17 M_{\odot}$ ) reduces drastically from 243 AU to a mere 18 AU, which is close enough for RLOF and CE evolution to occur. This is what happens after  $t \simeq 4.8 \text{ Myr}$ , and the orbit shrinks even further and circularizes. Again, SNe kicks unbind the quadruple companions, but the inner binary remains intact. The final CE phase brings the two objects to a close separation of 0.01 AU, and a BH-NS merger occurs at  $t \simeq 13.0 \text{ Myr}$ . Meanwhile, the other inner binary does not survive an SNe kick when its more massive star evolves into a BH. The two stars then evolve independently, with the companion becoming a high mass O-Ne WD.

4. *Scenario 3: (3+1 quadruple)*

Figure 2.4 (Model 0) shows a 3+1 quadruple with a very close inner binary ( $a_{\text{in}} \simeq 0.6 \text{ AU}$ ), a fairly distant intermediate star ( $a_{\text{mid}} \simeq 72 \text{ AU}$ ) and a very distant, but very eccentric, outer star ( $a_{\text{out}} \simeq 8014 \text{ AU}$ , with a periapsis of 480 AU). Secular evolution excites the intermediate eccentricity from a low 0.12 to a very high 0.95, with the intermediate periapsis decreasing from 64 AU to just 4 AU. This triggers a phase of dynamical instability; due to the tight inner semi-major axis, the massive inner stars (of masses  $25 M_{\odot}$  and  $20 M_{\odot}$ ) collide early and become a  $44 M_{\odot}$  star. The resulting system is a triple, with a high inner (previously intermediate) eccentricity. The previously intermediate  $20 M_{\odot}$  star becomes a giant and transfers mass to its very massive companion. Note that this type of evolution (the onset of RLOF of a star onto a companion which is twice as massive) is not expected in isolated binary evolution, and is unique to higher-order multiple systems. After another dynamical instability phase, a CE event follows and the two stars end up in a near-circular orbit with a semi-major axis 0.01 AU. The inner stars survive two SNe events (although the outer companion is kicked out), become a BH-NS binary, and merge within  $t \simeq 13 \text{ Myr}$ . Meanwhile, the ejected outer  $8 M_{\odot}$  star eventually becomes an NS.

## 2.4 Population synthesis

We perform a population synthesis of both 2+2 and 3+1 quadruples. Each system is run for 14 Gyr or a Hubble time. In the case of the 2+2 quadruples, we also compare results with isolated binaries having the same initial conditions as the inner binaries of the quadruples. Hence, we have twice as many isolated binaries as 2+2 quadruples for comparison. It is important to note that these isolated binaries are not distributed like real binaries in the field, mainly due to the quadruple stability requirements. The latter implies that the inner binaries in 2+2 quadruples are, on average, more compact compared to ‘truly’ isolated binaries in the field. We include this additional set to directly investigate the effect of secular evolution in quadruples.

For each of the three above-mentioned cases, we use 7 different models which vary certain distributions or parameters (see Section 2.4.1 for details). In each model, we run  $10^5$  quadruples (or  $2 \times 10^5$  binaries in the isolated binaries cases). Hence, in total, we run  $7 \times 10^5$  2+2 and 3+1 quadruples each, and  $14 \times 10^5$  isolated binaries, making a total of  $2.8 \times 10^6$  systems.

The following sub-sections describe the different models used, the initial conditions, and the other important parameters.

### 2.4.1 Different models

To better comprehend our results, we vary different parameters to see how they affect compact object merger rates. We use seven different models, numbered 0, 1, 2, 3a, 3b, 4a, 4b (see Table 2.1). Model 0 is taken to be our fiducial model, and the others are compared

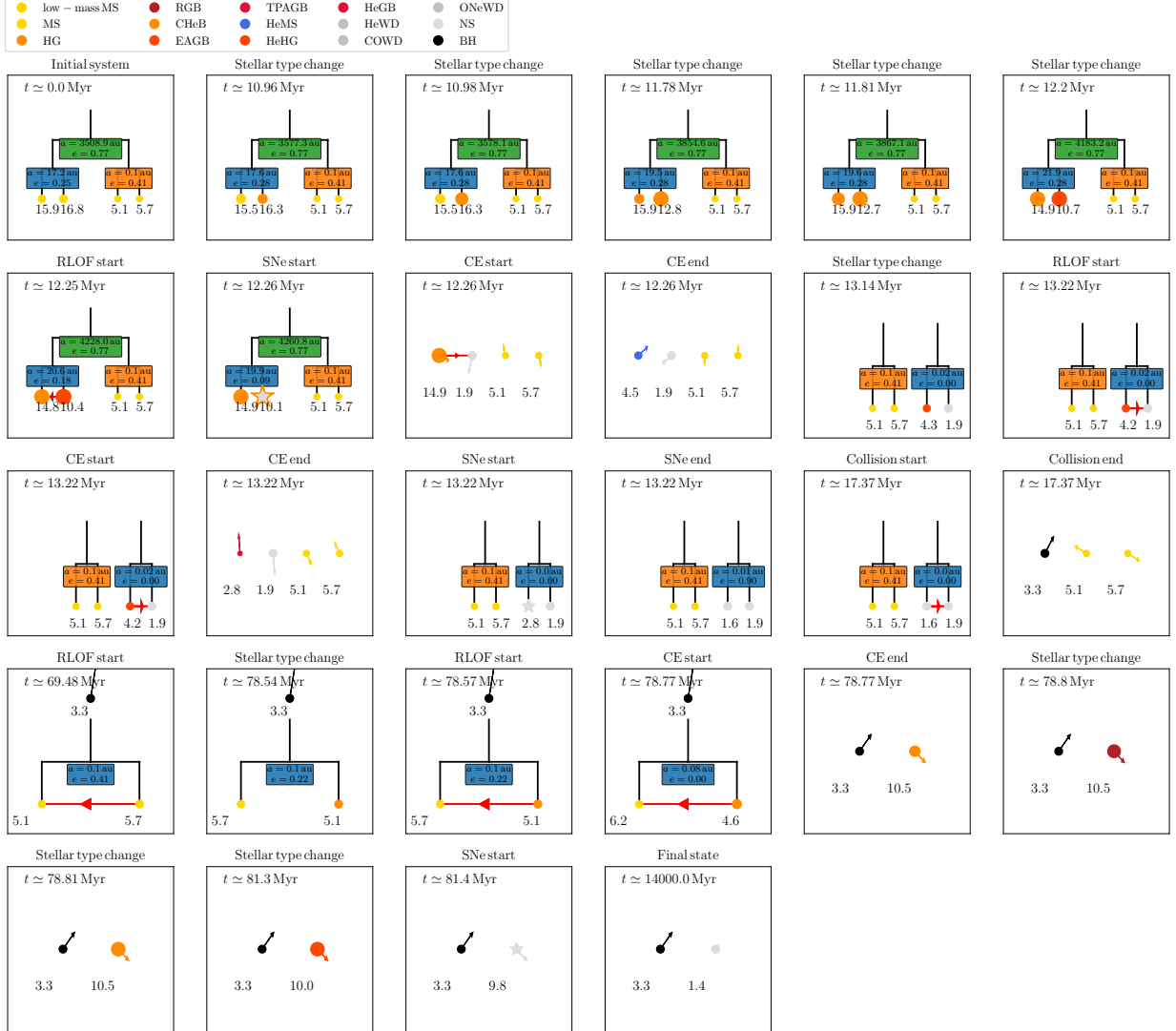


Figure 2.1: *Example 1*: (Model 0) A 2+2 quadruple system undergoing essentially isolated binary evolution with CE formation and eventually leading to a NS-NS merger.

against it. In Model 1, SNe kicks during NS and BH formation are excluded. In Model 2, fly-bys, which are enabled by default, are excluded. In Models 3a and 3b, the stellar metallicities  $Z$  are changed from solar ( $Z_{\odot} = 2 \times 10^{-2}$ ) to one-tenth and one-hundredth of solar metallicity respectively. In Models 4a and 4b, the CE mass-loss timescale  $t_{\text{CE}}$ , which is chosen to be  $10^3$  yr by default, is varied to one-tenth and ten times that of the default respectively.  $t_{\text{CE}}$  parameterizes the timescale at which mass is lost during a CE event. Specifically, if  $t_{\text{CE}}$  is short compared to the orbital period of the companions to the two stars undergoing CE evolution, then the mass-loss can be considered to be instantaneous for these orbits, and the companions can become unbound. In contrast, if  $t_{\text{CE}}$  is long compared to the orbital motion of the outer companions, the effect can be considered to





Figure 2.2: *Example 2*: (Model 1) A 2+2 quadruple system where a CE does not form, and the eventual BH-BH merger is solely due to secular evolution.

be adiabatic and the outer orbits remain bound and become wider. In MSE, these regimes, and the transitional regime, are taken into account by carrying out short term  $N$ -body integrations in which the mass of the binary undergoing CE evolution (modeled as a point mass) gradually loses mass (see Hamers et al., 2021a for details).

Here, we stress that the parameters discussed above are among the many which could have been altered. For example, the CE evolution prescription, the  $\alpha$ -CE model (Paczynski, 1976; van den Heuvel, 1976; Webbink, 1984; Livio & Soker, 1988; de Kool, 1990; see for review Ivanova et al., 2013), is uncertain. In this paper, we choose to alter  $t_{\text{CE}}$  since this effect has not been studied much, whereas it can determine whether or not outer companions remain bound after a CE event (e.g. Michaely & Perets, 2019). However, other

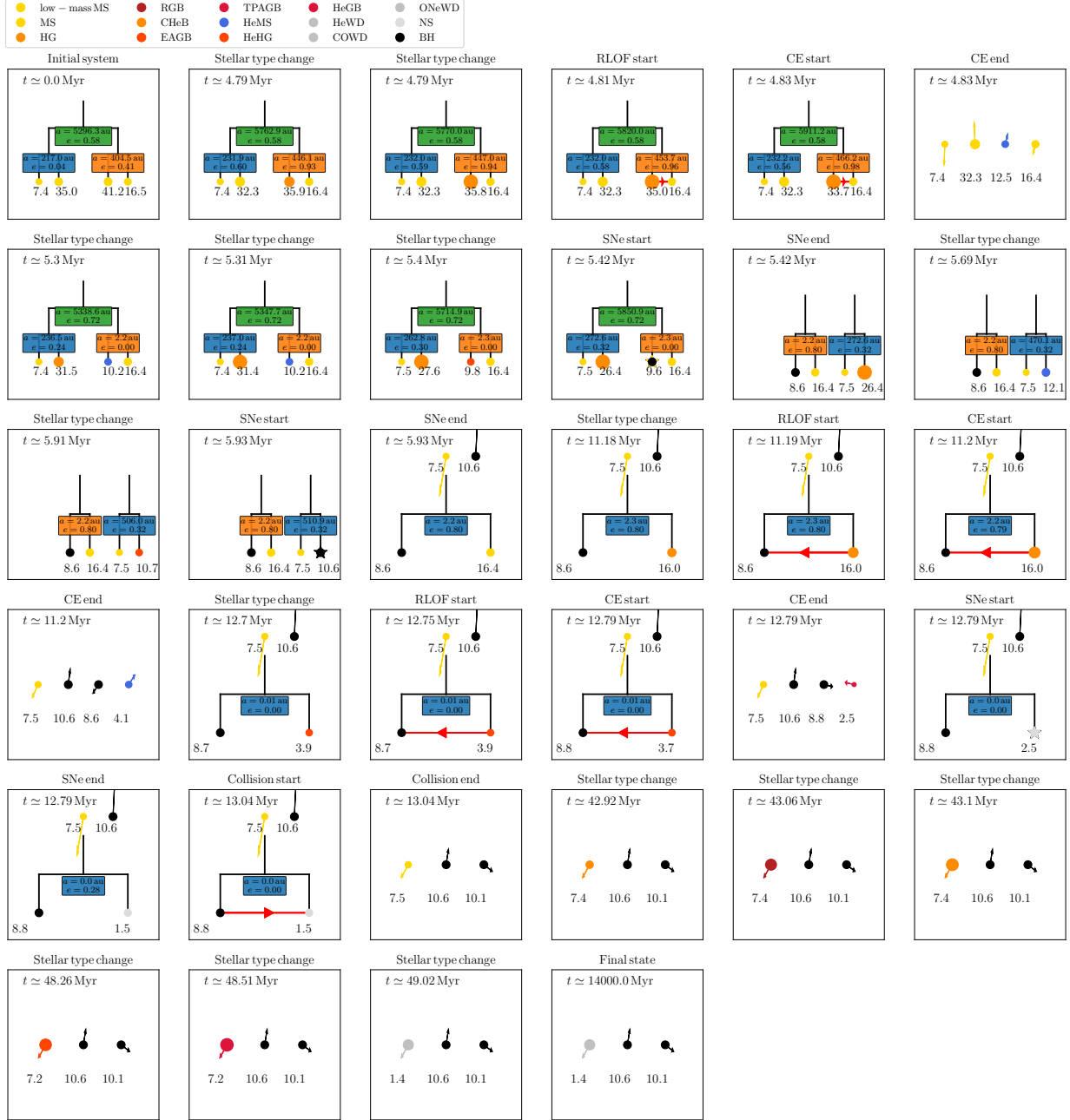


Figure 2.3: *Example 3*: (Model 0) A 2+2 quadruple system in which both secular evolution and CE evolution play a key role in the eventual BH-NS merger.

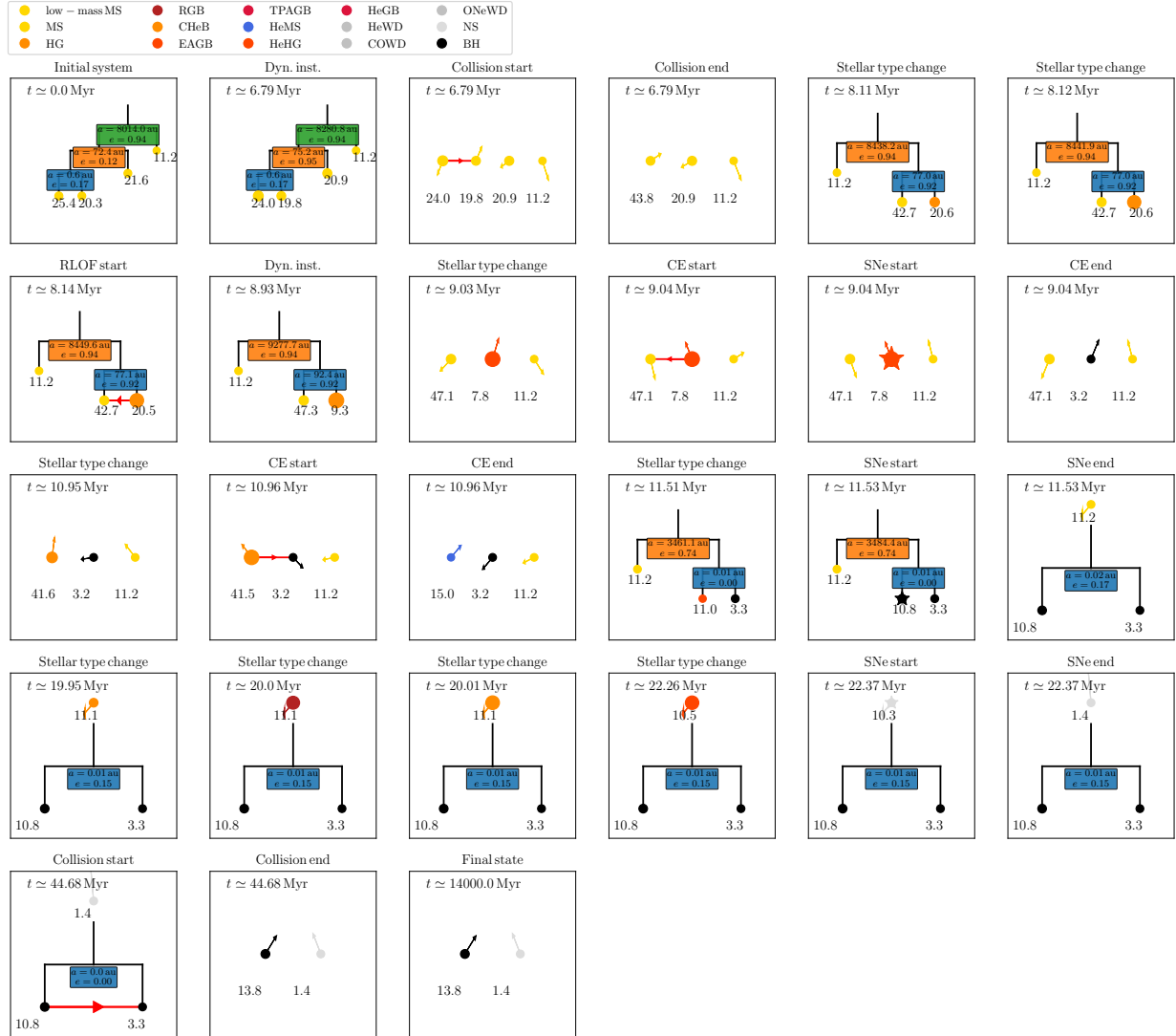


Figure 2.4: *Example 4*: (Model 0) A 3+1 quadruple system in which both secular evolution and CE evolution play a key role in the eventual BH-BH merger.

parameters, most notably the  $\alpha_{\text{CE}}$  parameter, also significantly affect binary evolution and compact object merger rates in particular (Dominik et al., 2012; Broekgaarden et al., 2021; Fragione et al., 2021). Another example is the choice of a model for the SNe kick distribution. We choose a Maxwell-Boltzmann distribution for both NSs and BHs. While the NS kick distribution has been widely studied (e.g., Hobbs et al., 2005), the BH kick distribution is largely unknown. Other assumptions we make include the initial distributions for stellar masses, semi-major axes, and eccentricities. They are still poorly constrained for quadruples; here, we chose to focus on model assumptions, rather than different initial conditions.

The parameters varied in the different models are given in Table 2.1. The details of

Model	SNe kicks	fly-bys	$Z$	$t_{\text{CE}}$
0	non-zero	included	$2 \times 10^{-2}$	$10^3$ yr
1	<b>zero</b>	included	$2 \times 10^{-2}$	$10^3$ yr
2	non-zero	<b>excluded</b>	$2 \times 10^{-2}$	$10^3$ yr
3a	non-zero	included	<b><math>2 \times 10^{-3}</math></b>	$10^3$ yr
3b	non-zero	included	<b><math>2 \times 10^{-4}</math></b>	$10^3$ yr
4a	non-zero	included	$2 \times 10^{-2}$	<b><math>10^2</math> yr</b>
4b	non-zero	included	$2 \times 10^{-2}$	<b><math>10^4</math> yr</b>

Table 2.1: Parameters varied in different models.

important parameters are given in Section 2.4.2.

### 2.4.2 Initial conditions

For each of the quadruple systems, we sample four zero-age main-sequence (ZAMS) masses  $m_i$ , and three each of eccentricities  $e_i$ , semi-major axes  $a_i$ , orbital inclinations  $i_i$ , longitudes of the ascending node  $\Omega_i$  and arguments of periapsis  $\omega_i$ . Stellar metallicities have constant values in each model, as given in Table 2.1. After sampling, we check for dynamical stability of the orbital configuration using the triple stability criterion described by [Mardling & Aarseth \(2001\)](#). For 2+2 quadruples, the stability criterion is evaluated for both inner binaries, considering the other binary to be the ‘tertiary’ star. In the case of 3+1 quadruples, the two ‘triple’ systems are (1) the innermost binary, with the intermediate star as the companion; and (2) the intermediate star-inner two stars binary, with the outermost star as the companion. Furthermore, we also check that the ZAMS stars (with a mass-radius relation given by  $R \sim m^{0.7}$ , in Solar units) do not fill their Roche lobes at periapsis (approximate Roche lobe radii are given by [Eggleton, 1983](#)). If any of these criteria are not fulfilled, the sampling is restarted.

- *Mass sampling:* The primary mass (most massive star in the quadruple system)  $m_{\text{pri}}$  is sampled from a Kroupa distribution ( $dN/dm \propto m^{-2.3}$  in the high-mass tail; [Kroupa, 2001](#)). However, we put an additional constraint that  $m_{\text{pri}} > 8 M_{\odot}$ , which is justified since we look specifically for BH and NS mergers. In principle, it could be possible to form BHs and NSs in multiple-star systems with primary masses  $m_{\text{pri}} < 8 M_{\odot}$  if stellar mergers occur during the evolution, e.g., due to secular eccentricity excitation. However, in post-processing, we find zero compact object mergers in systems with primary masses lower than  $10 M_{\odot}$ . The maximum possible mass of each star is  $100 M_{\odot}$ , a constraint set by SSE.

In the case of 2+2 quadruples, the secondary mass (immediate companion star of the primary)  $m_{\text{sec}}$  is sampled from a flat mass ratio distribution  $\sim U(0, 1)$  with respect to the primary ( $q = m_{\text{sec}}/m_{\text{pri}} < 1$ ). The companion binary is sampled similarly with respect to the original binary and is then split randomly to give the final two masses.

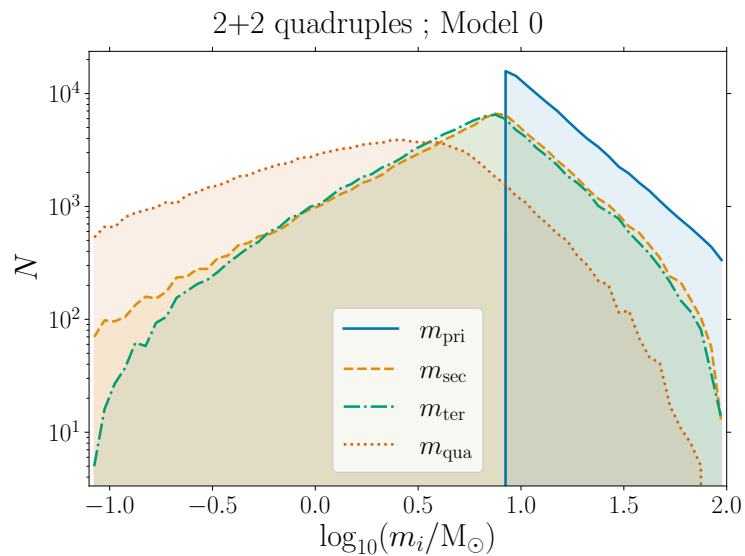


Figure 2.5: Initial mass distribution of  $10^5$  2+2 quadruple systems for all models.  $m_{\text{pri}}$  is the most massive star,  $m_{\text{sec}}$  is its immediate companion,  $m_{\text{ter}}$  is the heavier star in the other binary and  $m_{\text{qua}}$  is its final companion.

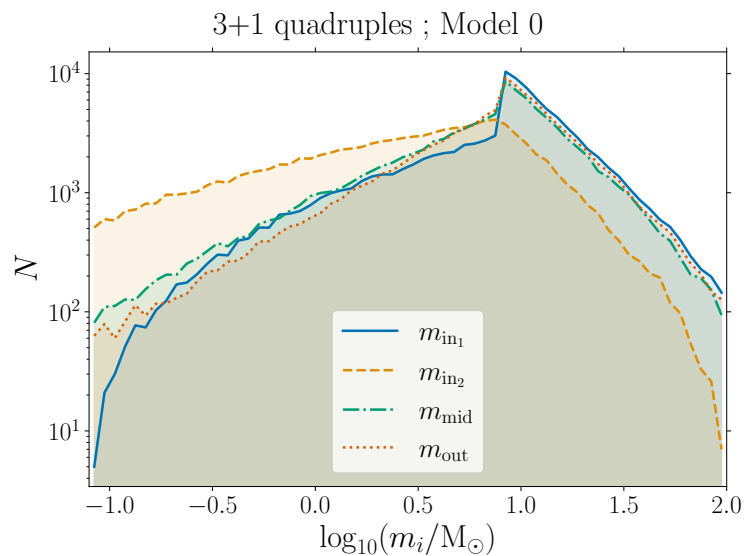


Figure 2.6: Initial mass distribution of  $10^5$  3+1 quadruple systems for all models.  $m_{\text{in}_1}$  is the heavier inner star,  $m_{\text{in}_2}$  is its inner companion,  $m_{\text{mid}}$  is the intermediate star orbiting around the inner binary and  $m_{\text{out}}$  is the outer star orbiting around the triple.

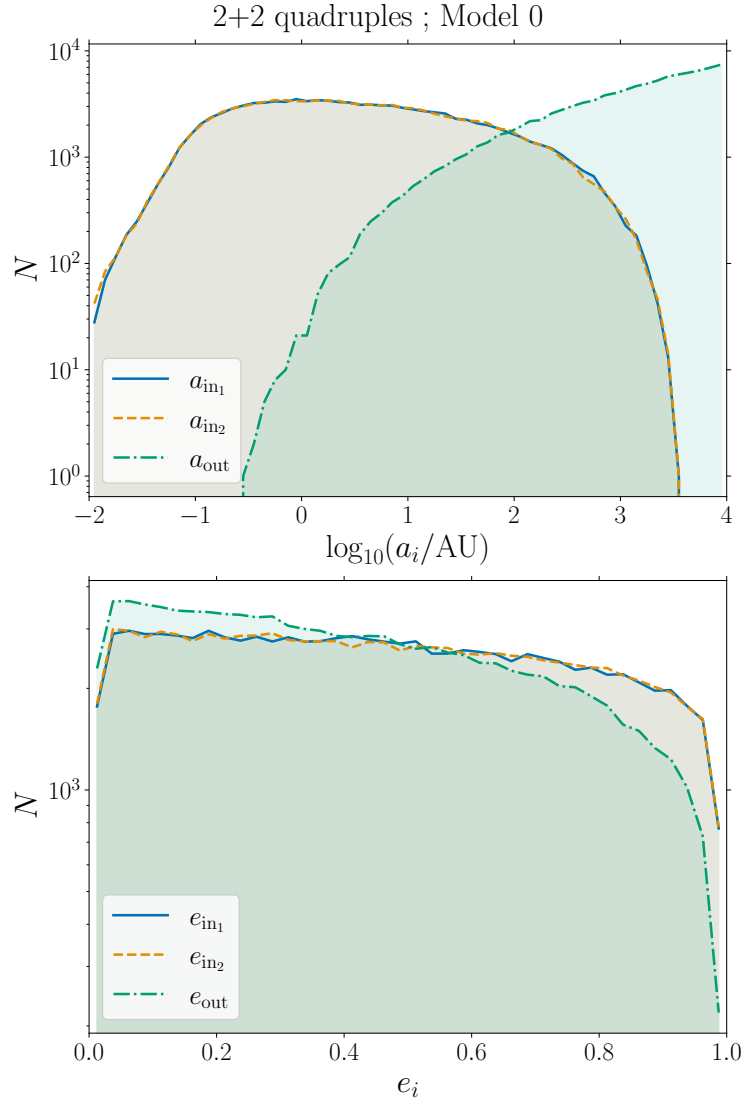


Figure 2.7: Initial semi-major axis and eccentricity distribution of  $10^5$  2+2 quadruple systems for all models. Subscripts ‘in<sub>1</sub>’ and ‘in<sub>2</sub>’ refer to the inner binaries, and ‘out’ refers to the outer binary (see Figure 1.2).

In 3+1 quadruples, the primary mass can be (1) one of the inner stars (twice as likely as the other two cases), (2) the intermediate star or (3) the outer star. In the first case, we sample the immediate companion and the other two stars in a way similar to that of the 2+2 quadruples ( $q = m_{\text{in}_2}/m_{\text{in}_1} < 1$ ). In the second case, the immediate companion of the primary is the inner binary, whose mass is sampled from a flat mass ratio distribution  $\sim U(0, 2)$  with respect to the primary ( $q = (m_{\text{in}_1} + m_{\text{in}_2})/m_{\text{mid}} < 2$ ). Then, this mass is split between the two inner stars as described in the case of 2+2 quadruples. The outer mass is sampled from the total mass of the inner triple. In the third case, the companion of the primary is the inner

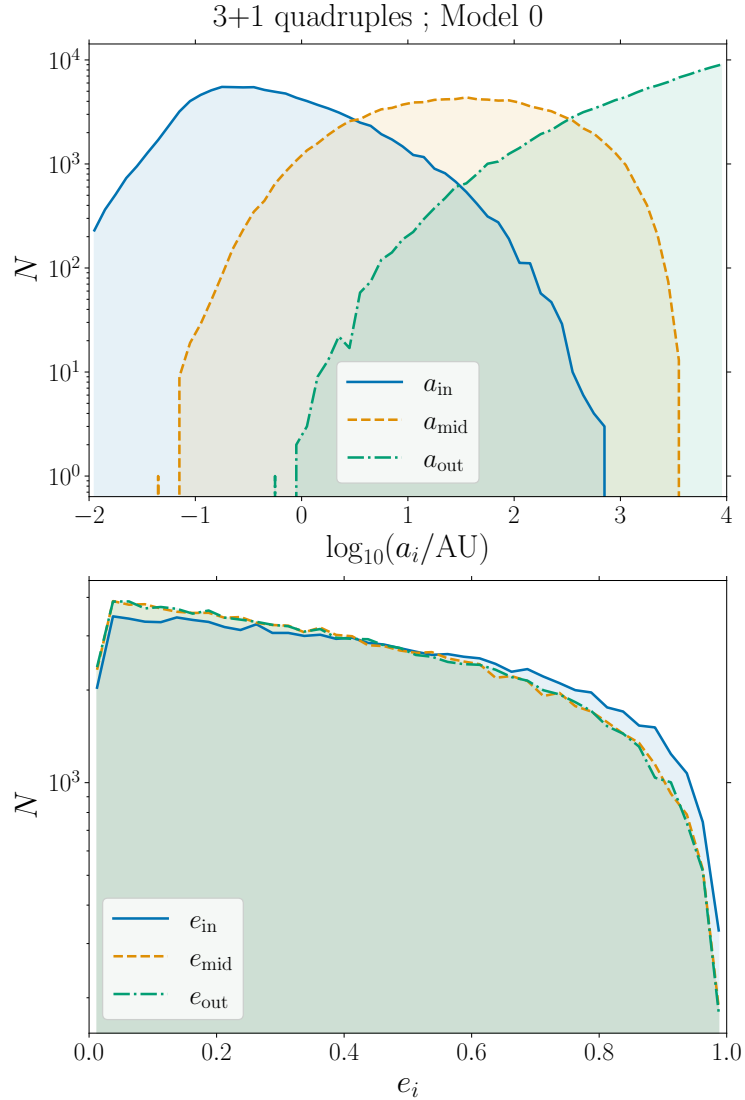


Figure 2.8: Initial semi-major axis and eccentricity distribution of  $10^5$  3+1 quadruple systems for all models. Subscripts ‘in’, ‘mid’ and ‘out’ refer to the inner, intermediate and outer binaries respectively (see Figure 1.2).

triple, and is sampled from a flat mass ratio distribution  $\sim U(0, 3)$  with respect to the primary ( $q = (m_{\text{in}_1} + m_{\text{in}_2} + m_{\text{mid}})/m_{\text{out}} < 3$ ). The individual star masses are then split as before.

In each of the samplings, we check that every star has a minimum mass of  $0.08 M_{\odot}$  and a maximum mass equal to that of the primary. If not satisfied, the sampling is done again. The obtained mass distributions are shown in Figure 2.5 (for 2+2 quadruples; all models) and 2.6 (for 3+1 quadruples; all models).

- *Semi-major axis sampling:* The  $a_i$ s are sampled independent of each other, from a

log flat distribution (Sana et al., 2012), ranging from  $10^{-2}$  AU to  $10^4$  AU. However, the final stability check is biased towards more hierarchical orbits, which is seen in Figures 2.7 (for 2+2 quadruples; all models) and 2.8 (for 3+1 quadruples; all models).

- *Eccentricity sampling:* The  $e_i$ s are also sampled independent of each other, from a flat distribution (Duchêne & Kraus, 2013), ranging from 0.01 to 0.99. The final stability check is biased towards lower eccentricities, especially the outer ones, which is seen in Figures 2.7 (for 2+2 quadruples; all models) and 2.8 (for 3+1 quadruples; all models). The flat distribution of eccentricities is chosen over the commonly adopted thermal distribution (Jeans, 1919).
- *Orbital angles sampling:* The orbital angles are sampled such that the orbits are distributed isotropically in 3D space. The  $i_i$ s are hence distributed uniformly in  $\cos i$ , whereas the  $\Omega_i$ s and the  $\omega_i$ s are distributed randomly from 0 to  $2\pi$ .

Studies have shown that orbital alignment in multiple-star systems is not always isotropic. Tokovinin (2017) showed that, while low-mass triples with wider outer orbits are nearly isotropic, tighter triples are more aligned to an orbital plane. However, the study also showed that high-mass triples do not show as significant an alignment. Hence, our assumption of isotropy is justified.

### 2.4.3 Other parameters and assumptions

There are various parameters, other than the initial conditions, which significantly affect MSE’s results. Since MSE does not model the detailed stellar structure, many parameter values are either prescription-dependent or assumed. Some of the important parameters, and the assumptions involved, are mentioned below.

- *Supernova kicks:* The default SNe kick distribution in MSE is Maxwellian for both NSs and BHs. Here,  $\sigma_{\text{NS}} = 265 \text{ km s}^{-1}$  (Hobbs et al., 2005) and  $\sigma_{\text{BH}} = 50 \text{ km s}^{-1}$ . In our models with SNe kicks (all except Model 1), we use the default distribution.
- *Fly-bys:* MSE samples stars passing by the multiple-star system assuming a homogeneous stellar background of solar density ( $n_{\star} = 0.1 \text{ pc}^{-3}$ ) and a Maxwellian distribution of stellar velocities, with dispersion  $\sigma_{\star} = 30 \text{ km s}^{-1}$ , consistent with the Solar neighborhood (Binney & Tremaine, 2008; Hamers & Tremaine, 2017). We adopt an encounter sphere radius of  $R_{\text{enc}} = 10^5 \text{ AU}$ , with the perturber masses following the Kroupa distribution. Only impulsive encounters (the orbital velocity is much lower than the velocity of the external star) are assumed to affect the orbits since the effects of secular encounters are usually unimportant in low-density systems in the field (this is different for dense stellar systems, see Heggie, 1975; Heggie & Rasio, 1996; Hamers & Samsing, 2019; and also Section 2.6.2). In our models with fly-bys (all except Model 2), we use this method.



Quantity	Distribution or value
Masses $m$	Primary from Kroupa distribution ( $> 8 M_{\odot}$ ); others as mass ratios of primary
Metallicities $Z$	0.02 ( <i>changed in models 3a and 3b</i> )
Semi-major axes $a$	Log flat distribution ( $10^{-2}$ AU – $10^4$ AU); only stable systems
Eccentricities $e$	Flat distribution (0.01 – 0.99); only stable systems
Inclinations $i$	Flat in $\cos i$
Longitudes of ascending node $\Omega$	Flat distribution ( $0 - 2\pi$ )
Arguments of periapsis $\omega$	Flat distribution ( $0 - 2\pi$ )
Supernova kicks	Maxwellian distribution; $\sigma_{\text{NS}} = 265 \text{ km s}^{-1}$ and $\sigma_{\text{BH}} = 50 \text{ km s}^{-1}$ ( <i>0 for model 1</i> )
Fly-bys	$n_{\star} = 0.1 \text{ pc}^{-3}$ ; $\sigma_{\star} = 30 \text{ km s}^{-1}$ (Maxwellian); $R_{\text{enc}} = 10^5 \text{ AU}$ ( <i>0 for model 2</i> )
CE parameters	$\alpha_{\text{CE}=1}$ ; $t_{\text{CE}=10^3 \text{ yr}}$ ( <i>changed in models 4a and 4b</i> )

Table 2.2: Initial conditions and parameters.

- *CE parameters:* MSE uses the energy argument-based  $\alpha$ -CE prescription. The common envelope efficiency  $\alpha_{\text{CE}} = 1$  by default. In this paper, we use three different values for the CE mass-loss timescale  $t_{\text{CE}}$ , as seen in Table 2.1.
- *Collisions:* In MSE, a ‘collision’ between stars is assumed to have occurred when their mutual separation is lesser than the sum of their effective radii. The effective radius is the same as the stellar radius for non-compact objects, whereas it is a factor 100 more for compact objects. This is done since it is computationally expensive to integrate the equations of motion just before a compact object merger, and justified by the very short remaining merger time (see also Hamers et al., 2021a, Eq. 108).

Table 2.2 summarizes the initial conditions and adopted parameters.

## 2.5 Results

In Section 2.5.1, we define quantities of interest pertaining to compact object mergers. In Section 2.5.2, we present the compact object merger numbers for both 2+2 quadruples and isolated binaries, for direct comparison. In Section 2.5.3, we do the same for 3+1 quadruples. In Sections 2.5.4 and 2.5.5, we discuss in detail merger scenarios and rates respectively. Finally, in Section 2.5.6, we talk about systems which are ignored in this study.

### 2.5.1 Definitions of certain quantities

One of the most important features of a compact object merger is the eccentricity  $e_{\text{LIGO}}$  in the LIGO band. Firstly, we have the analytical relation between  $a$  and  $e$  due to GW emission given by (Peters, 1964):

$$a(e) = C_0 \frac{e^{12/19}}{1 - e^2} \left[ 1 + \frac{121}{304} e^2 \right]^{870/2299} \quad (2.2)$$

where  $C_0$  depends on the initial values  $a_0$  and  $e_0$ . We also have a relation for the GW peak frequency for given  $a$ ,  $e$  and total mass  $M = m_1 + m_2$  from Wen (2003):

$$f_{\text{GW}}(a, e, M) = \frac{\sqrt{GM}}{\pi} \frac{(1 + e)^{1.1954}}{[a(1 - e^2)]^{1.5}} \quad (2.3)$$

Using these equations and adopting  $f_{\text{LIGO}} = 10 \text{ Hz}$ , we can calculate  $e_{\text{LIGO}}$ .

Another feature of a LIGO detection is the effective spin parameter  $\chi_{\text{eff}}$ :

$$\chi_{\text{eff}} = \frac{\chi_1 m_1 (\hat{\mathbf{S}}_1 \cdot \hat{\mathbf{L}}) + \chi_2 m_2 (\hat{\mathbf{S}}_2 \cdot \hat{\mathbf{L}})}{m_1 + m_2} \quad (2.4)$$

where  $\hat{\mathbf{S}}_1$  and  $\hat{\mathbf{S}}_2$  are the unit spin angular momentum vectors of the two compact objects with  $\chi_i = c \|\vec{\mathbf{S}}_i\| / Gm_i^2$  lying between 0 and 1 ( $c$  and  $G$  have their usual meaning), and  $\hat{\mathbf{L}}$  is the unit Newtonian orbital angular momentum. We assume that the spins during compact object formation  $\chi_1$  and  $\chi_2$  are sampled uniformly between 0 and 1. It should be noted that assuming a different range for  $\chi_i$  results only in a horizontal re-scaling, while the distribution shape remaining the same (e.g. Hamers et al., 2021b show this for the range 0 to 0.1).

We also calculate another spin parameter, the spin precession parameter  $\chi_p$  (Schmidt et al., 2015; Abbott et al., 2020):

$$\chi_p = \max \left\{ \chi_1 \|\hat{\mathbf{S}}_{1\perp}\|, \kappa \chi_2 \|\hat{\mathbf{S}}_{2\perp}\| \right\} \quad (2.5)$$

where  $\hat{\mathbf{S}}_{i\perp} = \hat{\mathbf{S}}_i - (\hat{\mathbf{S}}_i \cdot \hat{\mathbf{L}}) \hat{\mathbf{L}}$  (component of  $\hat{\mathbf{S}}_i$  perpendicular to  $\hat{\mathbf{L}}$ ) and  $\kappa = \frac{q(4q + 3)}{4 + 3q}$ .

A final important quantity is the merger mass ratio  $q = m_2/m_1$ , where  $m_1$  and  $m_2$  are the heavier and lighter compact object masses respectively ( $0 < q \leq 1$ ).

### 2.5.2 2+2 quadruples and isolated binaries

Table 2.3 shows the number of compact object mergers, and the Poisson errors, in  $10^5$  and  $2 \times 10^5$  sampled systems, for each model of 2+2 quadruples and isolated binaries, respectively. It also shows the merger rates for the 2+2 quadruples. It is important to note that these isolated binaries are not distributed like ‘real’ binaries, and thus, it is

Model	Description	2+2 quadruples			3+1 quadruples		
		BH-BH	BH-NS	NS-NS	BH-BH	BH-NS	NS-NS
0	Fiducial	156 $\pm$ 13	82 $\pm$ 9	9 $\pm$ 3	32 $\pm$ 6	15 $\pm$ 4	8 $\pm$ 3
1	0 kicks	285 $\pm$ 17	215 $\pm$ 15	351 $\pm$ 19	164 $\pm$ 13	120 $\pm$ 11	44 $\pm$ 7
2	No fly-bys	108 $\pm$ 10	79 $\pm$ 9	10 $\pm$ 3	24 $\pm$ 5	17 $\pm$ 4	8 $\pm$ 3
3a	0.1 $Z_{\odot}$	274 $\pm$ 17	191 $\pm$ 14	20 $\pm$ 4	72 $\pm$ 8	64 $\pm$ 8	17 $\pm$ 4
3b	0.01 $Z_{\odot}$	429 $\pm$ 21	525 $\pm$ 23	51 $\pm$ 7	87 $\pm$ 9	199 $\pm$ 14	31 $\pm$ 6
4a	0.1 $t_{\text{CE},0}$	148 $\pm$ 12	72 $\pm$ 8	14 $\pm$ 4	30 $\pm$ 5	19 $\pm$ 4	8 $\pm$ 3
4b	10 $t_{\text{CE},0}$	149 $\pm$ 12	68 $\pm$ 8	10 $\pm$ 3	35 $\pm$ 6	17 $\pm$ 4	8 $\pm$ 3

Model	Description	Isolated binaries		
		BH-BH	BH-NS	NS-NS
0	Fiducial	168 $\pm$ 13	80 $\pm$ 9	14 $\pm$ 4
1	0 kicks	272 $\pm$ 16	194 $\pm$ 14	346 $\pm$ 19
2	No fly-bys	130 $\pm$ 11	52 $\pm$ 7	8 $\pm$ 3
3a	0.1 $Z_{\odot}$	309 $\pm$ 18	197 $\pm$ 14	28 $\pm$ 5
3b	0.01 $Z_{\odot}$	477 $\pm$ 22	619 $\pm$ 25	45 $\pm$ 7
4a	0.1 $t_{\text{CE},0}$	171 $\pm$ 13	79 $\pm$ 9	14 $\pm$ 4
4b	10 $t_{\text{CE},0}$	171 $\pm$ 13	79 $\pm$ 9	14 $\pm$ 4

Table 2.3: Number of compact object mergers in  $10^5$  2+2 and 3+1 quadruples, and  $2 \times 10^5$  isolated binaries.

irrelevant to consider their rates. Their numbers should be considered only as a direct comparison to 2+2 quadruples, and not out of this context.

The table shows that the corresponding number of mergers in both cases (bound vs. unbound 2+2 quadruples) are mostly within the Poisson error margin of each other. However, we can see that isolated binaries consistently produce a higher number of mergers in all models except Model 1 (where SNe kicks are disabled). This may be due to secular evolution driving mergers in 2+2 quadruples in the pre-compact object phases. For example, an isolated inner binary of a 2+2 quadruple could lead to a BH-BH merger, whereas the same inner binary in a bound system could see a merger before the component stars evolve into BHs due to eccentricity excitation.

Let us look at the numbers for each model in detail.

- *Model 0*: The number of BH-BH mergers is higher than that of BH-NS mergers, which in turn is significantly higher than that of NS-NS mergers. The very low merger rates for NS-NS binaries can be attributed to their high SNe kicks, which tend to unbind orbits.
- *Model 1*: Excluding SNe kicks has a drastic effect on the number of compact object mergers, especially the NS-NS mergers, for both 2+2 quadruples and isolated binaries. This is expected since SNe kicks almost always result in the unbinding of

orbits, more so for NSs since their kick distribution has a higher  $\sigma$  than that of BHs. Moreover, in 2+2 quadruples, having no SNe kicks means that there can be secular evolution even in the compact object phase. This eccentricity excitation can lead to much higher  $e_{\text{LIGO}}$  values and negative  $\chi_{\text{eff}}$  values. These outlier systems can be seen in Figures 2.9 and 2.10 (b) & (f) [Model 1 quadruples], but not in (a) & (e) [Model 0 quadruples] or (d) [Model 1 binaries].

- *Model 2:* Excluding fly-bys systematically reduces the total number of mergers. This is most prominent in the BH-BH merger numbers for both 2+2 quadruples and isolated binaries. The similar numbers for BH-NS and NS-NS mergers (in the quadruples case) may be attributed to the higher SNe kicks for NSs, which can diminish the effect of fly-bys. It is important to note that, while an external perturbation can destabilize a wide orbit, it can also decrease the outer periapsis distance, triggering stronger secular evolution with its inner orbits. In short, the general consequence of fly-bys is not immediately clear. Parameter distributions for Model 2 are roughly similar to those from Model 0.
- *Models 3a and 3b:* Reducing  $Z$  from the default  $Z_{\odot} = 2 \times 10^{-2}$  significantly increases the number of mergers. This is expected since lower  $Z$  stars are more compact than higher  $Z$  stars, thereby reducing the chances of pre-compact object phase merger events. Moreover, the maximum BH masses are also significantly higher than those in Model 0 since lower  $Z$  stars lose less mass due to stellar winds. This effect is seen by comparing Figures 2.13 (b) [Model 3a] and (c) [Model 3b] with (a) [Model 0].
- *Models 4a and 4b:* Changing  $t_{\text{CE}}$  from the default  $10^3$  yr does not seem to change the overall statistics of the mergers. This may be somewhat unexpected since  $t_{\text{CE}}$  affects the number of bound stars after CE evolution. However, since secular evolution does not play a dominant role (see Figure 2.15), whether or not the outer orbits in the multiple system remain bound is not important. Hence, the impact of  $t_{\text{CE}}$  tends to be small. Merger numbers for Models 4a and 4b are roughly similar to those from Model 0.

Figures 2.9, 2.10, 2.11 and 2.12 show the  $e_{\text{LIGO}}$ ,  $\chi_{\text{eff}}$ ,  $\chi_{\text{p}}$  and  $q = m_2/m_1$  ( $m_1 \geq m_2$ ) distributions respectively, for Models 0 and 1 of different system configurations. Figure 2.13 shows the scatter plots of the heavier vs. the lighter compact object masses for Models 0, 3a and 3b of the 2+2 quadruples. Finally, Figure 2.14 shows the  $t_{\text{delay}}$  (time duration between the ZAMS phase and the final merger) distributions for Models 0 and 1 of the quadruple configurations.

We see a clear difference between 2+2 quadruples and isolated binaries in the distributions of  $e_{\text{LIGO}}$  for Model 1. Typically,  $e_{\text{LIGO}}$  lies in the range  $10^{-3.5}$ – $10^{-2.5}$ , due to the orbits circularising from CE evolution and GW emission. Yet, we see that excluding SNe kicks has the effect of obtaining higher  $e_{\text{LIGO}}$  values ( $\gtrsim 10^{-2}$ ). These high values can be solely attributed to secular evolution in the compact object phase (see Example 2 in Section 2.3) since a similar effect is not seen in the binaries.

Likewise, for systems in which CE evolution dominates, the  $\chi_{\text{eff}}$  of a merger product is expected to be distributed in the range 0–1. This is because the natal spins  $\chi$  of the progenitors are assumed to lie uniformly in the range 0–1, and the spins and orbits were initially assumed to be aligned. This is different when SNe kicks are excluded, in which case negative  $\chi_{\text{eff}}$  can be explained by secular evolution – an orbit’s eccentricity and inclination can fluctuate, and hence, the spin-orbit orientation can vary. These secular evolution effects are not seen in Model 0, where SNe kicks are included. The distributions of  $e_{\text{LIGO}}$  and  $\chi_{\text{eff}}$  are qualitatively similar for BH-BH, BH-NS, and NS-NS mergers.

The  $\chi_{\text{p}}$  (Figure 2.11) distribution is dependent on the  $q$  values.  $\chi_{\text{p}}$  is related to the spin component in the orbital plane (unlike  $\chi_{\text{eff}}$ , which is related to the perpendicular component), and hence is relevant in quantifying the precession of the orbit. Our distribution shows that  $\chi_{\text{p}}$  is spread throughout the parameter space, but with a preference for small  $\chi_{\text{p}}$  ( $\sim 0$ ). For Model 0 of 3+1 quadruples, high  $\chi_{\text{p}}$  values are not seen, which may be due to the few mergers in this case. The preference for  $\chi_{\text{p}} \sim 0$  can be attributed to the dominance of isolated binary evolution: in our simulations, the stellar spins were assumed to be aligned with the orbit, implying initially zero component of the spin to the orbit. Dynamical evolution can change the orbital orientations and hence increase  $\chi_{\text{p}}$ , and there are indeed more systems with larger  $\chi_{\text{p}}$  in Model 1 (no kicks; secular evolution is more important) compared to Model 0.

The  $q$  distribution (Figure 2.12) itself is dependent on the type of merger. NS-NS mergers have  $q \gtrsim 0.5$ , peaking at  $\sim 1$ , since all NSs have masses greater than the Chandrasekhar mass  $\sim 1.4 M_{\odot}$  and lower than  $\sim 3 M_{\odot}$  (the approximate lower limit for the BH mass). BH-NS mergers typically have low  $q$  values because a BH is much heavier than an NS. The BH-BH distribution seems to be roughly flat, with not much of a skew ( $q \gtrsim 0.3$ ). Metallicity is important in determining the final compact object masses. This is seen in Figure 2.13, where the models with lower metallicities (Models 3a and 3b) consistently produce very high mass BHs ( $\gtrsim 17 M_{\odot}$ , up to  $\sim 27 M_{\odot}$ ).

The final distribution we look at is of the delay time  $t_{\text{delay}}$  (Figure 2.14). All compact object mergers take  $\gtrsim 10$  Myr to merge. As mentioned before, we limit our simulations up to 14 Gyr (Hubble time). We do not notice any significant preferences relating to  $t_{\text{delay}}$ .

### 2.5.3 3+1 quadruples

Table 2.3 shows the number of compact object mergers, along with the Poisson error, in  $10^5$  3+1 quadruple systems. The table shows that the number of mergers in 3+1 quadruples is significantly lower than in 2+2 quadruples (almost by a factor of 5 for Model 0). This is not surprising since stable 3+1 configurations need to be more hierarchical and can get destabilized more easily. Additionally, we can see that models 1 (zero SNe kicks) and 3a/3b (lower metallicities) host a much higher proportion of mergers than in the case of the 2+2 quadruples. This, again, is due to the susceptibility of 3+1 quadruples to get unbound, for example, due to even small SNe kicks. The details of individual models have similar explanations as in the case of 2+2 quadruples while keeping the above points in mind.

We refer to the Figures 2.9, 2.10, 2.11, 2.12 and 2.14 for the distributions of  $e_{\text{LIGO}}$ ,

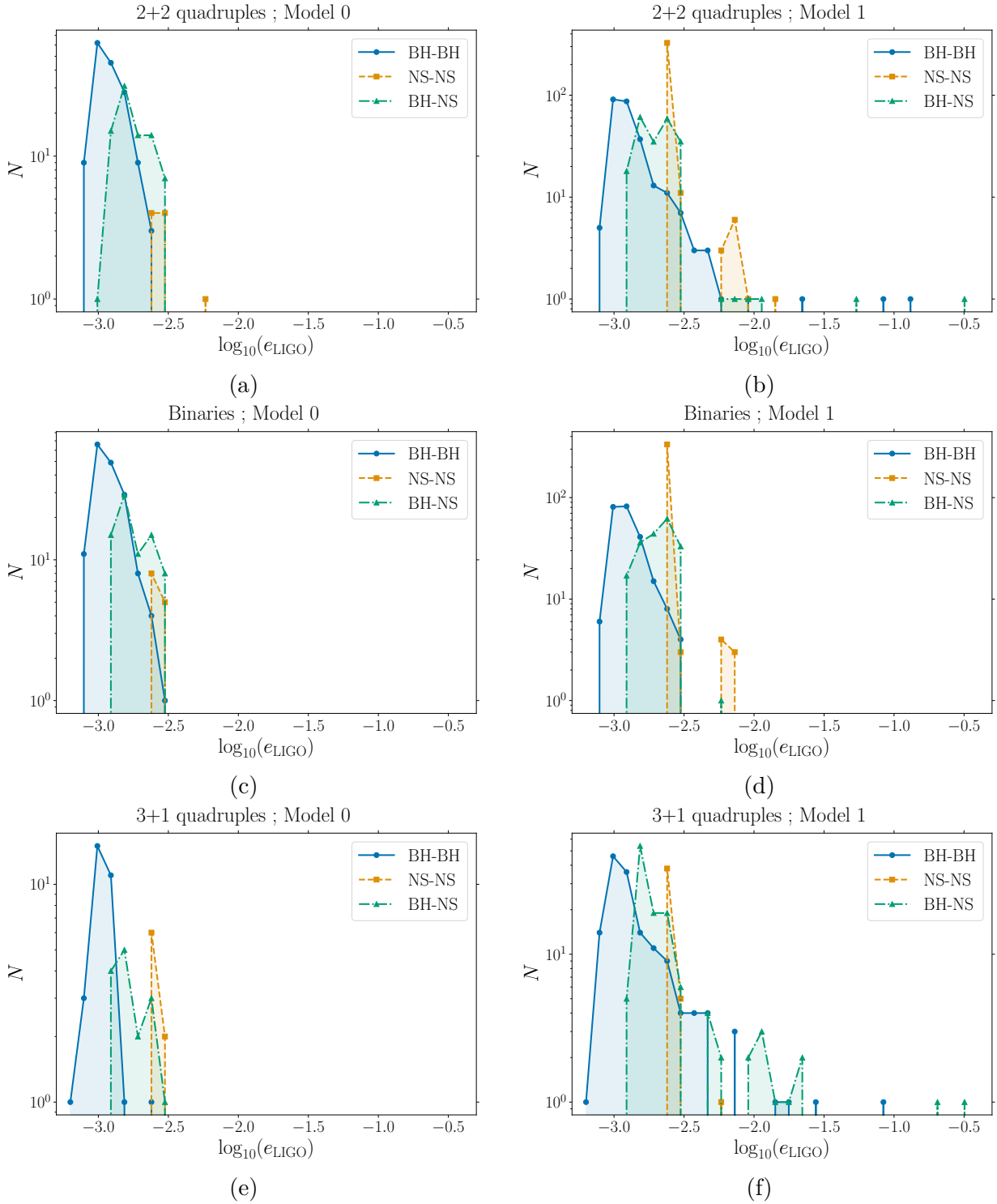


Figure 2.9: Frequency polygon of LIGO-band eccentricities  $e_{\text{LIGO}}$ . [Rows correspond to 2+2 quadruples, binaries and 3+1 quadruples respectively; Columns correspond to Models 0 and 1 respectively.] The quadruples have a significant tail at high  $e_{\text{LIGO}}$  values for Model 1, whereas the binaries do not.

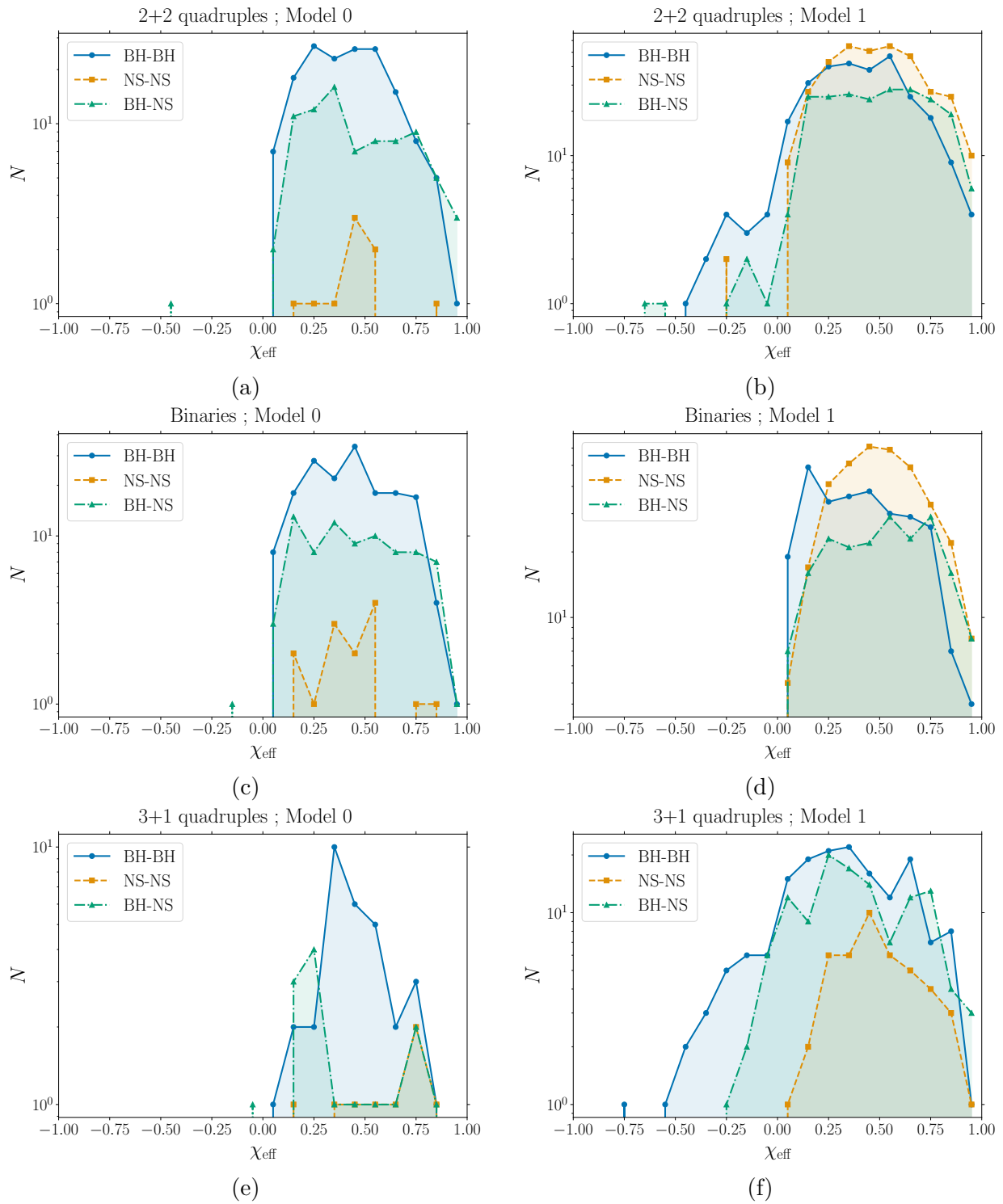


Figure 2.10: Frequency polygon of effective spins  $\chi_{\text{eff}}$ . [Rows correspond to 2+2 quadruples, binaries and 3+1 quadruples respectively; Columns correspond to Models 0 and 1 respectively.] The quadruples have a significant tail at negative  $\chi_{\text{eff}}$  values for Model 1, whereas the binaries do not.

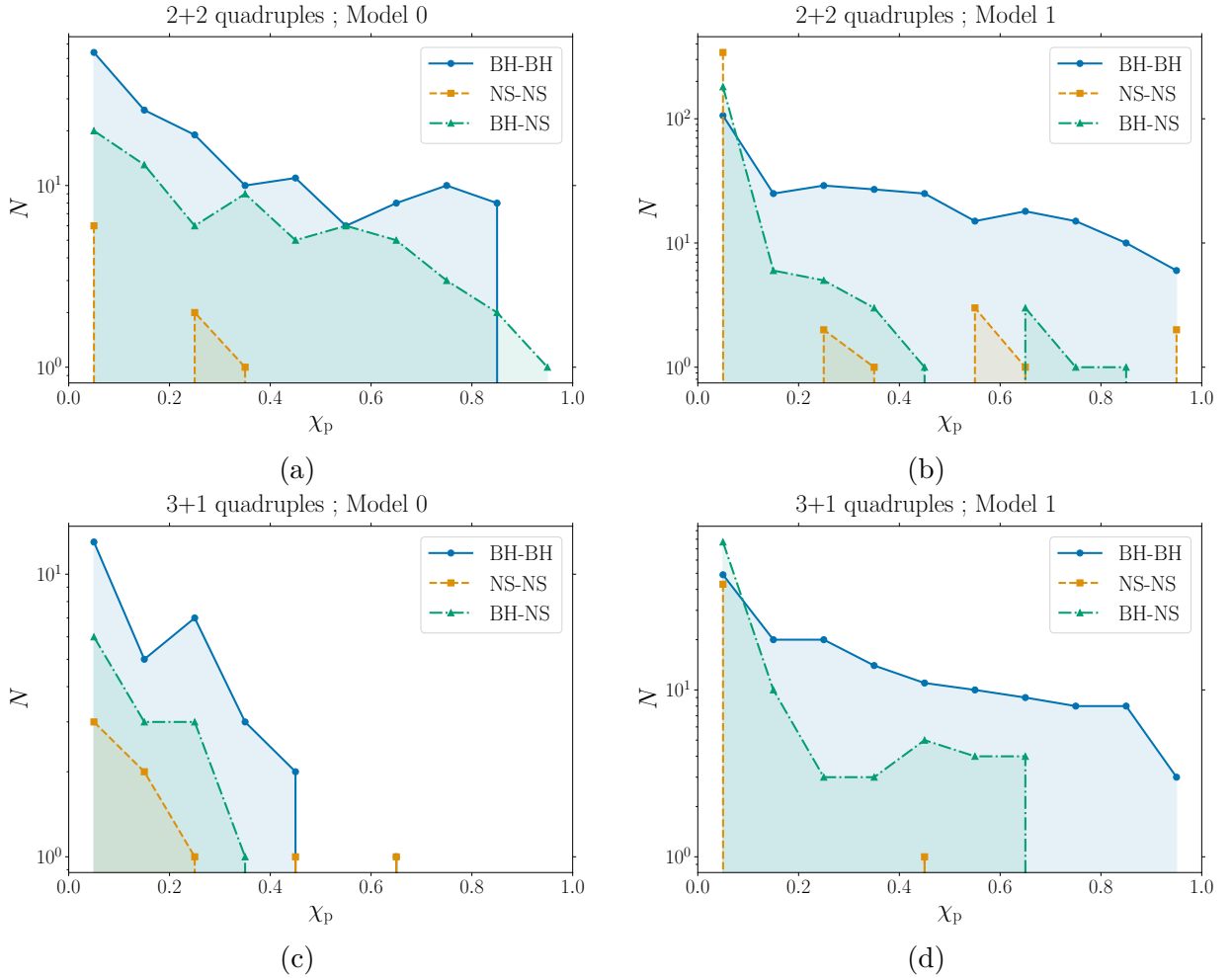


Figure 2.11: Frequency polygon of the spin precession parameters  $\chi_p$ . [Rows correspond to 2+2 and 3+1 quadruples respectively; Columns correspond to Models 0 and 1 respectively. Isolated binary profiles are similar to 2+2 quadruples.] For comparison,  $\chi_p$  for LIGO events GW190814 and GW190425 are  $\lesssim 0.07$  and  $0.30^{+0.19}_{-0.15}$  respectively.

$\chi_{\text{eff}}$ ,  $\chi_p$ ,  $q$  and  $t_{\text{delay}}$ . The  $e_{\text{LIGO}}$  and  $\chi_{\text{eff}}$  distributions for Model 1 show the outlier effect (seen in 2+2 quadruples; see section 2.5.2) characteristic to secular evolution. The other distributions also qualitatively follow the 2+2 quadruples, albeit with fewer data points. Thus, it is not possible to distinguish between 2+2 and 3+1 quadruples based on the parameter distributions alone.

### 2.5.4 Scenarios of mergers

In this section, we look back on the three merger scenarios referred to in Section 2.3 - *Only CE evolution* (Scenario 1), *Only secular evolution* (Scenario 2) and *Mixture of both* (Scenario 3). An attempt is made to estimate the fraction of merger systems that belong



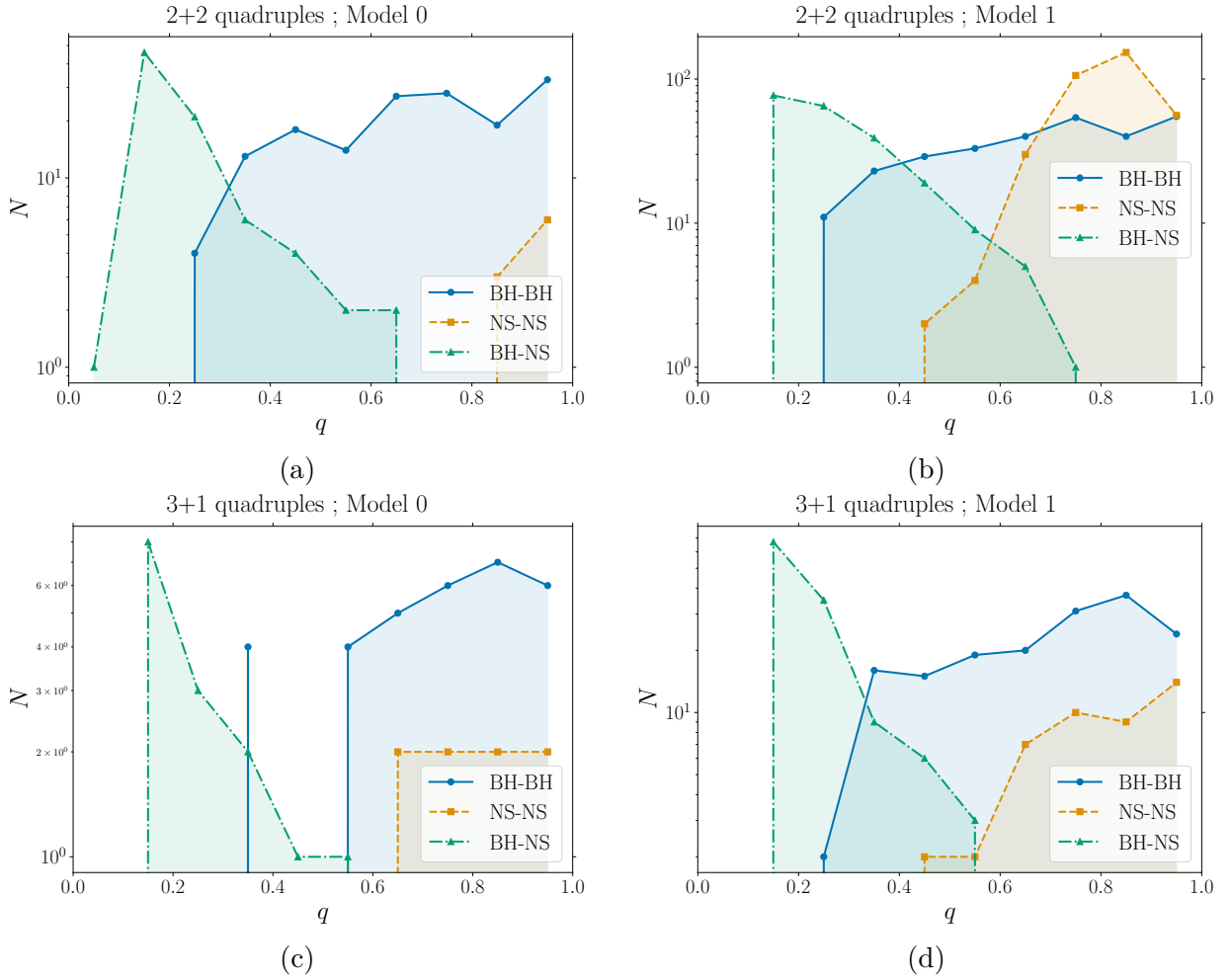


Figure 2.12: Frequency polygon of mass ratios  $q$  pre-merger. [Rows correspond to 2+2 and 3+1 quadruples respectively; Columns correspond to Models 0 and 1 respectively. Isolated binary profiles are similar to 2+2 quadruples.]

in each of these scenarios. It should, however, be noted that the distinction made between Scenarios 1 and 3 may not be unique, since it is generally difficult to quantify whether or not secular evolution played a decisive role.

The classification is as follows. Any merger system which does not undergo any CE or triple CE event throughout its evolution is considered in Scenario 2. The rest of the systems have a CE event at some point in their evolution. The distinction between Scenarios 1 and 3 is more arbitrary. To see if a system has been affected by secular evolution, we check for changes in the periastris distance  $r_p$  in the early stages of evolution. More specifically, the following conditions need to be satisfied by the inner or intermediate (in 3+1 quadruples) binaries to be classified under Scenario 3:  $r_p < 0.8 r_{p,0}$  and  $r_{p,0} > 5 \text{ AU}$ . Here,  $r_{p,0}$  is the inner or intermediate periastris at  $t = 0$ , and this condition is checked for the first three log entries of MSE (a time step in MSE is ‘logged’ when there are important events – stellar

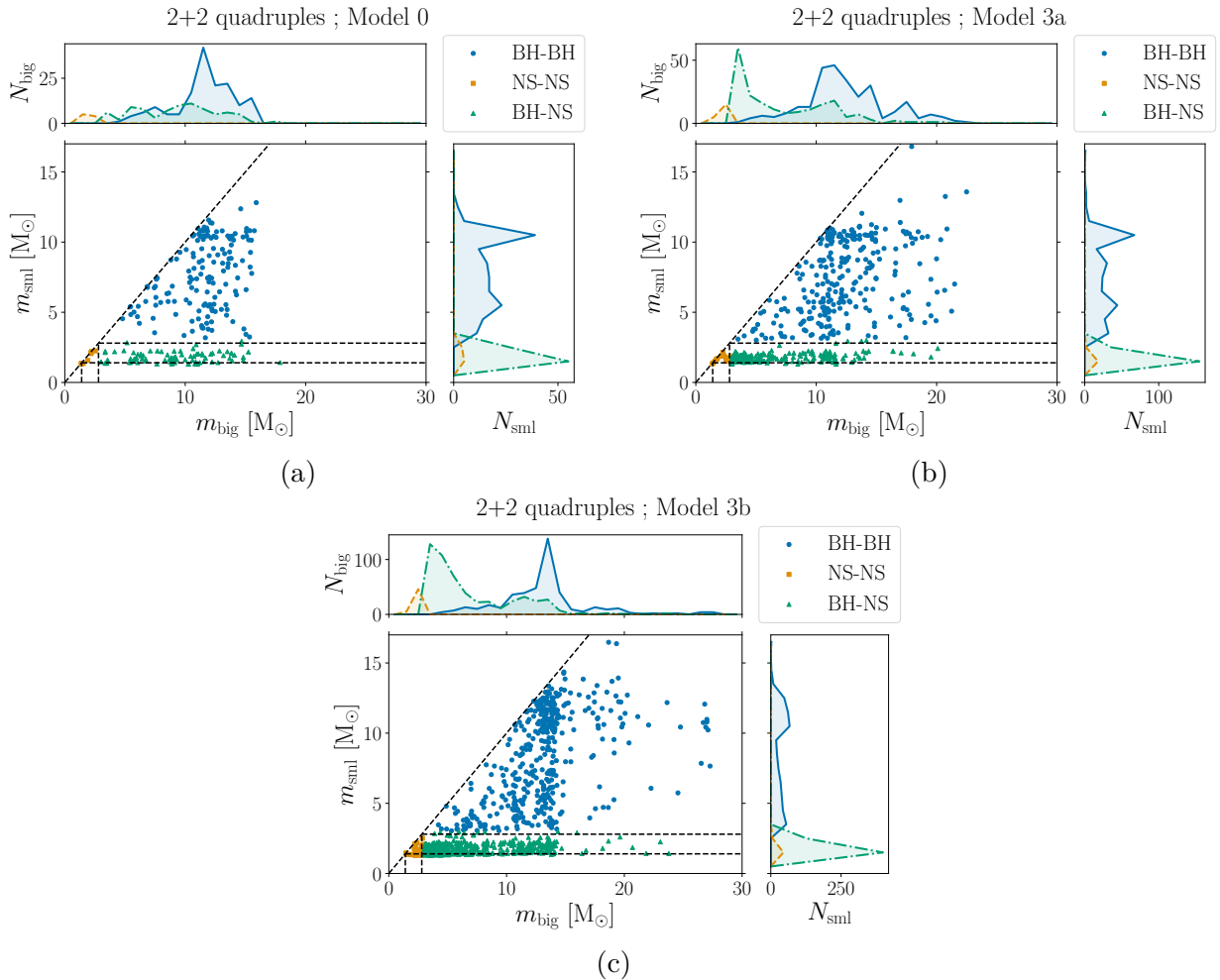


Figure 2.13: Scatter plot of heavier ( $m_{\text{big}}$ ) and lighter ( $m_{\text{sml}}$ ) compact object masses pre-merger. [Rows correspond to Models 0, 3a and 3b respectively.]

type changes, supernovae, RLOF or CE events, collisions, dynamical instabilities, etc.). Any system which does not satisfy these conditions is considered in Scenario 1.

The resulting scenario fraction are presented in Figure 2.15. In every model other than Model 1, Scenario 3 contributes to (15–30) % of all compact object mergers. The rest are contributed by Scenario 1. 3+1 quadruples have a systematically higher contribution from Scenario 2 as well, most likely because there is more room for secular interactions. Unlike in 2+2 quadruples, the 3+1 quadruples have an intermediate orbit whose eccentricity and inclination can change, which can, in turn, affect the eccentricity and inclination of the inner orbit. Model 1 is the only one where Scenario 2 is observed – 3 % and 10 %, respectively, in 2+2 and 3+1 quadruples. This exemplifies how much SNe kicks affect the evolution of quadruple-star systems.

We stress that our estimated percentages may not represent the true fraction of systems affected by secular evolution. Firstly, our periapsis condition is checked only for the first

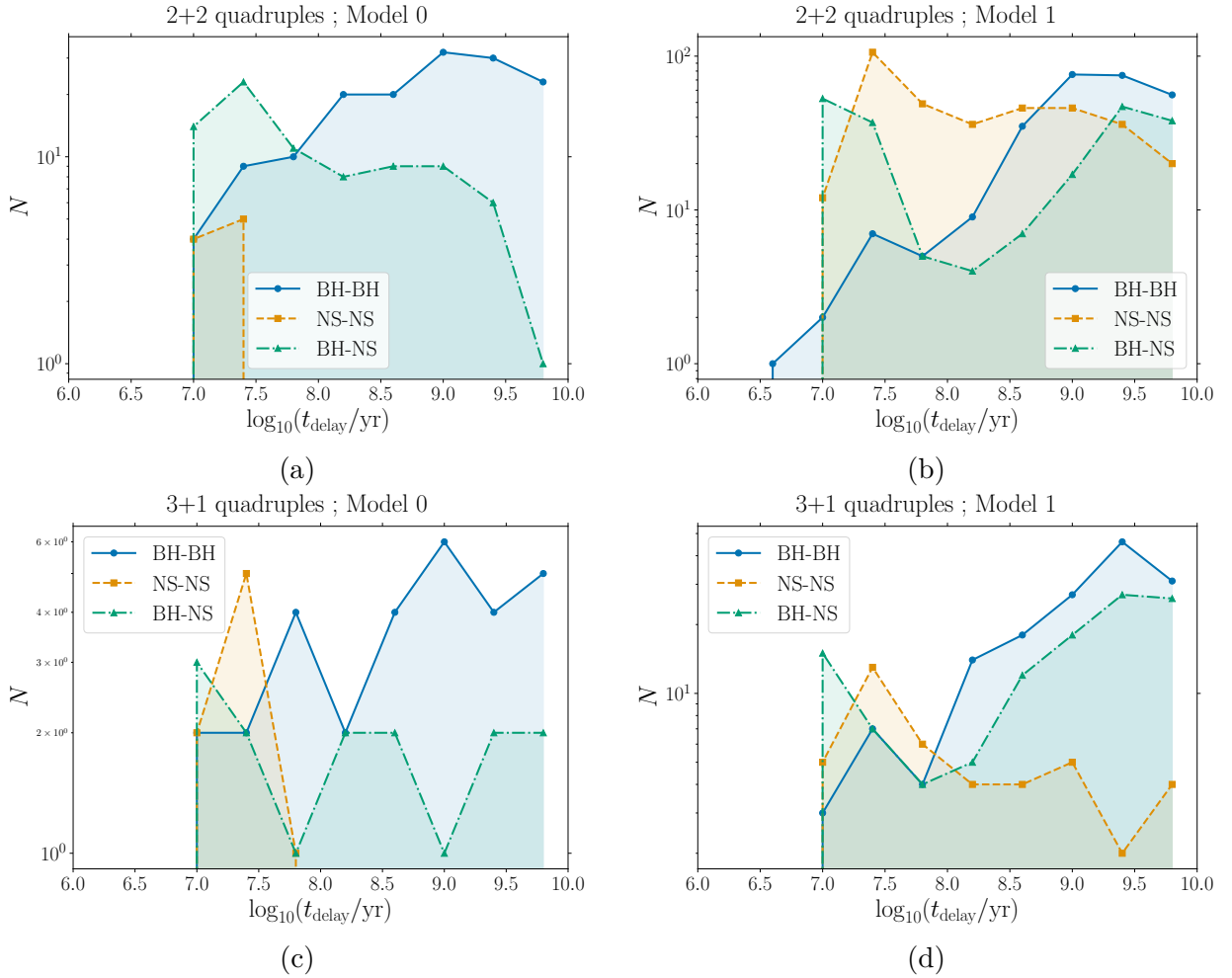


Figure 2.14: Frequency polygon of delay time  $t_{\text{delay}}$  of merger. [Rows correspond to 2+2 and 3+1 quadruples respectively; Columns correspond to Models 0 and 1 respectively. Isolated binary profiles are similar to 2+2 quadruples.]

few log entries. Any future secular evolution effects due to changed inclinations are not taken into account. Thus, the Scenario 3 fraction might be underestimated. Secondly, secular evolution does not aid all the merger systems in Scenario 3. For example, in 2+2 quadruples, one of the inner binary eccentricities might be enhanced, while the actual merger takes place in the other inner binary. In these cases, the Scenario 3 fraction might be overestimated. Nonetheless, Scenario 2 is unambiguously defined and, in particular, shows that the overall fraction of systems in which ‘clean’ secular evolution leads to compact object mergers is very small.

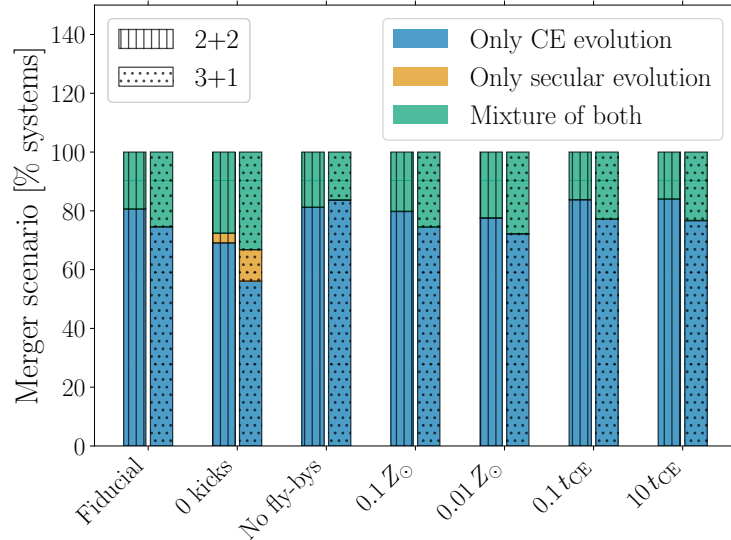


Figure 2.15: Bar graph of percentages of the three scenarios of compact object mergers in 2+2 and 3+1 quadruples.

### 2.5.5 Merger rate calculation

Our population synthesis systems do not represent the whole parameter space of quadruple-star systems, let alone all types of stellar systems. Thus, we need to take into consideration the assumptions made to get a realistic estimate for compact object merger rates. We employ a rate calculation method similar to the one used by Hamers et al. (2013).

The star formation rate (SFR) at redshift  $z = 0$  is assumed to be  $R_{\text{SF}} = 1.5 \times 10^7 \text{ M}_{\odot} \text{ Gpc}^{-3} \text{ yr}^{-1}$  (given by Madau & Dickinson, 2014). The overall merger rate  $R_{\text{merge;conf}}$  for a given model of a given quadruple configuration can be expressed by the following equation:

$$\begin{aligned}
 R_{\text{merge;conf}} &\sim R_{\text{SF}} \frac{N_{\text{merge;conf}}}{M_{\text{sim}}} \\
 &\sim \frac{R_{\text{SF}}}{N_{\text{sample}}} \frac{N_{\text{merge;conf}} F_{\text{quad;conf}}}{M_{\text{avg}}}
 \end{aligned}
 \tag{2.6}$$

where  $N_{\text{sample}} = 10^5$  (total number of sampled systems in each model),  $N_{\text{merge;conf}}$  values are given in Table 2.3 for given model and configuration (2+2 or 3+1) of quadruples,  $M_{\text{sim}}$  is the total mass represented by our simulation,  $M_{\text{avg}}$  is the average system mass of *all types* (singles, binaries, triples and quadruples) and  $F_{\text{quad;conf}}$  is the fraction of parameter space represented by a configuration of quadruples. In our rate normalisation calculations, we neglect the contribution of quintuples and higher-order systems.

Let us first start with the masses. We assume that the universal initial mass function (IMF) is the Kroupa distribution ( $dN/dm \propto m^{-1.3}$ ,  $m < 0.5 \text{ M}_{\odot}$  and  $dN/dm \propto m^{-2.3}$ ,  $m > 0.5 \text{ M}_{\odot}$ ; Kroupa, 2001). We then sample single, binary, triple and quadruple (both types) systems from this IMF as done in Section 2.4.2 and calculate their average masses

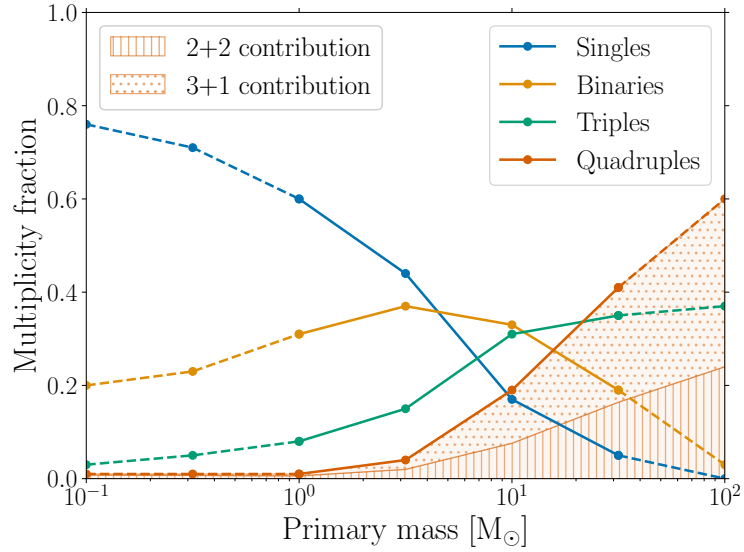


Figure 2.16: Distribution of multiplicity fraction as a function of primary mass. The solid lines are approximate interpolated values from Moe & Di Stefano (2017), while the dotted lines are extrapolations.

$\mu_{\text{sin}}$ ,  $\mu_{\text{bin}}$ ,  $\mu_{\text{trip}}$  and  $\mu_{\text{quad}}$  in different mass bins. Each mass bin also occupies a fraction  $f$  of the IMF. Next, we use interpolated and extrapolated values of multiplicity fractions from Moe & Di Stefano (2017) to calculate the contributions of singles  $\alpha_{\text{sin}}$ , binaries  $\alpha_{\text{bin}}$ , triples  $\alpha_{\text{trip}}$  and quadruples  $\alpha_{\text{quad}}$  to the average system mass  $M_{\text{avg}}$  in these mass bins. These fractions are shown in Figure 2.16. In the case of quadruples, we further separate the contributions  $\lambda_{2+2}$  and  $\lambda_{3+1}$  of 2+2 and 3+1 quadruples respectively. To do this, we analyze the quadruple systems in the comprehensive Multiple Star catalog (MSC) (Tokovinin, 1997, 2018b,a) and calculate fractions of 2+2 and 3+1 quadruples in four mass bins. This is shown in Figure 2.17. It should be mentioned that the MSC suffers from observational biases, but it is currently the best source to infer fractions of the two types of quadruples. Finally, we put these contributions together to give:

$$M_{\text{avg}} = \sum_{m_{\text{bins}}} (f_{\text{sin}}\alpha_{\text{sin}}\mu_{\text{sin}} + f_{\text{bin}}\alpha_{\text{bin}}\mu_{\text{bin}} + f_{\text{trip}}\alpha_{\text{trip}}\mu_{\text{trip}} + f_{\text{quad};2+2}\alpha_{\text{quad}}\lambda_{2+2}\mu_{\text{quad}} + f_{\text{quad};3+1}\alpha_{\text{quad}}\lambda_{3+1}\mu_{\text{quad}}) \quad (2.7)$$

The other quantity in Equation 2.6 is  $F_{\text{quad};\text{conf}}$ :

$$F_{\text{quad};\text{conf}} = \sum_{m_{\text{bins}}} f_{\text{quad};\text{conf}}\alpha_{\text{quad}}\lambda_{\text{conf}} \quad (2.8)$$

The final calculated rates are shown in Table 2.4. The errors indicate the Poisson errors.

### 2.5.6 Systems not considered

Not all of the systems ran completely. For such systems, the code gets stuck either in the direct  $N$ -body or secular integration modes. Thus, we terminate any system which takes

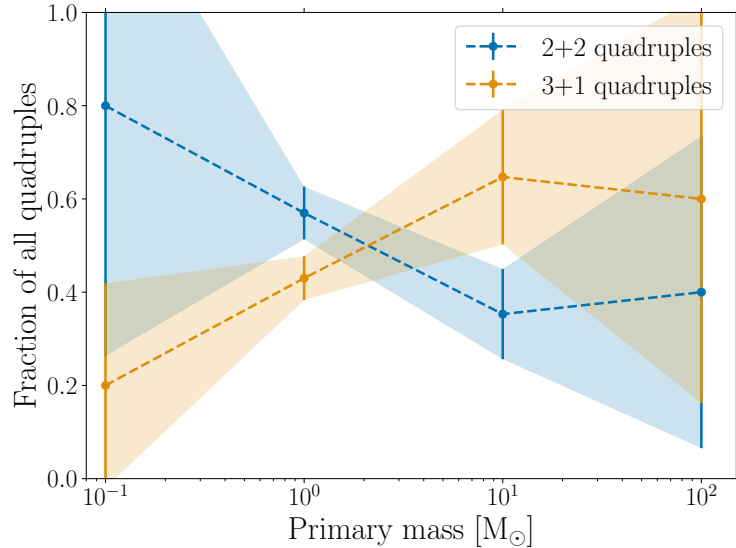


Figure 2.17: Distribution of 2+2 and 3+1 quadruple fraction as a function of primary mass. Systems from the Multiple Star catalog are binned, and the errors are represented by the shaded regions.

longer than a CPU wall time of  $t_{\text{wall}} = 10$  hr to run. We note that this is a reasonable time limit given that many systems take a few seconds to a few minutes to run. For completeness, in Figure 2.18, we present the percentage of systems which take longer than  $t_{\text{wall}}$  to run.

The isolated binary models have the least proportion of such systems (0.1%–0.3%) and the 3+1 quadruples have the most (2.9%–3.5%). The proportion for 2+2 quadruples is midway (0.6%–1.6%). This is expected since dynamical integration is straightforward in binaries while it is most complicated in 3+1 quadruples. In the case of the quadruples, it can be seen that Model 1 has the highest proportion of systems with  $t_{\text{wall}} > 10$  hr. This is because zero SNe kicks aid in keeping more systems bound, and hence, there is a higher

Model	Description	2+2 quadruples [ $\text{Gpc}^{-3} \text{yr}^{-1}$ ]			3+1 quadruples [ $\text{Gpc}^{-3} \text{yr}^{-1}$ ]		
		BH-BH	BH-NS	NS-NS	BH-BH	BH-NS	NS-NS
0	Fiducial	$10.8 \pm 0.9$	$5.7 \pm 0.6$	$0.6 \pm 0.2$	$2.9 \pm 0.5$	$1.4 \pm 0.4$	$0.7 \pm 0.3$
1	0 kicks	$19.7 \pm 1.2$	$14.9 \pm 1.0$	$24.3 \pm 1.3$	$14.8 \pm 1.2$	$10.8 \pm 1.0$	$4.0 \pm 0.6$
2	No fly-bys	$7.5 \pm 0.7$	$5.5 \pm 0.6$	$0.7 \pm 0.2$	$2.2 \pm 0.5$	$1.5 \pm 0.4$	$0.7 \pm 0.3$
3a	$0.1 Z_{\odot}$	$19.0 \pm 1.2$	$13.2 \pm 1.0$	$1.4 \pm 0.3$	$6.5 \pm 0.7$	$5.8 \pm 0.7$	$1.5 \pm 0.4$
3b	$0.01 Z_{\odot}$	$29.7 \pm 1.5$	$36.3 \pm 1.6$	$3.5 \pm 0.5$	$7.8 \pm 0.8$	$17.9 \pm 1.3$	$2.8 \pm 0.5$
4a	$0.1 t_{\text{CE},0}$	$10.2 \pm 0.8$	$5.0 \pm 0.6$	$1.0 \pm 0.3$	$2.7 \pm 0.5$	$1.7 \pm 0.4$	$0.7 \pm 0.3$
4b	$10 t_{\text{CE},0}$	$10.3 \pm 0.8$	$4.7 \pm 0.6$	$0.7 \pm 0.2$	$3.2 \pm 0.5$	$1.5 \pm 0.4$	$0.7 \pm 0.3$

Table 2.4: Merger rates of compact object mergers in 2+2 and 3+1 quadruples.

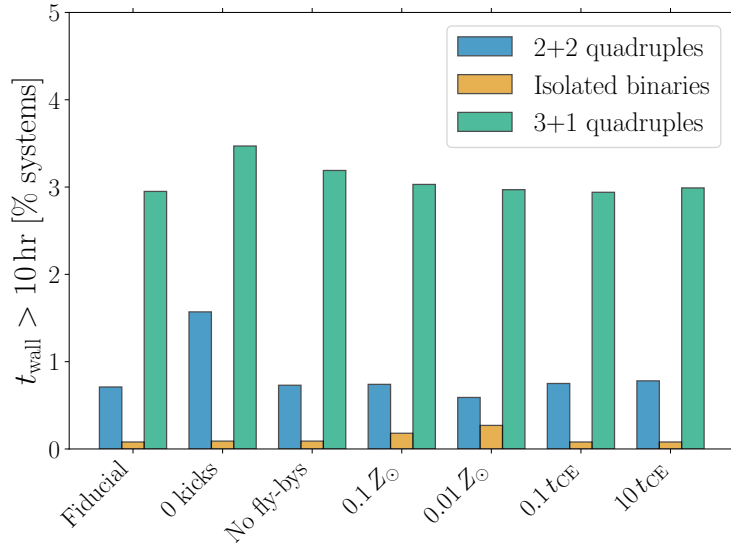


Figure 2.18: Bar graph of percentage of systems for which  $t_{\text{wall}} > 10 \text{ hr}$  in 2+2 quadruples, isolated binaries and 3+1 quadruples.

chance for the gravitational dynamical integration to be slow.

However, more than 96% of the systems in all our models do run completely. Moreover, the offending systems are not clustered but spread throughout our initial parameter space. Hence, our overall statistics are not affected.

## 2.6 Discussion

### 2.6.1 Merger rate comparisons

To put our estimated compact object merger rates in quadruples in context, we mention the compact object merger rates derived from LIGO detections. [Abbott et al. \(2021b\)](#) determined the GWTC-2 BH-BH and NS-NS merger rates to be  $23.9_{-8.6}^{+14.3} \text{ Gpc}^{-3} \text{ yr}^{-1}$  and  $320_{-240}^{+490} \text{ Gpc}^{-3} \text{ yr}^{-1}$  respectively. [Abbott et al. \(2021c\)](#) carried out a similar analysis for BH-NS mergers and found the rate to be  $45_{-33}^{+75} \text{ Gpc}^{-3} \text{ yr}^{-1}$  (assuming the two BH-NS detections are representative of the whole population) or  $130_{-69}^{+112} \text{ Gpc}^{-3} \text{ yr}^{-1}$  (assuming a broader distribution of masses). The rates we observe are either in agreement with the LIGO rates (for BH-BH mergers) or much lower (for NS-NS mergers, and BH-Ns mergers to a lesser extent). Merger rates also depend on star formation rates, which depend on redshift ([Madau & Dickinson, 2014](#)).

Let us now compare with the other theoretical channels of GW emission. Most of these studies only consider BH-BH mergers, of which quadruples can constitute a significant fraction. The high NS-NS merger rates inferred from LIGO detections are not reproduced in many population synthesis studies due to the high SNe kicks attributed to NSs. This is true for our study as well. Generally, dynamical merger channel can have high LIGO band

eccentricities  $e_{\text{LIGO}}$ , and possibly anti-aligned (negative) effective spins  $\chi_{\text{eff}}$ . Many of the below-mentioned rates are uncertain and should be taken as order of magnitude estimates.

- *Isolated binary channel:* [Belczynski et al. \(2016\)](#) estimated a high BH-BH merger rate of  $\sim 200 \text{ Gpc}^{-3} \text{ yr}^{-1}$  within redshift  $z \sim 0.1$ , for their standard model of isolated binary evolution of very massive stars ( $\gtrsim 40 M_{\odot}$ ). In contrast, [de Mink & Mandel \(2016\)](#) predicted a local BH-BH merger rate of  $\sim 10 \text{ Gpc}^{-3} \text{ yr}^{-1}$ , and a rate of  $\sim 20 \text{ Gpc}^{-3} \text{ yr}^{-1}$  at redshift  $z \sim 0.4$ , for chemically homogeneous evolution in tidally distorted massive binaries. Since there is no secular evolution in isolated binaries, LIGO band eccentricities  $e_{\text{LIGO}}$  is very small and  $\chi_{\text{eff}}$  is aligned with their orbits.
- *Dynamical channel in star clusters:* [Rodriguez et al. \(2016\)](#) predicted a local BH-BH merger rate of  $\sim 5 \text{ Gpc}^{-3} \text{ yr}^{-1}$  in globular clusters using a Monte Carlo approach, with 80 % of them being in the mass range  $\sim (30\text{--}60) M_{\odot}$ . They also found that nearly all of the BH-BH systems circularize and have  $e_{\text{LIGO}} \lesssim 10^{-3}$ , similar to isolated binaries. In comparison, [Banerjee \(2017\)](#) used direct  $N$ -body evolution to estimate a LIGO merger BH-BH rate of  $\sim 13 \text{ yr}^{-1}$  within a radius of 1.5 Gpc, which is equivalent to  $\sim 3 \text{ Gpc}^{-3} \text{ yr}^{-1}$ . BH-NS and NS-NS mergers are unlikely since NSs do not efficiently segregate to the center (as BHs do).
- *Dynamical channel in galactic nuclei:* [Petrovich & Antonini \(2017\)](#) estimated BH-BH, BH-NS and NS-NS merger rates of  $\lesssim 15 \text{ Gpc}^{-3} \text{ yr}^{-1}$ ,  $\lesssim 0.4 \text{ Gpc}^{-3} \text{ yr}^{-1}$  and  $\lesssim 0.02 \text{ Gpc}^{-3} \text{ yr}^{-1}$  respectively for binaries in the sphere of influence of the central massive BH (MBHs) in galactic nuclei. They also noted that the fraction of systems that reach extremely high eccentricities ( $1 - e \sim 10^4\text{--}10^6$ ) is  $\sim (10\text{--}100)$  higher than in spherical clusters. The predictions of [Hamers et al. \(2018\)](#) agree with the above, with their most optimistic BH-BH merger rate being  $\sim 12 \text{ Gpc}^{-3} \text{ yr}^{-1}$ . [Hoang et al. \(2018\)](#) predicted lower BH-BH merger rates of  $\sim (1\text{--}3) \text{ Gpc}^{-3} \text{ yr}^{-1}$  using Monte Carlo simulations.
- *Dynamical channel in triple systems:* [Silsbee & Tremaine \(2017\)](#) used a simple triple BH assumption to estimate a merger rate of  $\sim 6 \text{ Gpc}^{-3} \text{ yr}^{-1}$ . On the other hand, [Antonini et al. \(2017\)](#) combined stellar evolution and dynamics to predict BH-BH merger rates of  $\sim (0.3\text{--}1.3) \text{ Gpc}^{-3} \text{ yr}^{-1}$ , with many of the mergers having  $e_{\text{LIGO}} > 10^{-2}$ . For BH-NS mergers, [Fragione & Loeb \(2019\)](#) estimated rates of  $\sim (1.0 \times 10^{-3}\text{--}3.5 \times 10^{-2}) \text{ Gpc}^{-3} \text{ yr}^{-1}$  when natal kicks are included.
- *Dynamical channel in quadruple systems:* [Liu & Lai \(2019\)](#) showed that interactions between the two inner binaries in 2+2 quadruples can result in resonances which can increase the number of mergers by almost an order of magnitude compared to similar triples. Another study by [Fragione & Kocsis \(2019\)](#) (assuming all components are BHs) showed that this factor can be  $\sim (3\text{--}4)$ . [Hamers et al. \(2021b\)](#), who carried a simplified population synthesis of 2+2 quadruples, inferred optimistic rates of  $\sim (10\text{--}100) \text{ Gpc}^{-3} \text{ yr}^{-1}$ , of which the lower limits are consistent with our study. They



also predicted second-generation mergers (see later) at a rate  $\sim 10^{-5} \text{ Gpc}^{-3} \text{ yr}^{-1}$ , which is not seen in our population synthesis (possibly due to low resolution). As in the case of triples, all these studies see a non-negligible fraction of mergers with high  $e_{\text{LIGO}}$ . Moreover, [Hamers et al. \(2021b\)](#) noted some merger products with negative  $\chi_{\text{eff}}$ .

- *AGN disk channel:* [Bartos et al. \(2017\)](#) and [Stone et al. \(2017a\)](#) calculated BH-BH merger rates of  $\sim 1.2 \text{ Gpc}^{-3} \text{ yr}^{-1}$  and  $\sim 3 \text{ Gpc}^{-3} \text{ yr}^{-1}$  in AGN disks. This channel is interesting due to potential electromagnetic counterparts in the form of X-rays or  $\gamma$ -rays, emitted due to super-Eddington accretion.

### 2.6.2 Caveats

As emphasized several times, the main takeaway from our estimated merger rate is that SNe kicks are a major deciding factor. The kick distribution we have chosen is a Maxwellian one. Even though NS kicks have been constrained, to some extent, from the motion of observed isolated pulsars (though it is not clear how this generalizes to natal kicks in multiple-star systems), BH kicks are still poorly constrained. Assuming different distributions can hence significantly affect merger rates, and the values of  $e_{\text{LIGO}}$  and  $\chi_{\text{eff}}$ .

Another caveat is that we looked at quadruple-star systems in the field, where stellar encounters are typically weak and infrequent. The evolution of quadruples in high-density environments, such as star clusters or galactic nuclei, will ostensibly be more dependent on fly-bys. For example, in the cores of globular clusters, binary-binary scatterings (e.g., [Mikkola, 1983](#); [Sigurdsson & Hernquist, 1993](#)) can dynamically form triple systems, with one of the stars escaping. Meanwhile, stable triples in clusters are much more likely to be destroyed by strong interactions. Similarly, quadruples can be dynamically formed by scattering processes (e.g., [van den Berk et al., 2007](#)) and can be destroyed by strong encounters. [Antognini & Thompson \(2016\)](#) performed scattering experiments of binary-binary, triple-single and triple-binary interactions to quantify and characterize the formation of triples in clusters. [Antonini et al. \(2016\)](#) studied dynamically formed triple systems in globular clusters using Monte Carlo models for the cluster coupled with an  $n$ -body integrator. They found that the timescales for angular momentum change can become comparable to the orbital periods, thereby making the secular approximation inaccurate. They also found eccentric LIGO band mergers. [Martinez et al. \(2020\)](#) performed a similar study and derived conservative BH-BH merger rates of  $\sim 0.35 \text{ Gpc}^{-3} \text{ yr}^{-1}$ . However, a study on quadruples in clusters is yet to be carried out and is beyond the scope of this paper.

We also looked at the effect of the CE mass-loss timescale  $t_{\text{CE}}$  and concluded that it does not affect merger rates meaningfully. Other studies ([Dominik et al., 2012](#); [Broekgaarden et al., 2021](#); [Fragione et al., 2021](#)) have shown that the CE efficiency parameter  $\alpha_{\text{CE}}$  has a more significant effect. Moreover, CE evolution still faces significant uncertainties.

The main question this work has tried to address is the contribution of secular evolution to compact object mergers in quadruple-star systems. In Section 2.5.4, we described the different scenarios of mergers and concluded that secular evolution indeed has an effect,

although perhaps not as significant as could be expected based on secular dynamics alone. However, our classification does not represent systems that undergo pre-compact object phase stellar collisions or have dynamical instabilities. Here, we briefly mention a few other examples from our population synthesis, leading to compact object mergers, not shown in Section 2.3:

- In 2+2 quadruples, the two inner binaries can be close enough that they merge in their main-sequence (MS) or giant phases. Alternatively, eccentricity enhancements cause them to merge prematurely. Now, we have a binary system of merger products, typically very massive stars, which can evolve into BHs and merge. There can also be systems in which there is only one inner binary merger in the pre-compact object phase. The resulting system evolves as a triple-star system.
- In 3+1 quadruples, the intermediate orbit’s eccentricity can be enhanced to an extent that the resulting configuration becomes dynamically unstable. One of two things can happen – either there is a collision, or one of the stars gets ejected from the system, resulting in a triple hierarchy. This triple system can now evolve and produce a merger.

Such examples show the wide complexity in the evolution of quadruples, and also explain why second-generation compact object mergers (see Fragione et al., 2020; Hamers et al., 2021b for examples) are rare. In fact, in our simulations, none of such mergers have been observed, not even in the zero SNe kicks case. Nevertheless, we can expect to see a few if the number of systems run was significantly higher. For a second-generation merger to occur, we need to have at least three compact objects in a bound stable configuration, which in itself never happens in our non-zero SNe kick models. Then, the first merger should occur, either due to interaction with the tertiary or due to a prior CE evolution and GW emission-aided orbit shrinkage. Now, the two resulting compact objects are far enough that they will not merge within a Hubble time, and there is no companion to enhance the merger.

The possibility of having four bound compact objects is even more scarce than having three of them. Even then, the orbit alignments and separations need to be just right to have a second-generation merger within a Hubble time. Thus, quadruple systems probably cannot explain recent GW detections of higher mass BH ( $\gtrsim 40 M_{\odot}$ ) mergers.

## 2.7 Conclusion

We used the population synthesis code MSE (Hamers et al., 2021a) to look for black hole (BH) and neutron star (NS) mergers in quadruple-star systems, from their birth as main-sequence (MS) stars to their death as compact objects, taking into account a wide range of physical processes. We looked at the two configurations of quadruples – 2+2 and 3+1 – and compared the 2+2 quadruples with ‘isolated’ binaries. We also compared seven different models (with altered parameters) for each of the configurations. Our main conclusions are listed below:

1. Quadruple-star systems contribute to a significant fraction of BH-BH mergers, with their merger rates being on the order of the LIGO rate. BH-NS mergers also do occur in quadruples, but not as many as LIGO rates predict. On the other hand, NS-NS merger rates are extremely low due to SNe kicks in these systems. The measured rates for our fiducial model (includes both types of quadruples) are  $13.7 \text{ Gpc}^{-3} \text{ yr}^{-1}$ ,  $7.1 \text{ Gpc}^{-3} \text{ yr}^{-1}$ , and  $1.3 \text{ Gpc}^{-3} \text{ yr}^{-1}$  respectively for BH-BH, BH-NS, and NS-NS mergers.
2. 2+2 quadruples have similar merger numbers to the isolated binaries, although the latter have higher merger numbers in all models except our model with zero SNe kicks. This indicates that, although the effects of secular evolution are seen in (15–30) % of systems, they can either aid or hinder compact object mergers.
3. Only in  $\sim (3\text{--}10)$  % of cases (when SNe kicks are excluded) is a compact object merger not associated with CE evolution, and a compact object multiple system forms successfully. In such cases, the mergers are due to dynamically induced high eccentricities.
4. A comparison of the two types of quadruples 2+2 and 3+1 shows that the former has many more BH-BH and BH-NS than the latter (by a factor of 3–4). The NS-NS merger rates are comparable (with SNe kicks).
5. SNe kicks are the most important factor for determining merger rates. Excluding kicks increases the number of mergers by factors of  $\sim 2\text{--}40$  for 2+2 quadruples, and  $\sim 5\text{--}8$  for 3+1 quadruples. The large outlier (factor  $\sim 40$  increase) is the NS-NS merger rate in 2+2 quadruples. The increase in BH-BH and BH-NS mergers is more significant in 3+1 quadruples, however.
6. Metallicity  $Z$  is another parameter that significantly affects the merger numbers, similar to isolated binaries. For  $Z = 0.1 Z_{\odot}$ , merger numbers are scaled up by factors of  $\sim 2\text{--}4$ . For  $Z = 0.01 Z_{\odot}$ , they are scaled up by factors of  $\sim 3\text{--}10$ . The greatest increase is seen in BH-NS mergers ( $\sim 3\text{--}4$  and  $\sim 6\text{--}10$  for the two metallicities respectively) for both types of quadruples, but more drastically in the 3+1 quadruples.
7. For quadruples, the LIGO band ( $f_{\text{GW}} \sim 10 \text{ Hz}$ ) eccentricities  $e_{\text{LIGO}}$  lie in the range  $10^{-3.5}$  to  $10^{-2.5}$  in all the models where supernova (SNe) kicks are included. In the latter case,  $e_{\text{LIGO}}$  can be high, even up to 0.3 (for both 2+2 and 3+1 systems). This can be attributed to secular evolution in the compact object phase.
8. Effective spin parameters  $\chi_{\text{eff}}$  of the compact object mergers, for quadruples, mostly lie in the range 0–1 in all the models where supernova (SNe) kicks are included. In the latter case, a significant fraction of systems have negative  $\chi_{\text{eff}}$ . Similarly to  $e_{\text{LIGO}}$ , the outliers, with negative  $\chi_{\text{eff}}$ , can be explained by secular evolution.
9. BH masses pre-merger can go up to  $\sim 17 M_{\odot}$  for Solar metallicity systems. Lower metallicities can produce even higher masses, up to  $\sim 27 M_{\odot}$  for  $Z = 0.01 Z_{\odot}$ . We

find no second-generation mergers, which could be due to their low formation rate and the limited number of systems considered here.

10. Excluding fly-bys decreases the number of BH-BH mergers by a factor of  $\sim 0.7$  for both types of quadruples. However, this decrease is not seen for BH-NS and NS-NS mergers. In the case of binaries, there is a noticeable decrease in all three types of mergers.
11. The common envelope mass-loss timescale  $t_{\text{CE}}$  does not alter merger rates much. Scaling or descaling  $t_{\text{CE}}$  by a factor of 10 does not change merger numbers beyond the Poisson error deviation. This can be understood by noting that isolated binary evolution (in particular, CE evolution) is the dominant factor in driving compact object mergers in quadruples. Therefore, whether or not outer orbits in the multiple system remain bound after a CE event is not very important, since secular evolution on its own only drives a small fraction of compact object mergers.

# Chapter 3

## Dynamical stability of triple-star systems

This chapter reproduces the paper [Vynatheya et al. \(2022\)](#), titled “*Algebraic and machine learning approach to hierarchical triple-star stability*”, and published in the journal MNRAS. The initial setup, code runs, and final analysis were all conducted by me. The text has been written mainly by me, with contributions from Adrian Hamers, Rosemary Mardling and Earl Bellinger.

### 3.1 Introduction

The three-body problem has been of interest to physicists ever since classical mechanics was formulated. Unlike the two-body problem, the equations governing the motion of three bodies do not admit general closed-form solutions; the fact that solutions exist that exhibit extreme sensitivity to initial conditions is evidence that this must be true. There are a few specific cases, including the test particle limit or the ‘restricted’ three-body problem, for which closed-form analytic solutions exist, but the general problem can be chaotic and can only be solved numerically. In the past few decades, the advent of computing has vastly improved our knowledge of  $N$ -body dynamics.

In this paper, we shall focus on hierarchical triple-star systems. Such a hierarchical configuration can be regarded as two ‘nested’ binaries, with an inner binary of two stars being orbited by a third companion. Unlike isolated binaries, the orbits of a triple can change over periods much greater than orbital timescales, and significantly, depending on the system. This secular evolution in triples leads to, in the lowest-order approximation, von Zeipel-Lidov-Kozai (LK or ZLK) oscillations ([von Zeipel, 1910](#); [Lidov, 1962](#); [Kozai, 1962](#); see [Naoz, 2016](#) for a review), which are periodic changes seen in the inner orbital eccentricity and the mutual orbital inclination. Drastic changes in eccentricity can lead to stellar collisions if the orbital periastron is on the order of stellar size and the LK oscillations are not quenched by general relativistic or tidal effects. Additionally, a large eccentricity can mark the onset of dynamical instability and the subsequent escape of one of the stars.

The physical origin of chaotic behaviour in hierarchical triples involves resonant interactions between the inner orbit and harmonics of the outer orbit (Mardling, 2008, 2013). In particular, significant energy exchange between the orbits must take place for one of the stars to escape, and this can only occur if there is enough power in the harmonic whose frequency is close to the inner orbital frequency. This in turn requires sufficiently high outer eccentricity. As a result, for a particular integer  $N \simeq P_{\text{out}}/P_{\text{in}}$ , it is the  $N : 1$  ‘resonance’ and its neighbours which determine stability in triple star systems, with the *resonance overlap stability criterion* from Chirikov (1979) providing a powerful heuristic for assessing this (Mardling, 2008). Resonance is at the heart of the simpler Mardling & Aarseth (2001) stability criterion (see Equation 3.2 below), which is based on the proposal that the ratio of outer to inner semimajor axes is proportional to some power of the ratio of the time of outer periastron passage to the inner orbital period.

Investigating the stability of hierarchical triples is important because of their abundance in the universe. Moe & Di Stefano (2017) found that  $\gtrsim 50\%$  of massive O- and B-stars reside in multiple-star systems like triples and quadruples, compared to  $\lesssim 10\%$  of solar-mass stars. Hence, the study of massive stars, which includes high-energy phenomena like supernovae and gravitational waves, is incomplete without first understanding the dynamical evolution of triples. However, direct  $N$ -body integration is computationally expensive and not always desirable. This makes it necessary to come up with techniques to predict the long-term stability of hierarchical configurations.

Besides being compelling from a pure dynamics perspective, the question of hierarchical triple-star stability is of interest in triple population synthesis studies (e.g., Antonini et al., 2016; Fragione & Loeb, 2019). In this context, dynamical stability criteria are an important step in the initial sampling of a population of triple-star systems. A poor classification can impact the statistics of the problem.

In this work, we compare our results to the stability criteria presented by Eggleton & Kiseleva (1995) and Mardling & Aarseth (2001). Eggleton & Kiseleva (1995) proposed an empirical fit for the stability of hierarchical triple-star systems. They assumed a system to be stable if it remains in the same hierarchical configuration after 100 orbits of the ‘outer’ binary. A more widely used stability criterion was provided by Mardling & Aarseth (2001) (see also Mardling & Aarseth, 1999). They drew parallels between dynamical instability in triples and tidal evolution and presented a semi-analytical formula to distinguish between stable and unstable systems.

The structure of this paper is as follows. Section 3.2 briefly describes the  $N$ -body code we used and the assumptions we make about stability; Section 3.3 details the initial conditions and our parameter space; Sections 3.4 and 3.5 form the crucial components of this paper, describing our updated stability criterion and our machine learning classifier respectively; Section 3.6 summarises our results; Section 3.7 is the discussion; and Section 3.8 finally concludes.

## 3.2 *N*-body code and stability

For our study of hierarchical triple-star systems, we use the *N*-body code **MSTAR** (see [Rantala et al., 2020](#) for details), which performs highly accurate integration for a wide range of mass ratios. For simplicity, we use the code with the post-Newtonian (PN) terms disabled. The PN terms have little effect when distances are in the order of  $\sim 1$  AU and for stellar-mass scales but can be significant during close encounters and compact object mergers. The reason for ignoring PN terms is to make our problem *scale-free* in mass, distance and time. Thus, we do not need to be concerned about the actual values of masses and distances and instead, concentrate on ratios of quantities.

With the scale-free assumption, hierarchical triple systems have the following relevant initial parameters, which dictate the evolution of the system:

- Inner mass ratio  $q_{\text{in}} = m_2/m_1 \leq 1$  ( $m_2 \leq m_1$ ), where  $m_1$  and  $m_2$  are the inner binary masses of the hierarchical triple.
- Outer mass ratio  $q_{\text{out}} = m_3/(m_1 + m_2)$ , where  $m_3$  is the outer mass of the hierarchical triple.
- Semimajor axis ratio  $\alpha = a_{\text{in}}/a_{\text{out}} < 1$ , where  $a_{\text{in}}$  and  $a_{\text{out}}$  are the semimajor axes of the inner and outer orbits of the hierarchical triple respectively.
- Inner orbit eccentricity  $0 \leq e_{\text{in}} < 1$ .
- Outer orbit eccentricity  $0 \leq e_{\text{out}} < 1$ .
- Mutual inclination  $i_{\text{mut}}$  between the two orbits of the hierarchical triple.

Here, the mutual inclination  $\cos(i_{\text{mut}}) = \cos(i_{\text{in}})\cos(i_{\text{out}}) + \sin(i_{\text{in}})\sin(i_{\text{out}})\cos(\Omega_{\text{in}} - \Omega_{\text{out}})$  takes into account two of the three orbit-orientation (Euler) angles, with the inclination  $i$  and the longitude of ascending node  $\Omega$  being defined with respect to a chosen reference direction (the subscripts refer to the inner and outer orbits). In fact, as demonstrated in panels (e) and (f) of Figure 3.16 of [Mardling \(2008\)](#), the stability boundary is also sensitive to the third Euler angle, the argument of periapsis  $\omega$ , since it is this which determines the position of a system relative to the centre of the relevant  $N : 1$  resonance, and as a consequence, the system's stability. We do not attempt to capture the resulting step-like structure of the stability boundary, instead adopting an expression which effectively smooths this behaviour. Similarly, any dependence on the true anomaly  $\theta$  is not captured in this work.

We now come to the defining criterion for the stability of a triple. Newtonian mechanics predicts that a bound two-body system remains in a closed elliptical orbit indefinitely. On the other hand, the evolution of a three-body system can be, in general, chaotic and unpredictable. In many cases, minute changes in the initial parameters can manifest as substantial differences in evolution in secular timescales. Thus, we need to decide about how to quantify stability. We deem a triple system stable if it remains bound for 100 outer

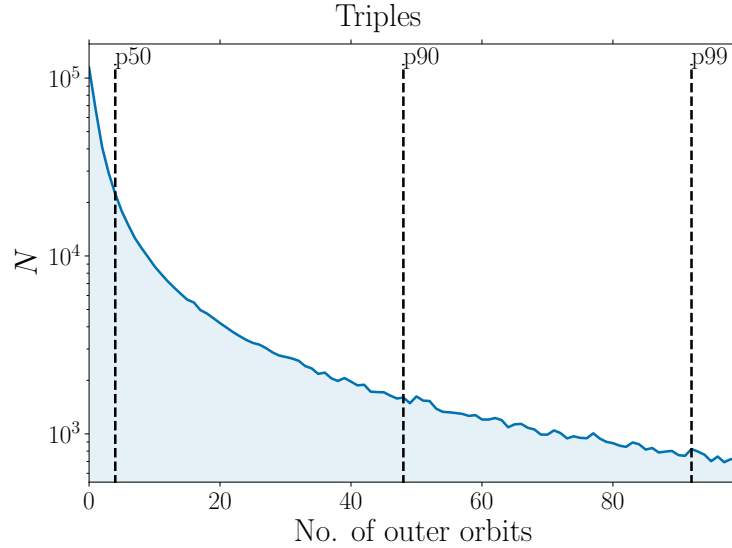


Figure 3.1: Plot of the number of outer orbits within which unstable triple-star systems become unbound. The dashed lines represent the 50th, the 90th and the 99th percentile values, which shows that the fraction of unstable systems that become unbound within 100 outer orbits decreases rapidly.

orbits and if the semimajor axes of both inner and outer orbits do not change by more than 10% of the initial value. The rationale for choosing 100 orbits is shown in Figure 3.1. The most unstable systems become unbound well before 100 outer orbits. There exist a small fraction of unstable systems which remain bound after 100 outer orbits, and the second criterion applies to these systems. The 10% threshold for semimajor axis change ensures that triple systems on the verge of becoming unstable are not erroneously classified as stable.

### 3.3 Data set and initial conditions

We generate initial conditions for hierarchical triple systems such that the parameter space is filled more or less uniformly. This is necessary to ensure good classification.

Moreover, to analyse the parameter space more thoroughly, we look at different parameter space slices, where one or more initial parameters are kept constant while others are varied. We perform three kinds of parameter space slices:

1. Varied semimajor axes and masses, constant eccentricities and mutual inclinations (see Table 3.1).
2. Varied semimajor axes and eccentricities, constant masses and mutual inclinations (see Table 3.2).



Slice	$e_{\text{in}}$	$e_{\text{out}}$	$i_{\text{mut}}$
Fiducial	0.0	0.0	0.0
$i_{\text{mut}} = \pi/2$	0.0	0.0	$\pi/2$
$i_{\text{mut}} = \pi$	0.0	0.0	$\pi$
$e_{\text{out}} = 0.3$	0.0	0.3	0
$e_{\text{out}} = 0.6$	0.0	0.6	0
$e_{\text{in}} = 0.3$	0.3	0.0	0
$e_{\text{in}} = 0.6$	0.6	0.0	0

Table 3.1: Parameter space slices where  $\alpha$ ,  $q_{\text{in}}$  and  $q_{\text{out}}$  are varied, and other parameters are kept constant. The columns in the table show the constant values of these parameters in different slices.

Slice	$q_{\text{in}}$	$q_{\text{out}}$	$i_{\text{mut}}$
Fiducial	1.0	0.5	0.0
$i_{\text{mut}} = \pi/2$	1.0	0.5	$\pi/2$
$i_{\text{mut}} = \pi$	1.0	0.5	$\pi$
$q = 0.1, 0.818$	0.1	0.818	0.0
$q = 1, 9$	1.0	9.0	0.0
$q = 0.8, 0.111$	0.8	0.111	0.0

Table 3.2: Parameter space slices where  $\alpha$ ,  $e_{\text{in}}$  and  $e_{\text{out}}$  are varied, and other parameters are kept constant. The columns in the table show the constant values of these parameters in different slices.

3. Varied semimajor axes and mutual inclinations, constant masses and eccentricities (see Table 3.3).

We also limit our parameter ranges to remain in the triple-star system domain:

- $10^{-2} \leq q_{\text{in}} \leq 1, 10^{-2} \leq q_{\text{out}} \leq 10^2$
- $10^{-4} < \alpha < 1$
- $0 \leq e_{\text{in}} < 1, 0 \leq e_{\text{out}} < 1$
- $0 \leq i_{\text{mut}} \leq \pi$ .

### 3.4 Updated formula

As mentioned previously, we attempt to improve on the previously existing and widely used stability criterion given by [Mardling & Aarseth \(2001\)](#). Before detailing our up-

Slice	$q_{\text{in}}$	$q_{\text{out}}$	$e_{\text{in}}$	$e_{\text{out}}$
Fiducial	1.0	0.5	0.0	0.0
$e_{\text{out}} = 0.3$	1.0	0.5	0.0	0.3
$e_{\text{out}} = 0.3$	1.0	0.5	0.0	0.6
$e_{\text{in}} = 0.3$	1.0	0.5	0.3	0.0
$e_{\text{in}} = 0.6$	1.0	0.5	0.6	0.0
$q = 0.1, 0.818$	0.1	0.818	0.0	0.0
$q = 1, 9$	1.0	9.0	0.0	0.0
$q = 0.8, 0.111$	0.8	0.111	0.0	0.0

Table 3.3: Parameter space slices where  $\alpha$  and  $i_{\text{mut}}$  are varied, and other parameters are kept constant. The columns in the table show the constant values of these parameters in different slices.

dated stability criterion, we mention the two stability criteria with which we compare our classification performances.

- Defining  $Y = [a_{\text{out}}(1 - e_{\text{out}})]/[a_{\text{in}}(1 + e_{\text{in}})]$  [Eggleton & Kiseleva \(1995\)](#) (henceforth EK95) derived the following fitting formula for stability:

$$Y_{\text{crit}} = 1 + \frac{3.7}{q_{\text{out}}^{-1/3}} - \frac{2.2}{1 + q_{\text{out}}^{-1/3}} + \frac{1.4}{q_{\text{in}}^{-1/3}} \frac{q_{\text{out}}^{-1/3} - 1}{q_{\text{out}}^{-1/3} + 1}. \quad (3.1)$$

A hierarchical triple-star system is deemed ‘stable’ if  $Y > Y_{\text{crit}}$  and ‘unstable’ if  $Y < Y_{\text{crit}}$ .

- The other criterion we will compare against is the semi-analytical, and more accurate, formula by [Mardling & Aarseth \(2001\)](#) (henceforth MA01):

$$\frac{R_{\text{p,crit}}}{a_{\text{in}}} = 2.8 \left[ (1 + q_{\text{out}}) \frac{1 + e_{\text{out}}}{(1 - e_{\text{out}})^{1/2}} \right]^{2/5} \left( 1 - \frac{0.3i_{\text{mut}}}{\pi} \right) \quad (3.2)$$

Here,  $R_{\text{p}} = a_{\text{out}}(1 - e_{\text{out}})$  is the outer periastron distance and a triple system is deemed ‘stable’ if  $R_{\text{p}} > R_{\text{p,crit}}$  and ‘unstable’ otherwise.

Finally, we present our stability criterion. After taking into account the dependencies on the initial parameters, we defined a new parameter  $\tilde{e}_{\text{in}}$  as follows:

$$\begin{aligned} e_{\text{in,max}} &= \sqrt{1 - \frac{5}{3} \cos^2 i_{\text{mut}}}; \\ e_{\text{in,avg}} &= 0.5e_{\text{in,max}}^2; \\ \tilde{e}_{\text{in}} &= \max(e_{\text{in}}, e_{\text{in,avg}}). \end{aligned} \quad (3.3)$$

The first equation is the quadrupole-order approximation for the maximum value of inner eccentricity due to LK oscillations. The second equation describes the *average* eccentricity during an orbit in the sense that the *time-averaged* separation for a single orbit is  $\langle r_{\text{in}} \rangle = a_{\text{in}}(1 + e_{\text{in,avg}})$  (see [Stein & Elsner, 1977](#)).

Our updated stability criterion is as follows:

$$\begin{aligned} \tilde{Y}_{\text{crit}} = 2.4 & \left[ \frac{(1 + q_{\text{out}})}{(1 + \tilde{e}_{\text{in}})(1 - e_{\text{out}})^{1/2}} \right]^{2/5} \\ & \times \left[ \left( \frac{1 - 0.2\tilde{e}_{\text{in}} + e_{\text{out}}}{8} \right) (\cos i_{\text{mut}} - 1) + 1 \right]. \end{aligned} \quad (3.4)$$

Here,  $\tilde{Y}$  is the same as  $Y$  with  $e_{\text{in}}$  replaced by  $\tilde{e}_{\text{in}}$ . The second term in the equation accounts for some of the complicated dependence on mutual inclination, whereas the first term is very similar to the MA01 formula with an additional  $\tilde{e}_{\text{in}}$  dependence.

The reasoning behind the choices for the dependencies in Equation 3.4 is detailed in the following sub-sections.

### 3.4.1 Eccentricity dependence

From our parameter space slices of eccentricities, we found that an additional dependence on  $e_{\text{in}}$  can better describe the classification boundary between stable and unstable systems. This is unlike the MA01 formula, which has no dependence on  $e_{\text{in}}$ .

Figures 3.2 and 3.3 illustrate the dependence of stability on both  $e_{\text{in}}$  and  $e_{\text{out}}$ . The dependence of  $Y_{\text{crit}}$  on  $e_{\text{out}}$  is the same as the MA01 factor  $(1 - e_{\text{out}})^{-2/5}$ , while the extra dependence on  $e_{\text{in}}$  is taken into consideration in Equation 3.4 through the factor  $(1 + e_{\text{in}})^{-2/5}$ . It should also be noted that Equation 3.4 works better for prograde orbits (Figure 3.2) than for retrograde orbits (Figure 3.3). Retrograde systems tend to have a stronger dependence on  $e_{\text{in}}$  for stability than prograde systems. Nonetheless, it is a notable improvement on previously existing stability criteria.

### 3.4.2 Mutual inclination dependence

The parameter space slices of mutual inclinations showed that the inclination dependence on stability is not linear. The ad-hoc inclination factor in the MA01 formula,  $(1 - 0.3i_{\text{mut}}/\pi)$ , is a good linear approximation but leaves room for improvement. In particular, systems with mutually highly inclined orbits (around  $i_{\text{mut}} = \pi/2$ ) tend to be less stable than those with both less-inclined prograde and retrograde orbits. Moreover, retrograde orbits tend to be more stable than prograde orbits, which is also captured by the MA01 formula.

To account for the bowl-shaped depression in the stability classification boundary, we employed a trick used by [Grishin et al. \(2017\)](#). We replaced  $e_{\text{in}}$  by  $\tilde{e}_{\text{in}}$ , defined in Equation 3.3.

The motivation for doing this substitution is that the inner eccentricity, unlike the outer eccentricity, is not constant in the quadrupole-order approximation of LK oscillations. The

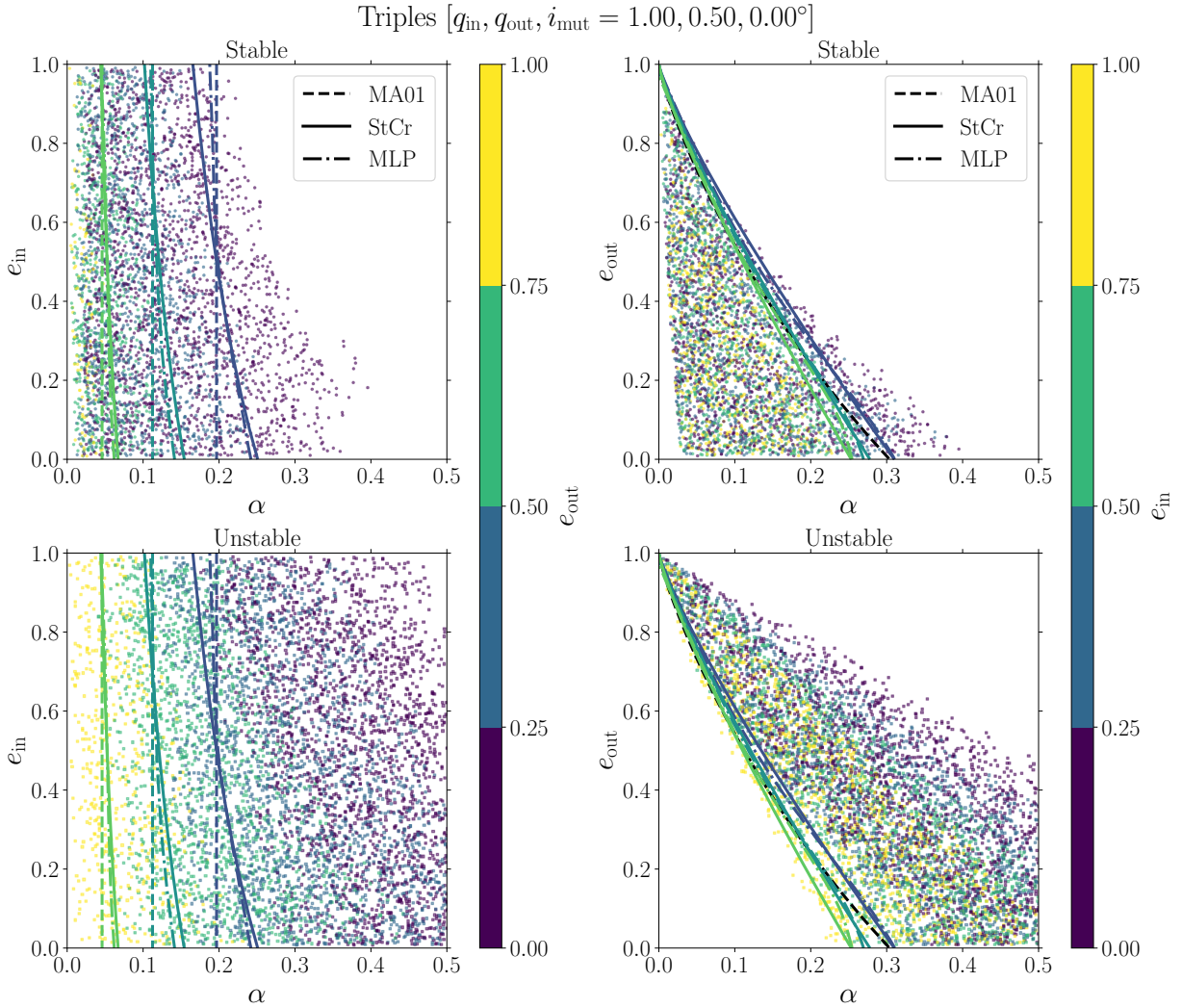


Figure 3.2: Plot showing a parameter space slice of varying  $\alpha$ ,  $e_{\text{in}}$  and  $e_{\text{out}}$ . The constant values of the other parameters are mentioned at the top. The left panel plots  $e_{\text{in}}$  vs  $\alpha$ , while the right panel plots  $e_{\text{out}}$  vs  $\alpha$ . The missing varied parameter is the colour axis in all panels. The top and bottom panels show the systems which remain stable and become unstable respectively from direct  $N$ -body simulations. The lines represent contours of the classification boundaries, with the legend labels ‘MA01’, ‘StCr’ and ‘MLP’ referring to the MA01 criterion, our updated stability criterion (Equation 3.4) and our MLP model respectively. The colours of the contour lines coincide with the transition values on the colour axes. The black lines are independent of the colour axis.

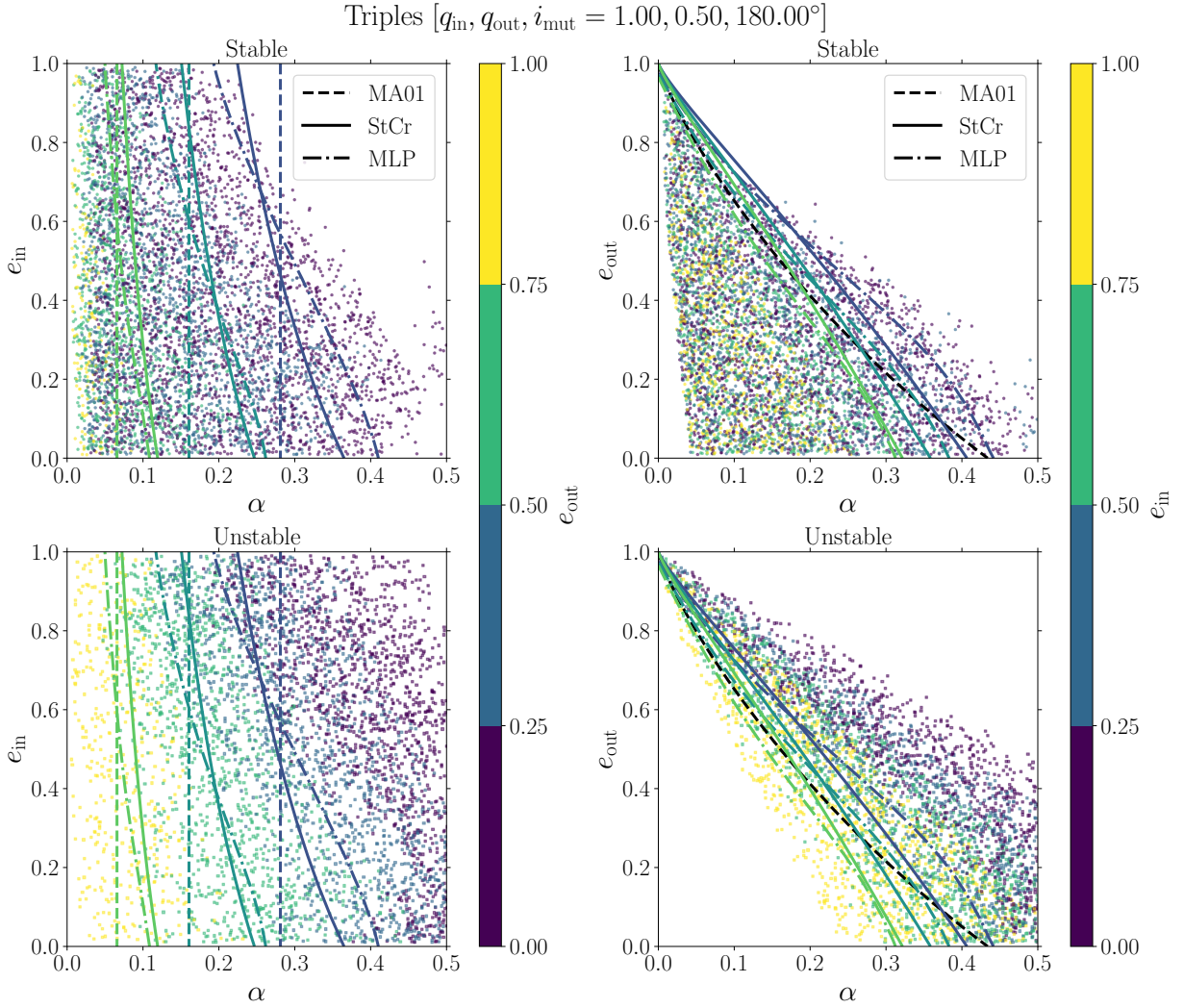


Figure 3.3: Plot similar to Figure 3.2, but showing a different parameter space slice. The changed constant values are mentioned at the top.

$e_{\text{in}}$  value changes the most for highly inclined orbits, and hence, replacing the initial value of  $e_{\text{in}}$  with a more average value can help to better characterise such systems.

Figures 3.4 and 3.5 represent the ‘bowl-shaped’ depressions of instability. Furthermore, the value of  $q_{\text{out}}$  also changes the inclination dependence. Equation 3.4 works best when  $q_{\text{out}}$  is high, i.e., the outer star’s mass is comparable or higher than the inner binary stars’ masses (Figure 3.4). On the other hand, when  $q_{\text{out}}$  is low, mid-range retrograde orbits may be wrongly classified near the stability boundary (Figure 3.5).

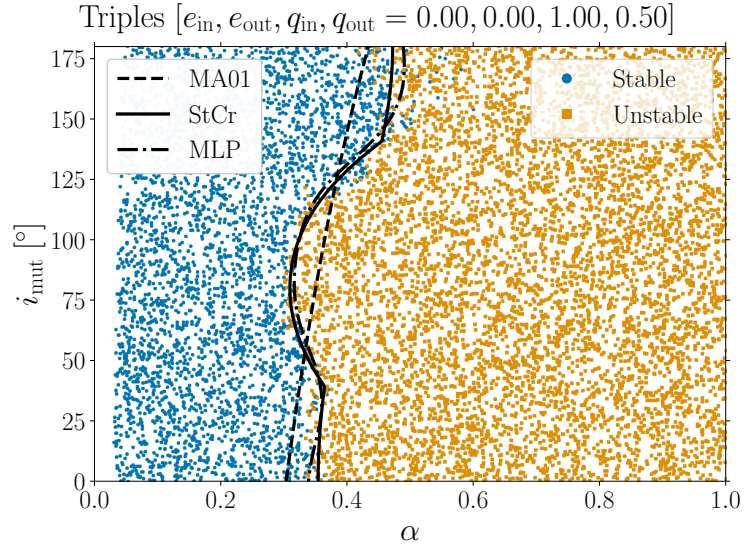


Figure 3.4: Plot showing a parameter space slice of varying  $\alpha$  and  $i_{\text{mut}}$ . The constant values of the other parameters are mentioned at the top. The left and right panels show the systems which remain stable and become unstable respectively from direct  $N$ -body simulations. The lines represent the classification boundaries, with the legend labels ‘MA01’, ‘StCr’ and ‘MLP’ referring to the MA01 criterion, our updated stability criterion (Equation 3.4) and our MLP model respectively.

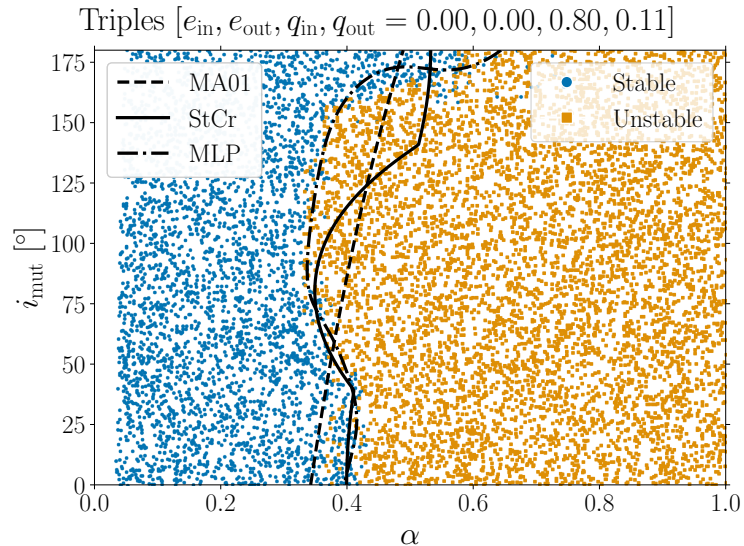


Figure 3.5: Plot similar to Figure 3.4, but shows a different parameter space slice. The changed constant values are mentioned at the top.

### 3.4.3 Mass ratio dependence

Note that, just like the MA01 formula, Equation 3.4 has the same  $q_{\text{out}}$  dependence factor  $(1 + q_{\text{out}})^{2/5}$  and no dependence on  $q_{\text{in}}$ . Our parameter space slices of mass ratios showed almost no dependence on  $q_{\text{in}}$  (except when mass ratios are very small,  $\lesssim 0.1$ ). If we were to replace the quadrupole-order approximated expression for  $e_{\text{in,max}}$  by the non-test particle limit formula presented by Hamers (2021), the slight dependence on  $q_{\text{in}}$  can be accounted for to some extent. However, we found that this replacement did not perform significantly better in classification whereas the expressions are significantly more complicated.

Figure 3.6 validates the above claims. The small dependence on  $q_{\text{in}}$  can be seen in both figures as a tail in the very-low mass ratio regime.

## 3.5 Machine learning approach

Machine learning (ML) classifiers are ubiquitous in the current era of computing. The basic premise of all ML algorithms is to learn from data to improve in classification or regression tasks. The results of such algorithms depend on the model parameters and hyper-parameters, which need to be tuned for reasonable performance.

### 3.5.1 Multi-layer perceptrons

An artificial neural network (ANN; McCulloch & Pitts, 1943; for a review, see Hastie et al. 2009) is a supervised ML algorithm, which uses connected units (neurons), arranged in a series of layers, to perform classification tasks. Each neuron receives inputs from other neurons from the previous layer and provides outputs to the neurons in the following layer. The connection strengths between neurons are controlled by weights. The output of a given neuron is the linear weighted sum of the inputs from the previous layer, which is then passed through an activation function  $\phi$  before being input to the next layer. Thus, the output of the  $j$ th neuron is given as:

$$y_j = \phi \left( \sum_{i=0}^n w_{ij} x_i + b_j \right) \quad (3.5)$$

Here,  $\mathbf{x}$  are the inputs from the neurons from the previous layer and  $n$  is the number of such neurons. The parameters  $\mathbf{w}$  and  $\mathbf{b}$  are optimised during training. The network does this by minimising a pre-defined loss function, which depends on the consensus between the true classification labels and the predicted labels.

We specifically implement the simplest form of an ANN called a multi-layer perceptron (MLP; Rosenblatt, 1958. MLPs are fully-connected ANNs, in the sense that every neuron in a given layer is connected to every neuron in the immediately adjacent layers. They consist of an input layer, one or more hidden layers and an output layer. Figure 3.7 shows a schematic of the MLP network we used for the classification of stable and unstable triple-star systems.

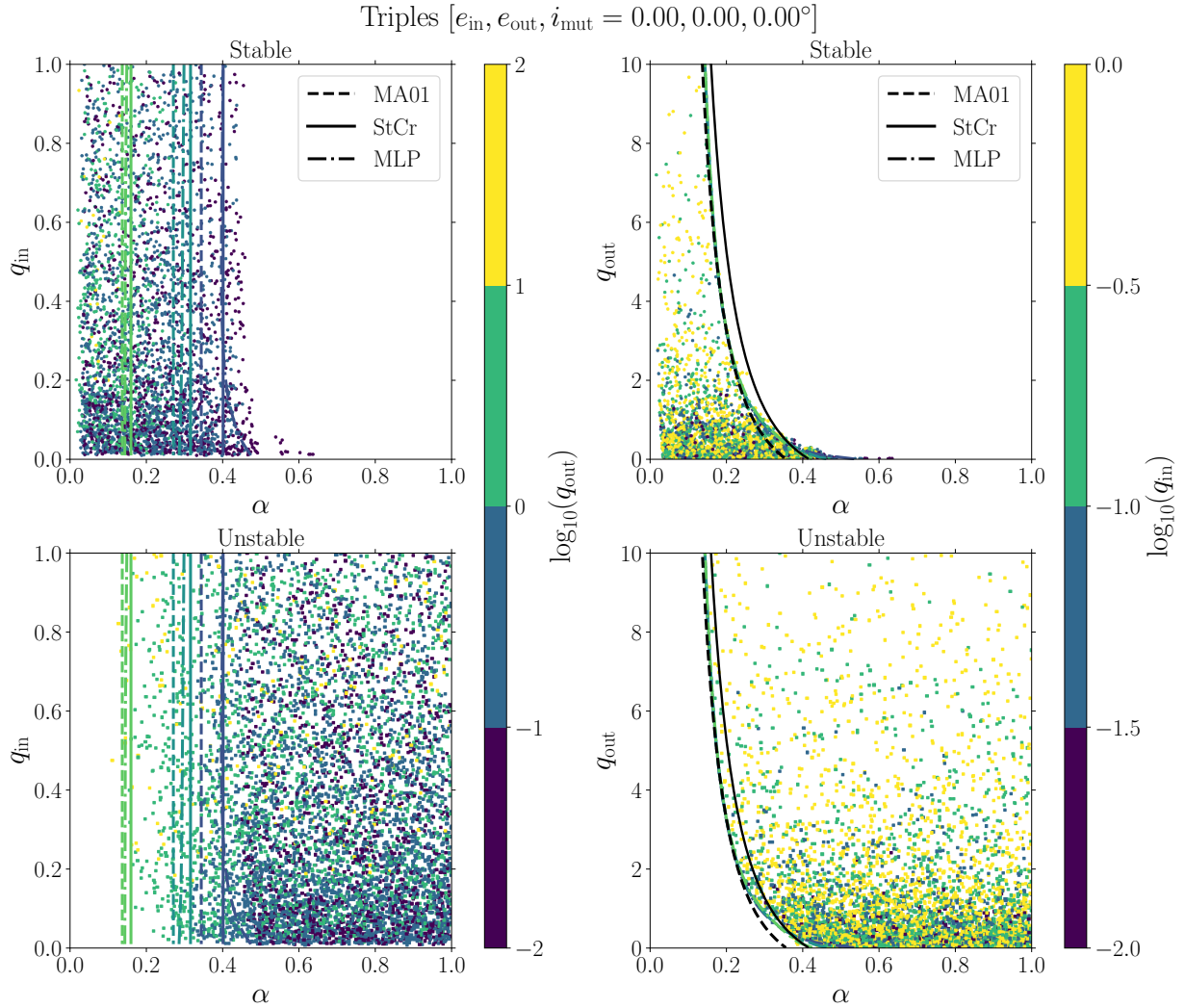


Figure 3.6: Plot showing a parameter space slice of varying  $\alpha$ ,  $q_{\text{in}}$  and  $q_{\text{out}}$ . The constant values of the other parameters are mentioned at the top. The left panel plots  $q_{\text{in}}$  vs  $\alpha$ , while the right panel plots  $q_{\text{out}}$  vs  $\alpha$ . The missing varied parameter is the colour axis in all panels. The top and bottom panels show the systems which remain stable and become unstable respectively from direct  $N$ -body simulations. The lines represent contours of the classification boundaries, with the legend labels ‘MA01’, ‘StCr’ and ‘MLP’ referring to the MA01 criterion, our updated stability criterion (Equation 3.4) and our MLP model respectively. The colours of the contour lines coincide with the transition values on the colour axes. The black lines are independent of the colour axis.



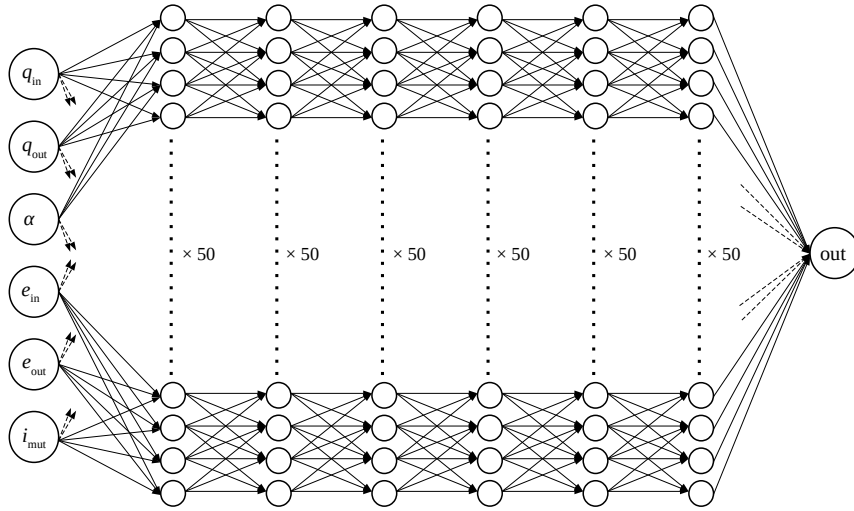


Figure 3.7: Schematic of the MLP architecture used for classification. Every neuron in a given layer is connected to every neuron in the adjacent layers. The input layer has 6 neurons ( $q_{in}$ ,  $q_{out}$ ,  $\alpha$ ,  $e_{in}$ ,  $e_{out}$ ,  $i_{mut}$ ), the output layer has one neuron (value ranges from 0 for ‘stable’ to 1 for ‘unstable’), and the six hidden layers have 50 neurons each.

For the MLP classifier, we use an implementation provided by the `scikit-learn` (Pedregosa et al., 2011) package in Python.

### 3.5.2 Training and testing data sets

We generated  $10^6$  hierarchical triple-star systems whose initial conditions were sampled uniformly throughout our parameter space, with the parameter limits mentioned in Section 3.3. Besides these six parameters, we also sample the arguments of periapsis and mean anomalies of both orbits uniformly. However, these values are not supplied to the MLP network as inputs. Since the data sparsely populated the six-dimensional space, we added a constraint to ensure that systems are sampled closer to the classification boundary. Additionally, we disregarded systems whose  $N$ -body integration took longer than five hours. These made up 0.4% of our total sample.

To do this, we consider the MA01 formula  $R_{p,ratio} = R_p/R_{p,crit}$  (Equation 3.2). If this ratio is greater than 1, a triple-star system is labelled ‘stable’, and vice-versa. However, since the formula does not have 100% accuracy, there is a range of values around 1 where systems can be classified incorrectly. We found that the range  $0.3 \leq R_{p,ratio} \leq 2.0$  is the most ambiguous for classification. Thus, after sampling our triple systems, we eliminated any system whose  $R_{p,ratio}$  value lies outside this range. This ensures that our training data, which lay within the range, is well suited for classification.

During classification, we use an 80:20 split of training and testing data. This, along with

5-fold cross-validation, was implemented to help validate the performance of the classifier.

### 3.5.3 Network architecture and hyper-parameters

We tried different network architectures and varied the hyper-parameters to arrive at the best-performing MLP model. The performance of a classifier refers to how well the model predicts the labels of previously unseen data – the test set. We chose our hyper-parameters by training a grid of MLP models, along with 5-fold cross-validation.

Our final model consists of 6 hidden layers of 50 neurons each (shown in Figure 3.7). Training a network of this size, with  $10^6$  training data points, takes about 30 minutes on 64 cores of an AMD EPYC 7742 CPU. The performance was found to be slightly worse with 4 or 5 hidden layers, and having 10 or 100 neurons in each layer worsened the classification substantially compared to having 50 neurons.

For optimisation, the network uses the *Adam solver* (Kingma & Ba, 2014), which is a stochastic gradient descent algorithm. Finally, we use the *logistic* activation function  $\phi(x) = 1/(1 + e^{-x})$  for the neuron outputs. Although slower in implementation than the widely used *ReLU* (rectified linear unit) activation function  $\phi(x) = \max(0, x)$ , the logistic function performs slightly better.

Other hyper-parameters include:

- Batch size, which is the size of the mini-batches used for stochastic gradient descent. After experimenting with batch sizes of 200, 1000 and 5000, we chose 1000.
- L2 regularisation term, which is an additional term in the loss function that penalises the squares of the weights. If this penalty is too low, there is an increased risk of over-fitting, and vice-versa. After experimenting with values of  $10^{-2}$ ,  $10^{-3}$  and  $10^{-4}$ , we chose  $10^{-3}$ .
- Initial learning rate, which controls the step-size of updating the weights and biases after each iteration. If it is too low, the optimiser takes a very long time to converge to the minimum of the loss function; if it is too high, the minimum can be skipped. After experimenting with values of  $10^{-2}$ ,  $10^{-3}$  and  $10^{-4}$ , we chose  $10^{-2}$ .

## 3.6 Results and comparison

To quantify the effectiveness of any classification algorithm, we need to consider a few quantities. Some of these include:

- Overall score: The fraction of systems which are classified correctly i.e., the ‘stable’ and ‘unstable’ systems are indeed stable and unstable respectively from direct  $N$ -body simulations.
- False stable ( $FS$ ) systems: The number of truly unstable (from  $N$ -body simulations) systems that the model predicts as ‘stable’. Similarly, we can define true stable ( $TS$ ) systems.

Classifier	Score	$P_{\text{stable}}$	$P_{\text{unstable}}$	$R_{\text{stable}}$	$R_{\text{unstable}}$
EK95	0.86	0.96	0.81	0.68	0.98
MA01	0.90	0.92	0.90	0.81	0.96
StCr	0.93	0.93	0.92	0.85	0.96
MLP	0.95	0.93	0.96	0.92	0.96

Table 3.4: Overall scores, precisions  $P$  and recalls  $R$  for the different classifiers we compare with. The labels ‘StCr’ and ‘MLP’ refer to our updated stability criterion (Equation 3.4) and our MLP model respectively.

- False unstable ( $FU$ ) systems: The number of truly stable (from  $N$ -body simulations) systems that the model predicts as ‘unstable’. Similarly, we can define true unstable ( $TU$ ) systems.
- Precision: The ratio of correctly classified stable (unstable) systems to the total number of systems classified as ‘stable’ (‘unstable’):  $P_{\text{stable}} = TS/(TS + FS)$  and  $P_{\text{unstable}} = TU/(TU + FU)$ . It quantifies validity of the classification.
- Recall: The ratio of correctly classified stable (unstable) systems to the total number of truly stable (unstable) systems:  $R_{\text{stable}} = TS/(TS + FU)$  and  $R_{\text{unstable}} = TU/(TU + FS)$ . It quantifies completeness of the classification.

Table 3.4 shows the comparison of scores, precisions and recalls of EK95, MA01, our updated Equation 3.4 and our MLP model from Section 3.5. It is evident that both our methods score better than the previous studies, and that the MLP model performs the best in classification. It is important to note that these scores can vary depending on the range of sampled parameter space. In our case, we sampled ‘close’ to the MA01 classification boundary line as described in Section 3.5.

We also show the false stable and unstable rates for the three parameter space slices (see Section 3.3) in Figures 3.8, 3.9 and 3.10 respectively. Again, both our methods perform better than EK95 and MA01 in all parameter space slices, with the MLP model being better in most cases. The figures indicate that the parameter space slices of retrograde orbits ( $i_{\text{mut}} = \pi$ ) have the highest misclassification rates. High  $e_{\text{in}}$  values can also lead to less efficient classification. On the other hand, parameter space slices with high  $q_{\text{out}}$  seem to have the best classification rates.

## 3.7 Discussion

We reiterate that our defining criterion for stability (see Section 3.2) is not absolute and that the accuracy of our classification would vary if we were to employ a different defining criterion. Moreover, our integration time of 100 outer orbits does not fully capture the instability of those systems that become unbound much later on. For example, [Mardling](#)

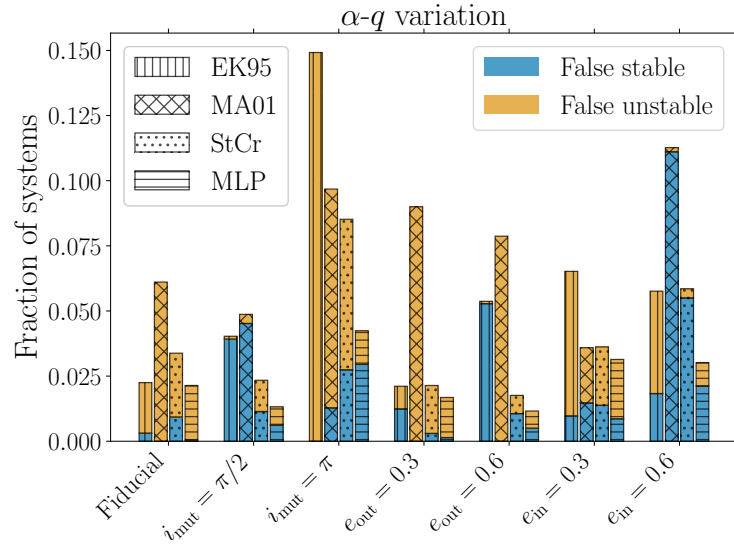


Figure 3.8: Bar chart illustrating the total fraction of ‘false stable’ and ‘false unstable’ systems (defined in text) in the parameter space slice of varying  $\alpha$ ,  $q_{\text{in}}$  and  $q_{\text{out}}$ . The  $x$ -axis labels refer to the constant values described in Table 3.1. The legend labels ‘StCr’ and ‘MLP’ refer to our updated stability criterion (Equation 3.4) and our MLP model respectively.

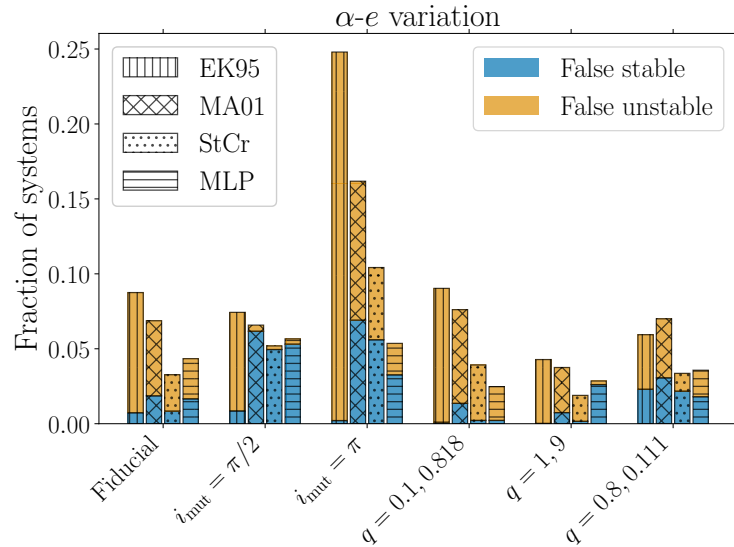


Figure 3.9: Plot similar to Figure 3.8, but in the parameter space slice of varying  $\alpha$ ,  $e_{\text{in}}$  and  $e_{\text{out}}$ .

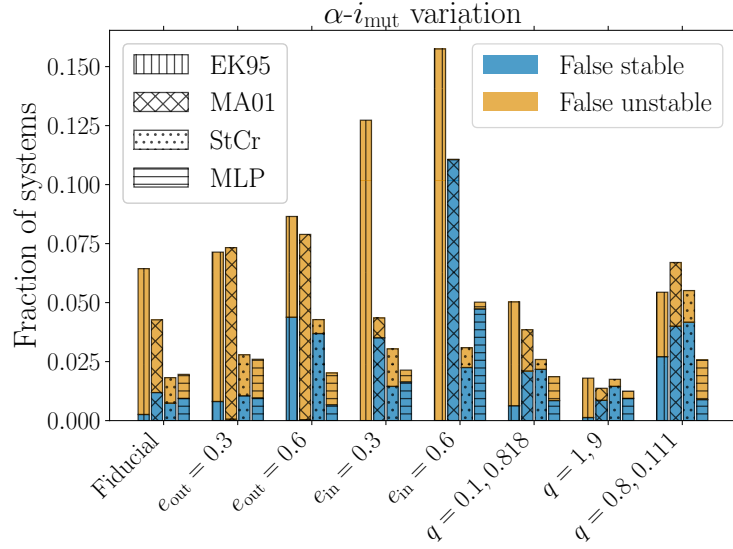


Figure 3.10: Plot similar to Figure 3.8, but in the parameter space slice of varying  $\alpha$  and  $i_{\text{mut}}$ .

(2008) demonstrated that the trajectory of a triple close to the stability boundary can diverge from another almost identical triple with slightly different initial conditions even after 100 outer orbits (see Figure 3.7). Our additional criterion that the inner and outer semimajor axes must not change more than 10% accounts for some of these unstable systems, but not all. This assumption is reasonable since hierarchical triples that become unstable undergo non-periodic, i.e., persistent transfer of energy between the inner and outer orbits. Since the semimajor axes are inversely proportional to the energies of the respective orbits, any significant change in their values would indicate that the triple is on the verge of becoming unbound.


It is worth noting that, very recently, [Lalande & Trani \(2022\)](#) also presented a machine learning approach to determine the stability of hierarchical triples. They employ a convolutional neural network (CNN), with a time series of orbital parameters as the training data, to perform the classification. This is unlike our classification which depends only on the *initial* values of the parameters, which makes our MLP model simpler and faster to use. They also assume equal masses, whereas we consider the dependence on mass ratios in our analysis. Finally, we highlight that an algebraic criterion like Equation 3.4 can be more useful than an ML classifier in understanding the physical dependencies on the initial parameters.

Stability criteria have also been used to classify hierarchical quadruple-star systems. Many studies, including [Hamers et al. \(2021b\)](#) and [Vynatheya & Hamers \(2022\)](#), applied the MA01 criterion to quadruples by considering them as two ‘approximate’ triple systems. For example, in a 2+2 quadruple system, one of the two inner binaries can be approximated as a single-star companion to the other inner binary. Hence, applying the triple stability criterion twice (one with each inner binary) yields an effective quadruple-star stability

criterion. A similar procedure can be applied on a 3+1 quadruple by approximating the innermost binary as a single star and plugging in the triple stability criterion to the two ‘nested’ triples. Nevertheless, as shown by our preliminary findings, this process does not always predict the stability of the quadruple accurately, especially in cases where the mutual inclinations of the orbits are significant. To overcome this, we are working on a quadruple stability criterion as well (Vynatheya et al. *in prep*) to analyse this problem in greater detail.

### 3.8 Conclusion

We presented an algebraic criterion to classify hierarchical triple-star systems based on their dynamical stability. This formula is an improved version of the widely used stability criterion of Mardling & Aarseth (2001) (MA01). We also performed the same classification using a fully connected neural network - a multilayer perceptron (MLP). Our labelled training data of  $10^6$  triples are generated by direct  $N$ -body simulations of triple-star systems using the  $N$ -body code MSTAR (Rantala et al., 2020). The main summary and results of the paper are presented in the following points:

- Our updated formula, Equation 3.4, adds a dependence on inner orbital eccentricity  $e_{\text{in}}$  which is absent in the MA01 formula. It also has a more complicated dependence on mutual orbital inclination  $i_{\text{mut}}$ , an improvement over the inclination dependence of MA01 described by an ad-hoc inclination factor.
- Similar to the MA01 criterion, Equation 3.4 does not have an explicit dependence on inner mass ratio  $q_{\text{in}}$ . This is mostly justified, the only exception being the regime where both inner and outer mass ratios are very low ( $\lesssim 0.1$ ).
- Equation 3.4 performs better than MA01 in all parameter space slices considered and has an overall classification score of 93%. The precisions of stable and unstable systems are 93% and 92% respectively, while the recalls are 85% and 96% respectively. In general, the classification is least effective for retrograde orbits and high inner eccentricities.
- Our MLP model is a neural network of six hidden layers of 50 neurons each. It performs even better than Equation 3.4 in classification and has an overall classification score of 95%. The precisions of stable and unstable systems are 93% and 96% respectively, while the recalls are 92% and 96% respectively.
- The classification works best in the parameter ranges of mass ratios  $10^{-2} \leq q_{\text{in}} \leq 1$ ,  $10^{-2} \leq q_{\text{out}} \leq 10^2$  and semimajor axis ratio  $10^{-4} < \alpha < 1$ . This range corresponds to a major fraction of hierarchical triple-star systems.
- Our MLP model is publicly available on Github  in the form of a simple Python script.

# Chapter 4

## Dynamical stability of quadruple-star systems

This chapter reproduces the paper [Vynatheya et al. \(2023b\)](#), titled “*Quadruple-star systems are not always nested triples: a machine learning approach to dynamical stability*”, and published in the journal MNRAS. The initial setup, code runs, and final analysis were all conducted by me. The text has been written mainly by me, with contributions from Rosemary Mardling and Adrian Hamers.

### 4.1 Introduction

Recent decades have witnessed an increasing interest in the study of small- $N$  stellar systems, both from the theoretical and observational point of view. Advances in telescope technology have revealed the true stellar multiplicity of many ‘single’ and ‘binary’ star systems and hence the prevalence of multiple-star systems, vindicating predictions of theories of star formation such as [Reipurth & Clarke \(2001\)](#) and [Delgado-Donate et al. \(2004\)](#). A comprehensive list of all observed multiple-star systems detected to date can be found in the Multiple Star Catalog ([Tokovinin, 1997, 2018b](#)). In particular, [Moe & Di Stefano \(2017\)](#) found that over 50% of high-mass O- and B-type stars dwell in triples and quadruples, compared to less than 10% in the solar-mass range. These high-mass stars (which eventually become neutron stars and black holes) are crucial for many high-energy stellar phenomena including supernovae, X-ray binaries and gravitational wave events. Thus, their study is incomplete without understanding triples and quadruples, and consequently their dynamics and long-term stability.

The study of quadruple stability is also crucial in the context of population synthesis studies of quadruples (e.g., [Hamers et al., 2021b](#); [Vynatheya & Hamers, 2022](#), in the context of merger of black holes and neutron stars). In such statistical studies, it is important that the initial sampling of quadruple systems is appropriately carried out. An inaccurate stability criterion can result in either a significant fraction of unstable systems (which are either short-lived or cannot form at all) being part of the sampled data set or many stable

systems being left out. In other words, a poor classifier can systematically alter calculated rates of stellar events and other statistics.

In our previous paper (Vynatheya et al., 2022; henceforth V+22), we discussed, in detail, the stability of triples and introduced two methods to classify them into ‘stable’ and ‘unstable’ systems. The first classifier involved an algebraic criterion, an improvement on the pre-existing stability criterion by Mardling & Aarseth (2001) (henceforth MA01). The second classifier, which is more relevant to this study, was a machine learning algorithm – a multi-layer perceptron (MLP). In this paper, we present similar MLP models for 2+2 and 3+1 quadruple-star systems (see Figure 1.2 for a mobile diagram of a triple, a 2+2 and a 3+1 quadruple). Thus, this study is a sequel of V+22, with many of the details of classification being similar.

The notable triple stability criterion of MA01 (see also Mardling & Aarseth, 1999) is often used to empirically determine quadruple stability, by considering quadruples as ‘nested’ triples and applying the condition twice. The ‘nested’ triples in the two types of hierarchical quadruples are described below (see Figure 1.2 for notation reference) :

- 2+2 quadruples: The first triple is the system of the inner binary  $b_{\text{in}1}$ , with stars of masses  $m_1$  and  $m_2$ , and a point mass approximated tertiary companion  $m_3 + m_4$ . Similarly, the second triple is the system of the inner binary  $b_{\text{in}2}$ , with stars of masses  $m_3$  and  $m_4$ , and a point mass approximated tertiary companion  $m_1 + m_2$ . The outer binary in both cases is  $b_{\text{out}}$ .
- 3+1 quadruples: The first triple is the system of the inner binary  $b_{\text{in}}$ , with stars of masses  $m_1$  and  $m_2$ , and the intermediate star  $m_3$  as the tertiary companion. The outer binary in this scenario is, hence,  $b_{\text{mid}}$ . The second triple is the system of the intermediate binary  $b_{\text{mid}}$ , with stars of masses  $m_3$  and  $m_1 + m_2$  (approximated as a point mass), and the outer star  $m_4$  as the tertiary companion. The outer binary is  $b_{\text{out}}$ .

There have also been numerous studies in the past on the stability of hierarchical (e.g., Eggleton & Kiseleva, 1995; Valtonen & Karttunen, 2006) and non-hierarchical (e.g., Stone & Leigh, 2019; Ginat & Perets, 2021) triples. More recently, Grishin et al. (2017) examined the effect of orbit inclinations on stability in the context of planets. Lalande & Trani (2022) trained a convolutional neural network on a limited time series of orbital parameters to predict the long-term stability of triples. Hayashi et al. (2022) conducted a detailed study on the disruption timescales of triples, rather than just classifying them as stable or unstable. Tory et al. (2022) came up with an updated triple-stability criterion which takes into account the varying dependence on outer mass ratio. However, studies on quadruple-star systems are few in number, and no quadruple-specific stability criteria have been investigated.

An important aspect of triple and quadruple dynamics is long-term secular evolution, which becomes important in timescales much larger than orbital timescales. For example, in triples, the lowest-order approximation of secular evolution manifests as the (von Zeipel)-Lidov-Kozai (LK) oscillations (von Zeipel, 1910; Lidov, 1962; Kozai, 1962), which



are periodic changes in the inner orbit eccentricities and mutual inclinations. Consequently, quadruples also undergo such evolution.

Hamers et al. (2015) analysed 3+1 quadruples in a secular-averaged approach and found that initially partially coplanar systems can become inclined if the ratio of the inner to the outer periods of LK oscillations  $\mathcal{R}_0 = P_{\text{LK,inner}}/P_{\text{LK,outer}} \sim 1$ . Grishin et al. (2018) found that chaotic mutual inclination changes can occur in 3+1 quadruples under similar conditions, and that short-range forces, such as tides and rotation, can aid in inner eccentricity excitation. A detailed study of secular dynamics in both 2+2 and 3+1 quadruples was carried out by Hamers & Lai (2017). They showed that high mutual inclinations, and consequently high inner eccentricities, can be achieved when the precession timescale of the outer angular momentum vector due to secular evolution is comparable to the LK period of the inner ‘nested’ triple. Due to these factors, quadruple systems can have shorter disruption timescales, and hence can become more unstable, than their equivalent ‘nested’ triples. Our study also arrives at a similar conclusion, but through a very different approach.

This paper is arranged as follows. Section 4.2 introduces the *N*-body code and subsequently, discusses dynamical stability. Section 4.3 goes into the details of the machine learning classifiers we use to determine quadruple stability. In Section 4.4, we compare the physical differences between triples and quadruples by carrying out limited parameter space studies. We present the results of the classifications in Section 4.5. Section 4.6 is the discussion and Section 4.7 concludes.

## 4.2 *N*-body code and stability

For accurate integration of few-body systems with arbitrary masses we used the accurate direct *N*-body code **MSTAR** (Rantala et al., 2020), restricting the study to Newtonian gravity. The latter has the advantage of making the problem scale-free (in the sense that only mass and length *ratios* are relevant), but the disadvantage of excluding the stabilizing effect of general relativity when orbital speeds are an appreciable fraction of the speed of light, with post-Newtonian terms restricting the growth of eccentricity.

Consequently, the scale-free parameters for 2+2 quadruples can be defined as follows (same notation as in Figure 1.2):

- Three mass ratios  $q_{\text{in}_1} = m_2/m_1 \leq 1$  ( $m_2 \leq m_1$ ),  $q_{\text{in}_2} = m_4/m_3 \leq 1$  ( $m_4 \leq m_3$ ), such that  $m_1 + m_2 \geq m_3 + m_4$ , and  $q_{\text{out}} = (m_3 + m_4)/(m_1 + m_2) \leq 1$ .
- Two semi-major axis ratios  $\alpha_{\text{in}_1\text{-out}} = a_{\text{in}_1}/a_{\text{out}} < 1$  and  $\alpha_{\text{in}_2\text{-out}} = a_{\text{in}_2}/a_{\text{out}} < 1$ , where  $a_{\text{in}_1}$ ,  $a_{\text{in}_2}$  and  $a_{\text{out}}$  are the semi-major axes of the binaries  $b_{\text{in}_1}$ ,  $b_{\text{in}_2}$  and  $b_{\text{out}}$  respectively.
- Three orbital eccentricities  $0 \leq e_{\text{in}_1} < 1$ ,  $0 \leq e_{\text{in}_2} < 1$  and  $0 \leq e_{\text{out}} < 1$  of binaries  $b_{\text{in}_1}$ ,  $b_{\text{in}_2}$  and  $b_{\text{out}}$  respectively.
- Three mutual inclinations  $i_{\text{in}_1\text{-in}_2}$ ,  $i_{\text{in}_1\text{-out}}$  and  $i_{\text{in}_2\text{-out}}$  between the the binary pairs  $b_{\text{in}_1}\text{-}b_{\text{in}_2}$ ,  $b_{\text{in}_1}\text{-}b_{\text{out}}$  and  $b_{\text{in}_2}\text{-}b_{\text{out}}$  respectively

Similarly, the scale-free parameters for 3+1 quadruples can be defined as follows (same notation as in Figure 1.2):

- Three mass ratios  $q_{\text{in}} = m_2/m_1 \leq 1$  ( $m_2 \leq m_1$ ),  $q_{\text{mid}} = m_3/(m_1 + m_2)$  and  $q_{\text{out}} = m_4/(m_1 + m_2 + m_3)$ .
- Two semi-major axis ratios  $\alpha_{\text{in-mid}} = a_{\text{in}}/a_{\text{mid}} < 1$  and  $\alpha_{\text{mid-out}} = a_{\text{mid}}/a_{\text{out}} < 1$ , where  $a_{\text{in}}$ ,  $a_{\text{mid}}$  and  $a_{\text{out}}$  are the semi-major axes of the binaries  $b_{\text{in}}$ ,  $b_{\text{mid}}$  and  $b_{\text{out}}$  respectively.
- Three orbital eccentricities  $0 \leq e_{\text{in}} < 1$ ,  $0 \leq e_{\text{mid}} < 1$  and  $0 \leq e_{\text{out}} < 1$  of binaries  $b_{\text{in}}$ ,  $b_{\text{mid}}$  and  $b_{\text{out}}$  respectively.
- Three mutual inclinations  $i_{\text{in-mid}}$ ,  $i_{\text{in-out}}$  and  $i_{\text{mid-out}}$  between the the binary pairs  $b_{\text{in}}-b_{\text{mid}}$ ,  $b_{\text{in}}-b_{\text{out}}$  and  $b_{\text{mid}}-b_{\text{out}}$  respectively

This results in a total of 11 parameters (each for 2+2 and 3+1 quadruples) on which stability can depend on. The three mutual inclinations are functions of individual orbit inclinations and longitudes of ascending node. However, non-identical combinations of the longitudes of ascending node can result in identical values of mutual inclinations. Our study does not take these degeneracies into account. It should also be noted that another set of orbital angles, the arguments of periapsis, can be important in the study of dynamical stability (see [Mardling, 2008](#)), thereby increasing the number of potentially dependent parameters to 14. Nevertheless, as in V+22, we simplified our problem by disregarding the dependence on the arguments of periapsis.

After setting up the initial parameters and the  $N$ -body integrator, one requires a robust stability criterion. This is crucial since the dynamical stability of a system can depend on the time scale considered, and hence, our results can differ with varying integration times. To handle this, we used a chaos theory-inspired approach to quantify stability, similar to MA01: given an initial data set of quadruple (or triple) systems, we constructed a nearly identical set of ‘ghost’ systems with the same initial conditions, except for a tiny change in one of the parameters. We chose to increase the inner semi-major axis by  $10^{-6}$  AU for this purpose. In the case of 2+2 quadruples, where there are two inner binaries, the one with the smaller total mass was chosen for the change of semi-major axis (in hindsight, it might have been better to choose the inner binary with the smallest binding energy). Subsequently, both data sets, the original and the ‘ghost’, were run for 100 outer orbits. The justification of the choice of 100 outer orbits is similar to V+22 (also see Figure 1 of V+22) – most unstable systems become unbound well before this time. Any system which becomes unbound within this duration was deemed unstable. However, if a system remained bound, we checked for the divergence between the original and its corresponding ‘ghost’ system (similar to Lyapunov stability; see [Portegies Zwart et al., 2022](#); [Hayashi et al., 2023](#)). In particular, one can define a quantity dependent on time  $t$ :

$$\delta(t) = \frac{a_{\text{in,orig}}(t) - a_{\text{in,ghost}}(t)}{a_{\text{in,orig}}(t)} \quad (4.1)$$

Here,  $a_{\text{in}}$  refers to the inner semi-major axis (which is initially slightly offset) and the subscripts refer to the original and ‘ghost’ systems.  $\delta(t)$  quantifies the relative divergence between the orbits or the degree of chaos. A bound system was deemed unstable if, at any time step,  $\delta(t)$  exceeds  $10^{-2}$ . We chose the threshold value  $10^{-2}$  after analysing the plots of  $\delta(t)$  vs.  $t$  for a number of stable and unstable systems. This ‘ghost’ system stability definition is reasonable because unstable systems are also chaotic in nature.

It is worth mentioning that V+22 used a different defining criterion for stability, where a system (also integrated for 100 outer orbits) is considered unstable when there is an escape of a body or a significant change in semi-major axes (see Section 4.6). Thus, in this study, when we compared triple stability with quadruple stability, we used the ‘ghost’ system approach for both to be consistent.

## 4.3 Machine learning classifier

In this era of computing and big data, machine learning (ML) has become an indispensable tool for classification and regression. ML algorithms ‘learn’ from prior data to make predictions on unseen data. The specifics of our classification algorithm (to determine dynamical stability) are laid out in the following subsections.

### 4.3.1 Data set and initial conditions

For machine learning (see Section 4.3), it is essential to have an evenly sampled parameter space. To that end, we sampled as follows (for both 2+2 and 3+1 quadruples):

- Masses were sampled log uniformly over 1 order of magnitude, such that the most massive star can be at most 10 times as massive as the least massive. More skewed masses were not considered because the integration of such systems could take longer. Mass ratios were then calculated.
- Semi-major axes were sampled uniformly as ratios of the outer semi-major axis (which was kept constant since the problem is scale-free).
- Eccentricities were sampled uniformly from 0 to 0.95. Higher eccentricities were not considered since they could result in close approaches (depending on the semi-major axes), thereby lengthening computing time.
- Orbital angles – inclinations, longitudes of ascending node, arguments of periapsis – and mean anomalies were sampled isotropically to ensure no biases. Mutual inclinations were then calculated from the inclinations and the longitudes. It should be emphasized that the other angles were *not* considered as parameters for machine learning.

Moreover, we ensured that an inner orbit’s apoapsis is smaller than an outer orbit’s periapsis to maintain the hierarchy. However, secular evolution can result in increased inner

eccentricities, which can disrupt hierarchy later on. We also restricted sampling quadruple systems ‘close’ to the MA01 classification boundary of the two ‘nested’ triples that constitute them. The MA01 formula is as follows:

$$\frac{R_{p,\text{crit}}}{a_{\text{in}}} = 2.8 \left[ (1 + q_{\text{out}}) \frac{1 + e_{\text{out}}}{(1 - e_{\text{out}})^{1/2}} \right]^{2/5} \left( 1 - \frac{0.3i_{\text{mut}}}{\pi} \right) \quad (4.2)$$

Here,  $R_p = a_{\text{out}}(1 - e_{\text{out}})$ , ‘out’ and ‘in’ refer to two orbits relative to each other. If  $R_p > R_{p,\text{crit}}$ , a triple is called MA01 stable, else MA01 unstable. A quadruple is only considered MA01 stable if both its ‘nested’ triples are as well. In order to ensure that there were comparable numbers of stable and unstable systems for the purpose of good machine learning classification, we excluded 70% (80%) of sampled MA01 unstable 2+2 (3+1) quadruples since they outnumber MA01 stable quadruples for our set of initial conditions.

After sampling the data set consisting of  $5 \times 10^5$  2+2 and 3+1 quadruple systems each, we created an equal number of ‘ghost’ systems as described in Section 4.2. This data is further split into training (80%) and testing data (20%) for the classification algorithm. The training data is used to build the classifier, while the testing data is used to evaluate its performance. We constructed a similar data set (and a ‘ghost’ data set) for triple-star systems to compare with quadruples.

For the  $N$ -body simulations, we limited the run time for an individual system to five hours. Any system which took longer was halted and ignored. The fractions of such systems for triples, 2+2 quadruples and 3+1 quadruples were found to be  $8.3 \times 10^{-4}$ ,  $1.4 \times 10^{-3}$  and  $2.8 \times 10^{-2}$  respectively. Since these fractions were very small, they did not significantly affect machine learning.

### 4.3.2 Multi-layer perceptron (MLP) - implementation

As in V+22, we implemented the simplest form of a feed-forward artificial neural network (ANN) (McCulloch & Pitts, 1943; see Hastie et al., 2009 for review) – the Multi-layer perceptron (MLP) (Rosenblatt, 1958). We used the `scikit-learn` (Pedregosa et al., 2011) package of Python3 for this purpose. Many of the details of the implementation of the MLP network are very similar to Section 5 of V+22. Nevertheless, for completion, we provide a summary below.

An MLP network consists of an input layer of our 11 initial parameters, multiple hidden layers with many neurons each and an output layer with a single output from 0 (‘stable’) to 1 (‘unstable’). Firstly, the training data is passed as input. Each subsequent layer then passes information (through weights and an activation function) forward to its immediate neighbour, resulting in a single-valued output. Finally, the algorithm updates the weights (through gradient descent) to bring the predicted outputs closer to the actual outputs. This process is iterated until an optimum classification is reached. We employed the logistic activation function  $\phi(x) = 1/(1 + e^{-x})$  and the Adam solver (Kingma & Ba, 2014) for gradient descent.

It is also important to note that tuning the hyper-parameters of an MLP network is crucial for a good classification. We tuned the hyper-parameters by running a grid of MLP models (coupled with cross-validating), and choosing the best-performing ones, mentioned below:

- Network architecture: 4 hidden layers of 50 neurons each.
- Batch size (number of samples used for gradient descent): 1000.
- L2 regularization term (penalty term for large weights):  $10^{-4}$ .
- Learning rate (step-size to update weights): 0.01.

The same hyper-parameters were used for 2+2 and 3+1 quadruples, and triples, for training. Training these networks takes about 30 minutes on 64 cores of an AMD EPYC 7742 CPU. The results of machine learning are summarised in Section 4.5.

## 4.4 From a triple to a quadruple

In addition to machine learning, which is a brute force classifier, we also wished to look at the physical differences between triple- and quadruple-star systems in a bottom-up approach. Given the large number of parameters needed to specify quadruple and triple configurations, we restricted our study to initially periapsis-aligned co-planar orbits with zero initial orbital phases. This reduces the intricate dependencies on 3 of the 11 parameters for quadruples, thereby simplifying our analysis.

To compare quadruples with triples, we started with a co-planar stable triple-star system with the following five parameters: semi-major axis ratio  $\alpha_{\text{tr}}$ , mass ratios  $q_{\text{in,tr}}$  and  $q_{\text{out,tr}}$ , and eccentricities  $e_{\text{in,tr}}$  and  $e_{\text{out,tr}}$ . We then split one of the stars (in a co-planar way) into a ‘new’ binary to form a quadruple. Thus, we get three extra parameters from the ‘new’ binary: semi-major axis  $\alpha_{\text{new}}$ , mass ratio  $q_{\text{in,new}}$ , and eccentricities  $e_{\text{in,new}}$ . The splitting for the two types of quadruples is done as follows:

- 2+2 quadruples: The outer star is split. The original triple parameters are equivalent to:  $\alpha_{\text{tr}} \equiv \alpha_{\text{in}_1\text{-out}}$ ,  $q_{\text{in,tr}} \equiv q_{\text{in}_1}$ ,  $q_{\text{out,tr}} \equiv q_{\text{out}}$ ,  $e_{\text{in,tr}} \equiv e_{\text{in}_1}$ ,  $e_{\text{out,tr}} \equiv q_{\text{out}}$ . The ‘new’ triple parameters are equivalent to:  $\alpha_{\text{new}} \equiv \alpha_{\text{in}_2\text{-out}}$ ,  $q_{\text{in,new}} \equiv q_{\text{in}_2}$ ,  $e_{\text{in,new}} \equiv e_{\text{in}_2}$ .
- 3+1 quadruples: One of the inner stars is split. The original triple parameters are equivalent to:  $\alpha_{\text{tr}} \equiv \alpha_{\text{mid-out}}$ ,  $q_{\text{in,tr}} \equiv q_{\text{mid}}$ ,  $q_{\text{out,tr}} \equiv q_{\text{out}}$ ,  $e_{\text{in,tr}} \equiv e_{\text{mid}}$ ,  $e_{\text{out,tr}} \equiv q_{\text{out}}$ . The ‘new’ triple parameters are equivalent to:  $\alpha_{\text{new}} \equiv \alpha_{\text{in-mid}}$ ,  $q_{\text{in,new}} \equiv q_{\text{in}}$ ,  $e_{\text{in,new}} \equiv e_{\text{in}}$ .

Subsequently, we varied the parameters of the ‘new’ binary (namely semi-major axis, eccentricity and mass ratio) two at a time to discern their effects on stability. Meanwhile, the other parameters were kept constant. Tables 4.1 and 4.2 show the different parameter space slices made for 2+2 and 3+1 quadruples respectively. For each parameter space

Slice	$\alpha_{\text{in}_1\text{-out}}$	$\alpha_{\text{in}_2\text{-out}}$	$q_{\text{in}_1}$	$q_{\text{in}_2}$	$q_{\text{out}}$	$e_{\text{in}_1}$	$e_{\text{in}_2}$	$e_{\text{out}}$
Fiducial	0.25	V   V	1	1   V	1	0	V   0	0
Low $q_{\text{in}_1}$	0.2	V   V	<b>1/9</b>	1   V	1	0	V   0	0
Low $q_{\text{out}}$	0.25	V   V	1	1   V	<b>1/9</b>	0	V   0	0
High $e_{\text{in}_1}$	0.175	V   V	1	1   V	1	<b>0.5</b>	V   0	0
High $e_{\text{out}}$	0.075	V   V	1	1   V	1	0	V   0	<b>0.5</b>

Table 4.1: Parameter space slices (zero inclination) considered for 2+2 quadruples. The ‘Fiducial’ slice has equal masses and zero eccentricities, while other slices change either the masses or the eccentricities. The parameters with values ‘V’ are varied to make grid-sampled plots like Figure 4.1 (the ‘Fiducial’ slices), the left (right) value being when the mass ratios (eccentricities) are varied with the semi-major axes of the ‘new’ binary.

Slice	$\alpha_{\text{in-mid}}$	$\alpha_{\text{mid-out}}$	$q_{\text{in}}$	$q_{\text{mid}}$	$q_{\text{out}}$	$e_{\text{in}}$	$e_{\text{mid}}$	$e_{\text{out}}$
Fiducial	V   V	0.25	1   V	1/2	1/3	V   0	0	0
High $q_{\text{mid}}$	V   V	0.175	1   V	<b>7/2</b>	1/9	V   0	0	0
High $q_{\text{out}}$	V   V	0.15	1   V	1/2	<b>7/3</b>	V   0	0	0
Low $q_{\text{mid}}$	V   V	0.2	1   V	<b>1/6</b>	3/7	V   0	0	0
Low $q_{\text{out}}$	V   V	0.25	1   V	1/2	<b>1/9</b>	V   0	0	0
High $e_{\text{mid}}$	V   V	0.175	1   V	1/2	1/3	V   0	<b>0.5</b>	0
High $e_{\text{out}}$	V   V	0.075	1   V	1/2	1/3	V   0	0	<b>0.5</b>

Table 4.2: Parameter space slices (zero inclination) similar to Table 4.1 for 3+1 quadruples. Figure 4.2 represents the ‘Fiducial’ slices. (It should be noted that, in our slices,  $q_{\text{out}}$  also varies when  $q_{\text{mid}}$  is varied, but not vice-versa.)

slice, we make two grid-sampled plots of stability, one for  $q_{\text{in,new}}$  vs.  $\alpha_{\text{new}}$  and another for  $e_{\text{in,new}}$  vs.  $\alpha_{\text{new}}$ . We chose grid dimensions of  $25 \times 25$  to sufficiently populate the limited parameter space slices.

Figures 4.1 and 4.2 represent these stability plots for the ‘Fiducial’ parameter space slices of 2+2 and 3+1 quadruples respectively (see Section 4.5 for details).

## 4.5 Results

We trained three MLP models in total, the ‘2+2 MLP’, the ‘3+1 MLP’ and the ‘triple MLP’ for 2+2 quadruples, 3+1 quadruples and triples respectively. To be clear, the ‘triple MLP’ model differs from a very similar model presented in V+22 owing to their different defining criteria for stability.

Classifier	$S$	$P_{\text{stable}}$	$P_{\text{unstable}}$	$R_{\text{stable}}$	$R_{\text{unstable}}$
MA01	0.83	0.77	0.96	0.95	0.78
triple MLP	0.88	0.85	0.94	0.93	0.87
2+2 MLP	0.94	0.94	0.95	0.94	0.95

Table 4.3: Classification results of different classifiers for 2+2 quadruples – overall scores, precisions and recalls for truly stable and unstable systems.

### 4.5.1 MLP model performances

To quantify how well a classification model performs, one needs to focus not only on the overall accuracy but also on individual class (either ‘stable’ or ‘unstable’) accuracies. Since there are only two classes, we can define four quantities: the numbers of true stable (TS), true unstable (TU), false stable (FS) and false unstable (FU) systems. True stable (unstable) systems are correctly classified as ‘stable’ (‘unstable’) by the classifier, while false stable (unstable) systems are, from  $N$ -body simulations, actually unstable (stable) but wrongly classified as ‘stable’ (‘unstable’) by the classifier. Using these 4 quantities, one can define the following:

- Overall score: Total fraction of systems predicted correctly, independent of class;  $S = T/(T + F)$ , where  $T = TS + TU$  and  $F = FS + FU$ .
- Precision: Fraction of predicted ‘stable’/‘unstable’ (by the classifier) systems that are actually stable/unstable (from  $N$ -body simulations);  $P_{\text{stable}} = TS/(TS + FS)$  and  $P_{\text{unstable}} = TU/(TU + FU)$ .
- Recall: Fraction of actually stable/unstable systems (from  $N$ -body simulations) that are predicted ‘stable’/‘unstable’ (by the classifier);  $R_{\text{stable}} = TS/(TS + FU)$  and  $R_{\text{unstable}} = TU/(TU + FS)$ .

The precisions and recalls, respectively, are the quantities which detail the validity and completeness of a class-wise prediction.

Tables 4.3 and 4.4 represent the scores, precisions and recalls of different classifiers for 2+2 and 3+1 quadruples respectively. ‘MA01’ refers to the triple stability criterion by MA01, with the formula being applied to the ‘nested’ triples (Section 4.1) that make up a quadruple. Similarly, ‘triple MLP’ refers to that model being applied to the ‘nested’ triples. The other two MLP models ‘2+2 MLP’ and ‘3+1 MLP’ are applied directly to the respective quadruples.

The performance indicators reveal that the quadruple MLP models are significantly better in classification than the ‘nested’ triples approach, especially for 3+1 quadruples. This is because 3+1 quadruples show the unique behaviour of the intermediate eccentricity becoming excited by the outer orbit, subsequently triggering instability of the inner triple.

The ‘triple MLP’ model performs better than ‘MA01’ but still falls short of good classification. The low values of the indicators  $P_{\text{stable}}$  (0.85 for 2+2 and 0.59 for 3+1) and

Classifier	$S$	$P_{\text{stable}}$	$P_{\text{unstable}}$	$R_{\text{stable}}$	$R_{\text{unstable}}$
MA01	0.56	0.54	0.95	0.95	0.55
triple MLP	0.66	0.59	0.97	0.96	0.62
3+1 MLP	0.93	0.91	0.95	0.91	0.95

Table 4.4: Classification results similar to Table 4.3 for 3+1 quadruples.

$R_{\text{unstable}}$  (0.87 for 2+2 and 0.62 for 3+1) tell us that the ‘triple MLP’ (and ‘MA01’) model overestimates the number of stable systems. Specifically, for 3+1 quadruples, the number of false stable systems is so large that the model performs only slightly better than a random classifier.

### 4.5.2 Analysing the stability criterion

We also performed a sanity check of our stability criterion by investigating the boundedness of a limited sample (to keep the computational expense in check) of systems over 1000 outer orbits<sup>1</sup>. A random sample of 1000 (out of an initial  $5 \times 10^6$ ) each of 2+2 and 3+1 quadruples compare with their assigned stability labels as follows:

- 92% and 85% respectively of 2+2 and 3+1 quadruples which are classified ‘stable’ remain bound after 1000 outer orbits.
- 92% and 91% respectively of 2+2 and 3+1 quadruples which are classified ‘unstable’ become unbound within 1000 outer orbits.

To understand these numbers, we first define the LK timescale of a triple as follows (see [Antognini, 2015](#); [Naoz, 2016](#)):

$$P_{\text{LK}} \approx \frac{P_{\text{out}}^2}{P_{\text{in}}} \left( \frac{m_{\text{in,tot}} + m_{\text{out}}}{m_{\text{out}}} \right) (1 - e_{\text{out}})^{3/2} \quad (4.3)$$

Very stable systems tend to have  $P_{\text{out}} \gg P_{\text{in}}$  and low  $e_{\text{out}}$  for both ‘nested’ triples, and hence have long LK periods. On the other hand, very unstable systems have short LK periods for at least one of the ‘nested’ triple, in the order of 100 outer orbits. The relatively low agreement fraction for 3+1 quadruples (85%) is primarily due to systems whose periods of LK oscillation  $P_{\text{LK}}$  of the two ‘nested’ triples differ by less than one order of magnitude. We corroborated this by running another limited sample of 1000 quadruples satisfying this condition, which corresponds to the chaotic regime detailed in [Hamers & Lai \(2017\)](#) and [Grishin et al. \(2018\)](#). Moreover, systems with lower inclination systems have similar agreement fractions as those with higher inclination, i.e., chaotic secular evolution

<sup>1</sup>We do not employ the ‘ghost’ orbit stability criterion in this case, and instead examine the boundedness. This is because the  $\delta(t)$  threshold stated in Section 4.2 was tailored to integration over 100 outer orbits, and not 1000.



can happen for low initial inclinations as well (Hamers & Lai, 2017). This fraction may reduce further if the  $N$ -body integration is carried out for longer. Nevertheless, for this study, the above agreement fractions are considered adequate.

### 4.5.3 Parameter space slices

Here, we present the results of the parameter space slices described in Section 4.4. To reiterate, we restricted our study only to co-planar orbits with all orbital angles initially set to 0. Starting from a stable triple, we split one of the stars into a ‘new’ binary to make a quadruple. We then varied the ‘new’ binary parameters, detailed in Tables 4.1 and 4.2 for 2+2 and 3+1 quadruples.

Figures 4.1 and 4.2 show the grid-sampled stability plots for 2+2 and 3+1 quadruples corresponding to the ‘Fiducial’ parameter space slices in the aforementioned tables. For conciseness, the other parameter space plots are not shown, but the results are presented.

Figures 4.1a (4.2a) and 4.1b (4.2b) represent the plots of  $q_{\text{in,new}}$  vs.  $\alpha_{\text{new}}$  and  $e_{\text{in,new}}$  vs.  $\alpha_{\text{new}}$  respectively. The blue and orange points correspond to the systems designated stable and unstable, respectively, from the  $N$ -body simulations. The dotted, dashed and solid lines represent the classification boundaries of the previously-described models ‘MA01’, ‘triple MLP’ and ‘2+2 MLP’/‘3+1 MLP’ respectively. The white spaces correspond to the systems which took longer than five hours to run.

The plots indicate that the MLP classifiers perform satisfactorily, while ‘MA01’ predicts worse when  $e_{\text{in,new}}$  is varied. This is evident when the fractions of wrongly classified (‘bad’) systems are compared. Figures 4.3 and 4.4 represent the bar charts, for 2+2 and 3+1 quadruples, of these fractions in the different parameter space slices.

- For 2+2 quadruples, the fractions of ‘bad’ systems remain lower than 15% using any of the three classifiers. ‘MA01’ predicts slightly worse than the others (which are comparable) when  $e_{\text{in}_2}$  is varied. This trend is not obvious when  $q_{\text{in}_2}$  is varied, although ‘triple’ MLP performs better than the other two.
- For 3+1 quadruples, the fractions of ‘bad’ systems are higher, even beyond 25% when  $e_{\text{out}}$  is high, using classifier ‘MA01’. Again, ‘MA01’ performs the worst when  $e_{\text{in}}$  is varied, while ‘3+1 MLP’ performs the best. All classifiers predict badly when  $e_{\text{out}}$  is high.

It is apparent, even from this restricted study, that the ‘nested’ triple approximation does not work well for 3+1 quadruples, although the differences are less drastic in the co-planar case. When inclinations are included, other effects of eccentricity enhancements due to changes in mutual inclinations come into play as well, further complicating the problem.

### 4.5.4 The complete parameter space

In this section, we take a look at the complete parameter space, albeit in a simplified manner. Figure 4.5 and 4.6 display frequency polygons of the fractions of wrongly classified (‘bad’) systems as functions of the initial parameters of 2+2 and 3+1 quadruples

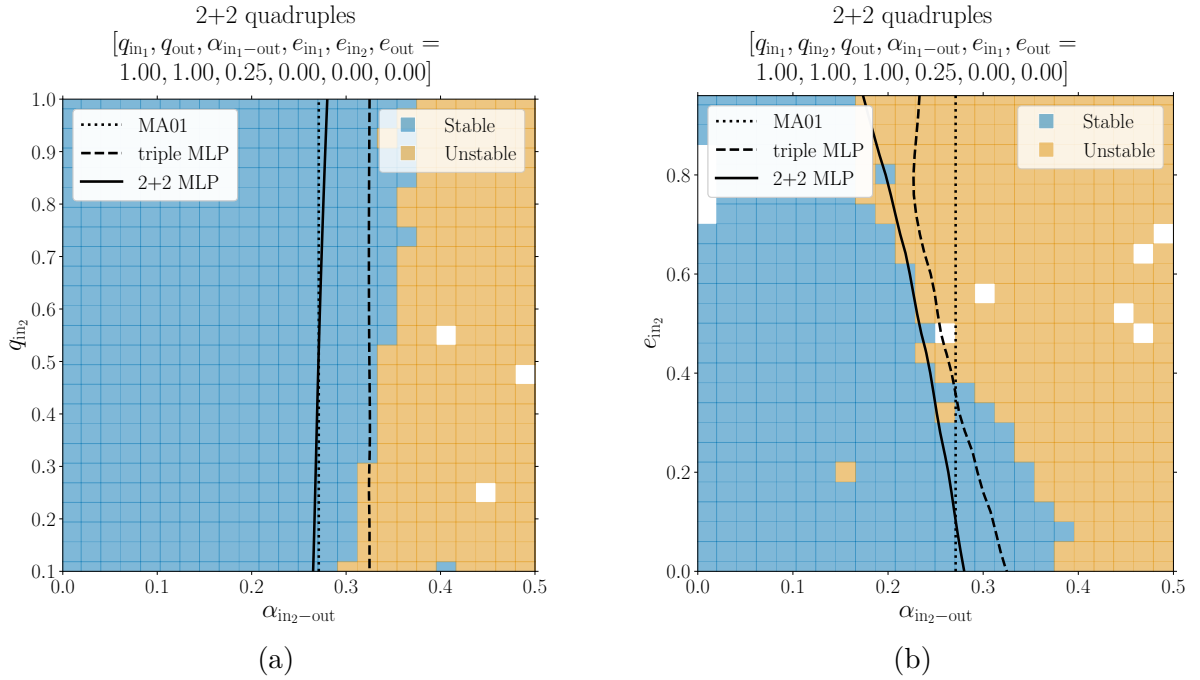


Figure 4.1: Stability plots depicting the making of a 2+2 quadruple system by splitting the outer star of a stable triple system. In panel 4.1a (4.1b), the semi-major axis ratios and the mass ratios (eccentricities) of the ‘new’ binary are grid-sampled ( $25 \times 25$  grid), corresponding to the ‘Fiducial’ slices from Table 4.1. The constant parameters are mentioned at the top of the plots. The dotted, dashed and solid lines represent the classification boundaries as given by the three classifiers in the legend. The white spaces depict systems which took too long to run.

respectively. In these plots, the dotted and solid lines represent the ‘triple MLP’ and ‘2+2 MLP’/‘3+1 MLP’ models respectively. ‘MA01’ is not depicted since it performs worse than ‘triple MLP’. The blue and orange lines correspond to false unstable (predicted ‘stable’, but actually unstable) and false stable (predicted ‘unstable’, but actually stable) systems respectively. The shaded regions represent the uncertainties in the fractions due to the relatively small number of systems being sampled in those ranges.

- For 2+2 quadruples, the fractions of false unstable systems using ‘triple MLP’ are higher than the others throughout the parameter space. In some cases, like for retrograde  $i_{in_1-in_2}$ , the false unstable fraction reaches almost 20%. Meanwhile, the fractions for ‘2+2 MLP’ remain lower than 10% for most parameter ranges. In the plot with varying  $e_{out}$  (centre-right), there is high uncertainty in the range of large  $e_{out}$  due to insufficient sampling, owing to their propensity of being unstable.
- For 3+1 quadruples, the fractions of false unstable systems using ‘triple MLP’ are extremely high, around 40%, throughout the parameter space. This result agrees with the previous sections. ‘3+1 MLP’ has significantly lower fractions, close to

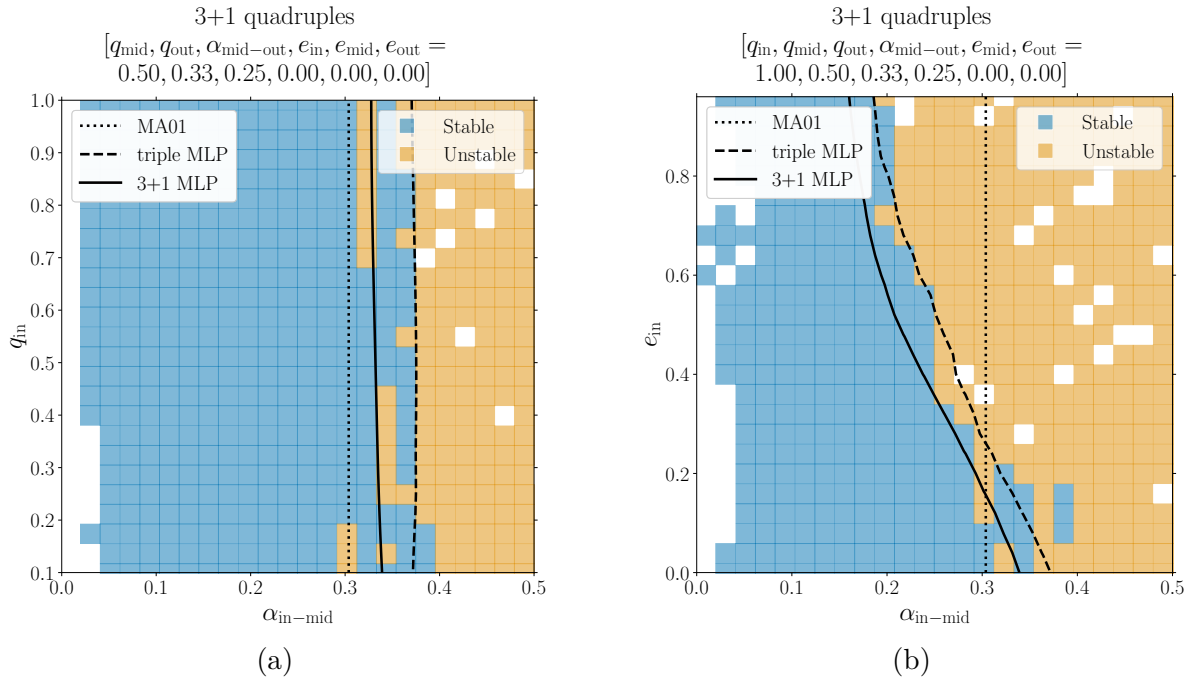


Figure 4.2: Stability plots similar to 4.1 for 3+1 quadruples. These grids correspond to the ‘Fiducial’ slices from Table 4.2.

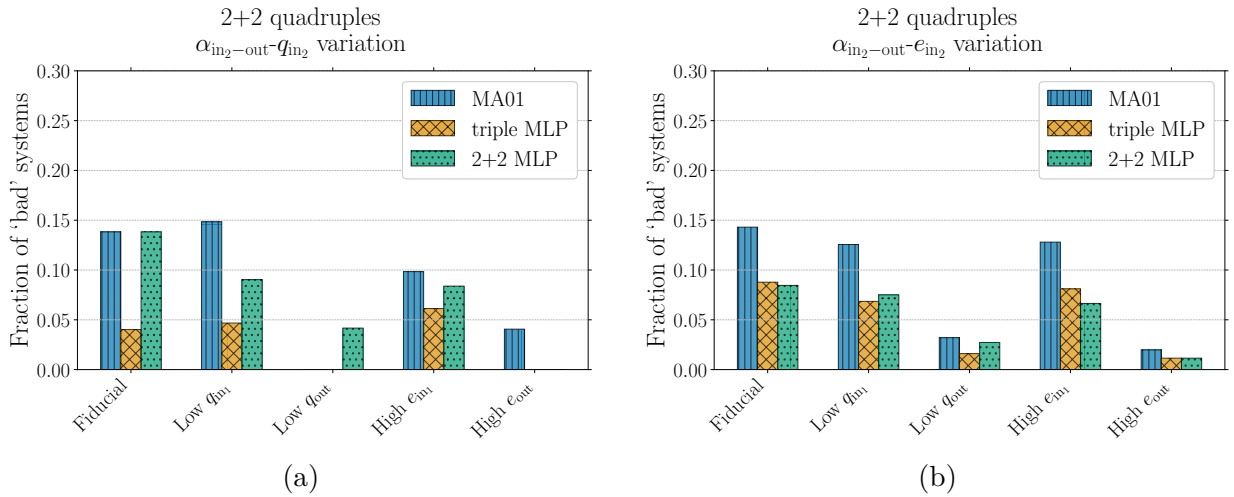


Figure 4.3: Bar plots of the fraction of 2+2 quadruple systems wrongly classified (‘bad’) by different classifiers in different zero inclination parameter space slices, like in Figure 4.1. In panel 4.3a (4.3b), the semi-major axis ratios and the mass ratios (eccentricities) of the ‘new’ binary are varied. In cases where the bars are not visible (left panel), the corresponding fractions happen to be 0. The detailed parameter values for each of the 7 parameter space slices are given in Table 4.1.

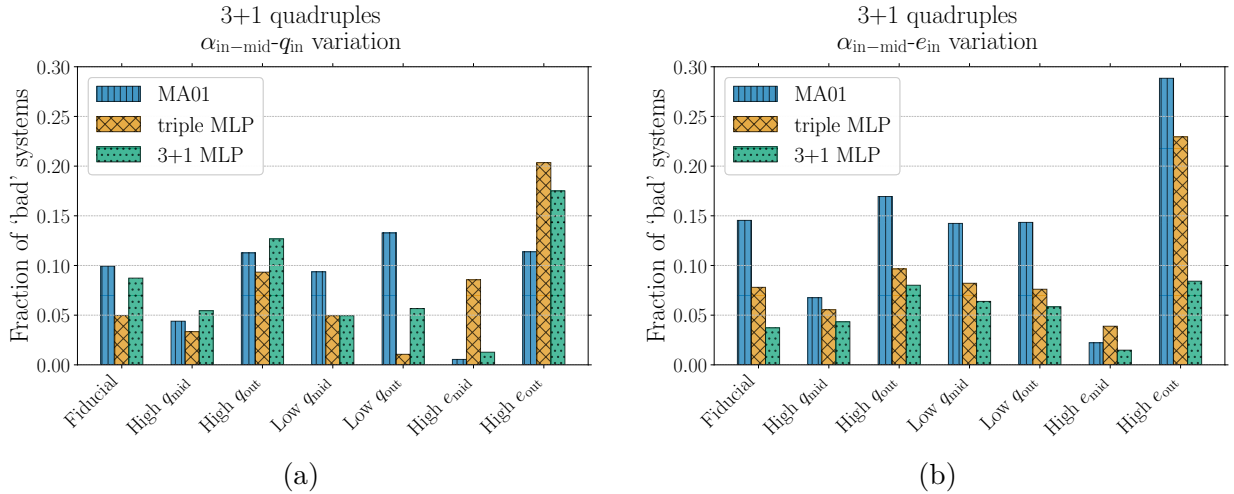


Figure 4.4: Bar plots similar to 4.3 for 3+1 quadruples. The detailed parameter values for each of the 7 parameter space slices are given in Table 4.2.

10%, although they are higher than in the 2+2 quadruple case. The plots show that ‘3+1 MLP’ has some trouble in classifying systems with high  $e_{\text{mid}}$  (again due to insufficient sampling) and near-perpendicular  $i_{\text{mid-out}}$ , where errors can reach up to 15%. Large uncertainties, in this case, are seen in the ranges of high  $q_{\text{mid}}$  and  $q_{\text{out}}$  since high mass ratio systems are improbable when individual masses range only 1 order of magnitude.

Looking at the fraction of ‘bad’ systems in the complete parameter space helps to identify the limitations of our models ‘2+2 MLP’ and ‘3+1 MLP’.

In summary, the ‘nested’ triples approximation works to some extent for 2+2 quadruples but fails for 3+1 quadruples. This also makes physical sense: for 2+2 quadruples, the point-mass approximation is carried out for the two inner binaries which are relatively tight, whereas for 3+1 quadruples, one of the approximated triples ignores the influence of the outer star. This stresses the importance of secular evolution in quadruples, as detailed by Hamers & Lai (2017) (also see Section 4.1).

## 4.6 Discussion

As mentioned in Section 4.1, this paper should be viewed as a follow-up of V+22, which improved on the existing MA01 stability criterion and also provided a machine learning MLP classifier. However, the key difference between this study and V+22 lies in the defining criterion for stability. In V+22, a triple which becomes unbound before 100 outer orbits is deemed unstable, but bound systems face another test – if there is a change of over 10% in either of the two semi-major axes during any time step, the triple is called unstable, else stable (see V+22 for details).

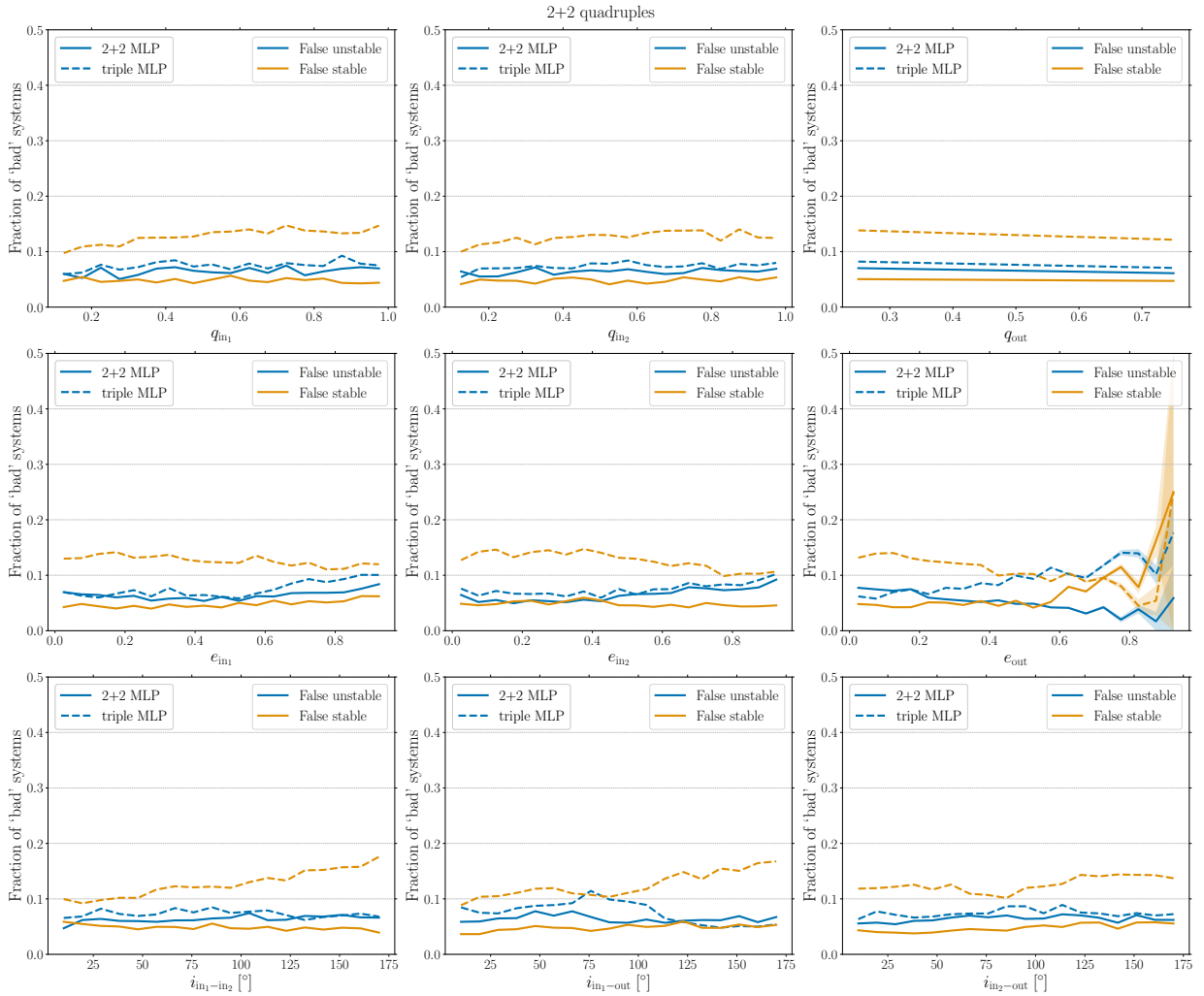


Figure 4.5: Frequency polygons of the fraction of 2+2 quadruple systems in the test data set wrongly classified (‘bad’) by the two MLP models ‘2+2 MLP’ (solid) and ‘triple MLP’ (dashed). The X-axis in each panel corresponds to the considered range of each parameter. The shaded regions (most visible in the centre-right panel in the range of high  $e_{\text{out}}$ ) depict the uncertainty in the fractions.

To check how our new defining criterion, involving ‘ghost’ systems, compared with the definition by V+22, we ran limited parameter space runs to visually see the differences. In particular, we varied two triple parameters, the semi-major axis ratio  $\alpha$  and the mutual inclination  $i_{\text{mut}}$ , keeping the others constant (similar to Figures 4 and 5 of V+22). Even with our new defining criterion, the ‘bump’ of unstable systems for highly-inclined systems was observed, lending credence to both defining criteria. Moreover, the stability boundaries using both were nearly identical, except for highly retrograde systems ( $i_{\text{mut}} \gtrsim 160^\circ$ ). V+22 predicted very few stable systems when  $\alpha \gtrsim 0.5$  values as compared to the new criterion, which predicts significant numbers of stable retrograde systems up to almost  $\alpha \sim 0.7$ . The

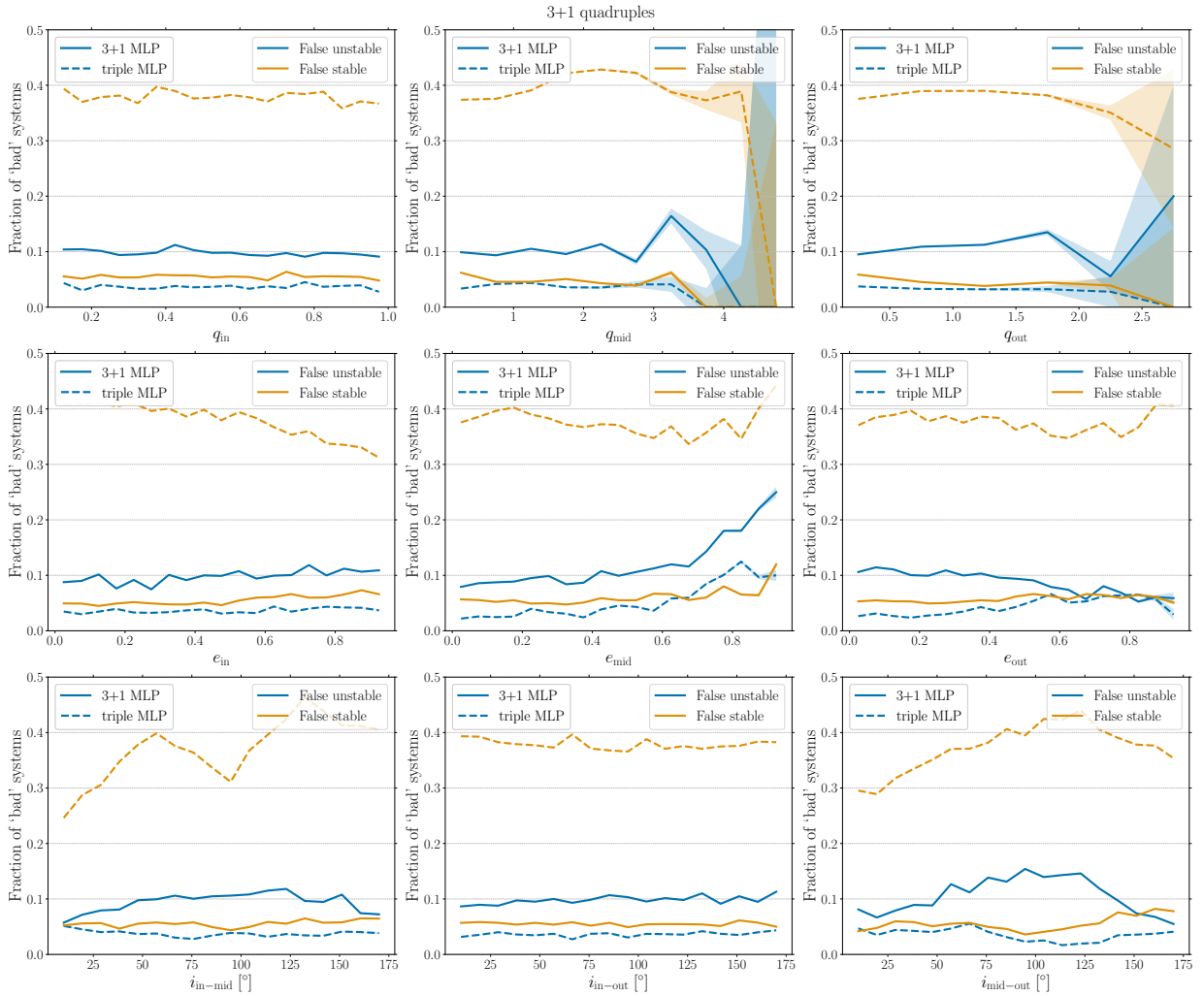


Figure 4.6: Frequency polygons similar to 4.5 for 3+1 quadruples. In this case, the shaded uncertainty regions are present in the ranges of high  $q_{\text{mid}}$  (top-centre) and  $q_{\text{out}}$  (top-right).

stability of highly retrograde triples was the only ambiguity we noticed between the two defining criteria for stability. This, in turn, implies that our MLP models may not be very reliable for such systems.

In Section 4.4, we highlighted that our limited parameter space study was restricted to systems with 0 initial mutual inclinations. This is because, unlike in triples where there is only one mutual inclination parameter, quadruples have three. Our preliminary study of varying mutual inclinations indicated that the stability boundary is not very well-defined in certain regions of the parameter space, possibly corresponding to resonances between different timescales. This is due to the chaotic evolution of mutual inclinations as detailed in Hamers et al. (2015) and Hamers & Lai (2017). The details of the resonances and the effect of mutual inclinations on stability are beyond the purview of this paper.


Finally, we note that, unlike V+22, we provide no analytical formula for the stability

of quadruples. While this was initially one of the aims of this study, it has proven to be a significant challenge, especially due to the aforementioned intricate dependencies on all three mutual inclinations. Nevertheless, our ‘2+2 MLP’ and ‘3+1 MLP’ models can easily be implemented in population synthesis studies to weed out unstable systems more efficiently than any other method to date.

## 4.7 Conclusion

We constructed efficient machine learning models – multi-layer perceptrons (MLPs) – to classify quadruple-star (2+2 and 3+1) systems based on their dynamical stability. For this purpose,  $5 \times 10^5$  2+2 and 3+1 quadruples were generated as the training data set, and they were integrated for 100 outer orbits using the direct  $N$ -body code *MSTAR* (Rantala et al., 2020). We compared the performances of ‘2+2 MLP’ and ‘3+1 MLP’ with a similar ‘triple MLP’ model, which was trained on  $5 \times 10^5$  triple systems and applied on the two ‘nested’ triples that constitute each quadruple system. We also conducted a limited parameter space study of co-planar quadruples, to compare them directly with triples in a bottom-up approach. We started with stable triple-star systems with varying initial conditions and split one of the stars to form quadruples. The important conclusions from this paper are as follows:

- The ‘2+2 MLP’ model, a neural network of 4 hidden layers of 50 neurons each, has an overall classification score of 94% on the testing data set. The precisions and recalls of stable (unstable) systems are 94% (95%) and 94% (95%) respectively. This is an improvement on the ‘triple MLP’ model with a score of 88%.
- The ‘3+1 MLP’ model, also a neural network of 4 hidden layers of 50 neurons each, has an overall classification score of 93% on the testing data set. The precisions and recalls of stable (unstable) systems are 91% (95%) and 91% (95%) respectively. This is significantly better than the ‘triple MLP’ model with a score of just 66%, which is only slightly better than a random classifier.
- For 2+2 quadruples, both ‘triple MLP’ and 2+2 MLP’ performed similarly in separating stable and unstable systems in all initially co-planar parameter space slices. The fraction of wrongly classified systems remained lower than 15%.
- For 3+1 quadruples, ‘3+1 MLP’ performed better than ‘triple MLP’ in all initially co-planar parameter space slices. However, both models performed badly for systems with high outer eccentricity  $e_{\text{out}}$ .
- The differences in classification performance between the triple and quadruple models is less drastic for co-planar systems, which implies that mutual inclination between orbits is a significant influence on stability.

- While 2+2 quadruples can still be approximated to ‘nested’ triples up to some extent, the same approximation fails for 3+1 quadruples. In general, quadruples tend to be more unstable than their corresponding ‘nested’ triples. This is crucial for population synthesis studies of quadruples which make use of this approximation.
- Our MLP models for 2+2 and 3+1 quadruples are publicly available on Github  in the form of a simple Python script. It is important to note that the initial parameter ranges mentioned in Section 4.3 need to be taken into account while using our models.



# Chapter 5

## Tidal disruptions of stars due to stellar-mass black holes

This chapter reproduces the paper [Vynatheya et al. \(2023a\)](#), titled “*Simulating the tidal disruption of stars by stellar-mass black holes using moving-mesh hydrodynamics*”, and accepted for publication in the journal A&A. The initial setup, code runs, and final analysis were all conducted by me. The text has been written mainly by me, with contributions from Taeho Ryu, Ruediger Pakmor, Selma de Mink and Hagai Perets.

### 5.1 Introduction

Tidal disruption events (TDEs) of stars by supermassive black holes (SMBHs) have been a subject of significant interest in the past decade (see [Stone et al., 2019](#); [Gezari, 2021](#) for reviews). TDEs by SMBHs are observed as transients in multiple wavelengths ([Gezari, 2021](#)), with  $\sim 100$  such events having been detected by observatories in optical (ASAS-SN: [Kochanek et al., 2017](#), ZTF: [Bellm et al., 2019](#), PTF: [Law et al., 2009](#), PS: [Chambers et al., 2016](#), ATLAS: [Tonry et al., 2018](#), SDSS: [Kollmeier et al., 2019](#), OGLE: [Udalski et al., 2015](#)), X-ray (ROSAT: [Voges et al., 1999](#), Swift: [Gehrels et al., 2004](#), XMM: [Jansen et al., 2001](#), Chandra: [Weisskopf et al., 2000](#)) and UV (GALEX: [Martin et al., 2005](#)).

In this work, we examine TDEs of stars by stellar-mass black holes or SBHs (termed  $\mu$ TDEs). These are less studied and have only garnered interest recently. Although  $\mu$ TDEs have lower observable rates ([Perets et al., 2016](#)), they can shed light on the processes occurring in the centers of globular and nuclear star clusters where they are most likely to occur. In particular, they are an important avenue in the mass growth of SBHs to form intermediate-mass black holes (IMBHs, e.g., [Stone et al., 2017b](#); [Rizzuto et al., 2023](#)). However, these studies make simplistic assumptions about the mass accreted onto a black hole after a TDE, which highlights the need for detailed simulations to model this interaction more accurately for the next generation of globular cluster simulations. Partial tidal disruptions (PTDEs), which are more likely than full tidal disruptions (FTDEs), can be responsible for the tidal capture, and subsequent encounters, of the remnant star by the

BH if the remnant ends up in a bound orbit. The remnant stars of such interactions tend to be spun up from the torque due to the BH and can have peculiar internal structures (e.g., [Alexander & Kumar, 2001](#)).

$\mu$ TDEs are also of interest in the context of low-mass X-ray binaries (LMXBs) and the newly-discovered Gaia BHs ([El-Badry et al., 2023b,a](#); [Chakrabarti et al., 2023](#)). Isolated binary evolution cannot satisfactorily explain the observed rates of binaries with BHs and low-mass stellar companions (e.g., [Podsiadlowski et al., 2003](#); [Kiel & Hurley, 2006](#)). Hence, the dynamical formation of such binaries in clusters, through PTDEs and subsequent tidal captures, may very well be a crucial process to explain them.

Accurate modeling of post-disruption orbits and the internal structure of remnant stars requires detailed hydrodynamics simulations. The first detailed study on  $\mu$ TDEs was carried out by [Perets et al. \(2016\)](#). They estimated that these events could occur in Milky Way globular clusters at a rate of  $10^{-6} \text{ yr}^{-1} \text{ MWGal}^{-1}$ , and might observationally resemble ultra-long GRB events. Similar rates were obtained for scenarios where a supernova natal kick to a newly formed BH results in a chance encounter with its binary companion. [Wang et al. \(2021\)](#) used smoothed-particle hydrodynamics (SPH) to find the fallback rates onto the BH in the case of partial  $\mu$ TDEs of polytropic stars. [Kremer et al. \(2022\)](#) performed a large suite of SPH simulations of partial- and full-disruptions, with varying BH and stellar masses, stellar polytropic indices, and impact parameters. Among other things, they observed that stellar structure plays a crucial role in the boundedness of the remnant stars after partial disruption, with the possibility of less centrally ‘concentrated’ stars ending up in hyperbolic orbits. [Xin et al. \(2024\)](#) looked at low-eccentricity ‘tidal-peeling’ events of realistic MS stars, with the star being slowly stripped away in multiple orbits.

Hydrodynamics studies on three-body encounters involving SBHs in globular clusters have also garnered interest, motivated by the significantly larger cross-sections of binary-single tidal interactions. [Lopez et al. \(2019\)](#) studied the interaction of binary BHs and polytropic stars and showed that tidal disruption can alter the spin of one of the BHs. An extensive series of studies was carried out by [Ryu et al. \(2022, 2023a,b, 2024b\)](#), using both SPH and moving-mesh codes, on the different combinations of close encounters between realistic MS stars and SBHs.

In our study, we use the moving-mesh code AREPO ([Springel, 2010](#); [Pakmor et al., 2016](#); [Weinberger et al., 2020](#)) to simulate  $\mu$ TDEs of low-mass MS stars with SBHs. It should be noted that [Ryu et al. \(2023a,b, 2024b\)](#) also employed AREPO to model TDEs with remarkable success. We generate realistic stellar models from detailed 1D MESA ([Paxton et al., 2011](#)) profiles. TDEs of MESA-generated stars by SMBHs and IMBHs have been investigated in the past (e.g., [Gallegos-Garcia et al., 2018](#); [Golightly et al., 2019](#); [Law-Smith et al., 2019, 2020](#); [Ryu et al., 2020a,b,c,d](#); [Kiroğlu et al., 2023](#)), but  $\mu$ TDE studies have typically probed polytropic stars. In this paper, we focus on the dependence of post-disruption mass, spin, and orbital parameters on the initial conditions and provide best-fit functions for the same. These fits can be incorporated into  $N$ -body or other cluster codes for better treatment of star-BH encounters.

The paper is organized as follows. In Section 5.2, we detail our simulation methodology, including our grid of initial conditions. We briefly describe the analysis of certain quantities

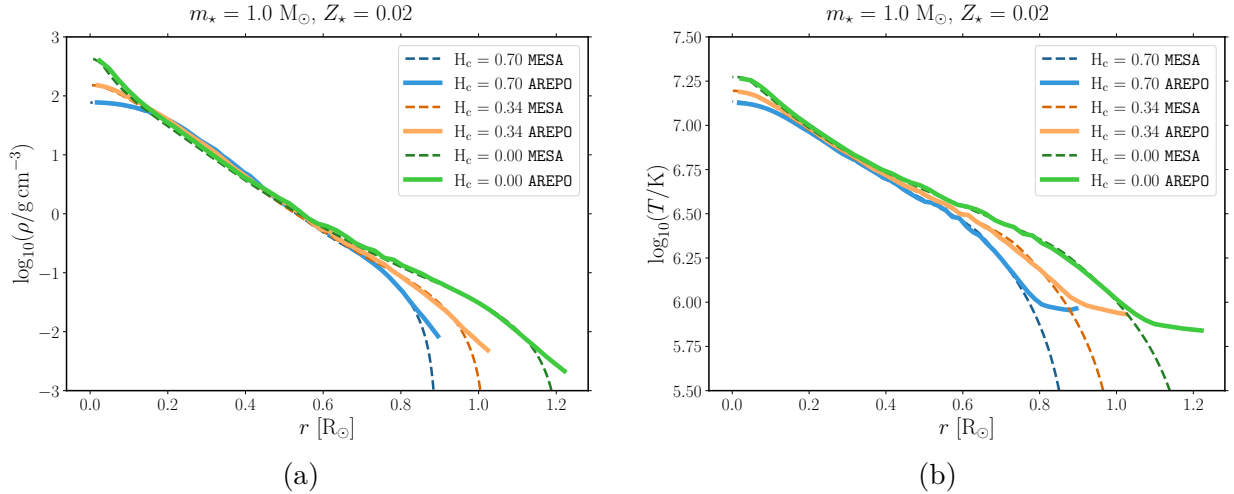


Figure 5.1: Density (left) and temperature (right) profiles of a  $1 M_{\odot}$  MS star of different models (see Table 5.1). The dashed and solid lines represent the 1D profiles generated by MESA and initialized (and subsequently relaxed for five dynamical timescales) in 3D in AREPO respectively. They agree very well over most of the range except close to the stellar surface because of smoothing during relaxation in AREPO. An older MS star (with lower  $H_c$ ) has a denser and hotter core and a puffier outer layer than a younger MS star (with higher  $H_c$ ).

in Section 5.3 and present our results and best-fit functions in Section 5.4. Section 5.5 and Section 5.6 discuss the implications of our work and conclude, respectively.

## 5.2 Methods

### 5.2.1 Hydrodynamics

We simulate the disruption of stars by black holes using the moving-mesh magnetohydrodynamics code AREPO (Springel, 2010; Pakmor et al., 2016; Weinberger et al., 2020). AREPO is a massively parallel 3D magnetohydrodynamics code with gravity that inherits many advantages of the two popular schemes, Eulerian grid-based finite-volume codes and Lagrangian smoothed particle hydrodynamics (SPH). Although initially developed for cosmological simulations, AREPO has been successfully employed in phenomena involving stars, e.g., tidal disruptions and encounters (Goicovic et al., 2019; Ryu et al., 2023a,b, 2024b), TDEs in active galactic nuclei disks (Ryu et al., 2024c), collisions of main-sequence stars (Schneider et al., 2019), giant stars (Ryu et al., 2024a), white dwarfs (Pakmor et al., 2013, 2021, 2022; Burmester et al., 2023; Gronow et al., 2021; Glanz et al., 2023) and neutron stars (Lioutas et al., 2024), and common envelope evolution (Ohlmann et al., 2016b,a; Sand et al., 2020; Kramer et al., 2020; Ondratschek et al., 2022).

To solve the fluid equations, AREPO builds an unstructured Voronoi mesh with cells of

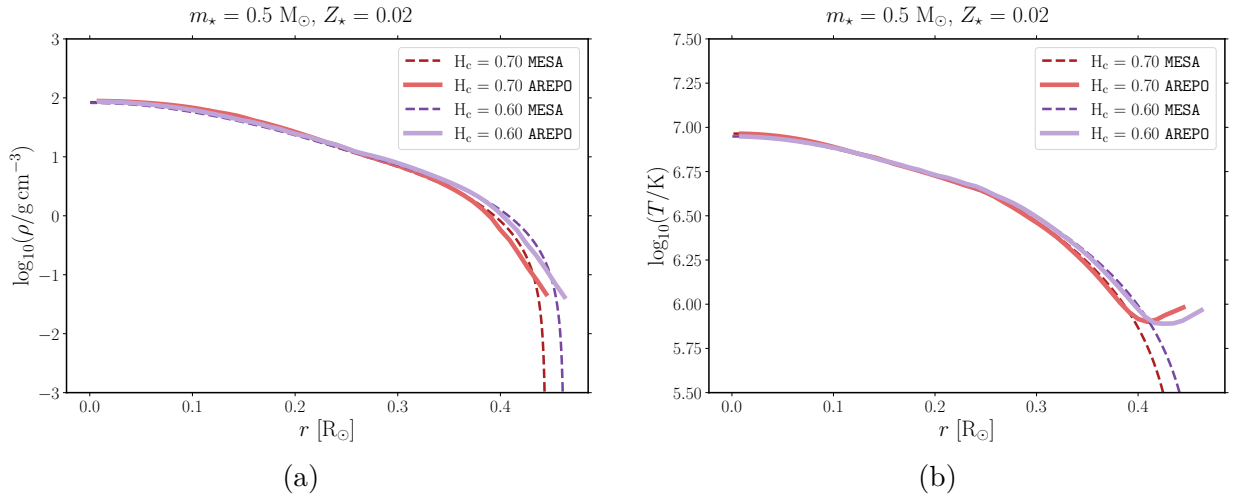


Figure 5.2: Similar profiles as Figure 5.1, but for a  $0.5 M_{\odot}$  MS star. A  $0.5 M_{\odot}$  star of age  $\sim 13.5$  Gyr with  $H_c = 0.60$  (purple curves) is very similar to a ZAMS star with  $H_c = 0.70$  (red curves), albeit with a slightly larger radius.

varying volume and calculates fluxes between the cells in a finite-volume approach. The Voronoi mesh moves in time according to the approximate bulk velocities of the fluid elements. Gravity is handled in a tree-particle-mesh scheme (see [Bagla, 2002](#)), with the minimum gravitational softening for the gas (star) cells set as one-tenth of the smallest gas cell for accuracy. AREPO allows for adaptation of spatial resolution according to arbitrary criteria on top of the default adaptivity to density, inherited from the near-Lagrangian nature of the scheme. It also includes particles that interact only gravitationally. We assume Newtonian gravity and do not include magnetic fields in our simulations.

### 5.2.2 Stellar models

We use the 1D stellar modeling code MESA ([Paxton et al., 2011](#)) to generate main-sequence (MS) stellar models with initial masses  $m_{\star} = 0.5 M_{\odot}$  and  $1.0 M_{\odot}$ , and metallicity  $Z_{\star} = 0.02$  (near-solar) at different ages. These masses are typical for globular clusters that predominantly consist of old, low-mass stars (e.g., [Salaris & Weiss, 2002](#); [De Angeli et al., 2005](#); [Marín-Franch et al., 2009](#)), while the metallicity is higher than those of most clusters, which typically have a tenth (or less) of Solar metallicity (e.g., [Harris, 2010](#)). However, the effect of metallicity is not expected to be significant and is quantified in Section 5.4. MESA solves the stellar structure equations to compute the evolution and provides us with stellar mass- and radial-profile parameters (e.g., densities, temperatures, and chemical abundances) at different evolutionary phases. We convert these 1D profiles to 3D AREPO initial conditions using the scheme adopted by [Ohlmann et al. \(2017\)](#), with the Helmholtz equation of state ([Timmes & Swesty, 2000](#)). After generating the star, we relax it for five stellar dynamical timescales  $t_{\text{dyn},\star} = (r_{\star}^3/Gm_{\star})^{0.5}$ , where  $r_{\star}$  is the stellar radius and  $G$  is the gravitational constant. We then use this relaxed star for the disruption simulations.

$m_\star$ [ $M_\odot$ ]	$t_\star$ [Gyr]	$H_c$	$r_\star$ [ $R_\odot$ ]	$t_{\text{dyn},\star}$ [hr]	$\rho_{\text{conc}}^{-1}$
0.5	0.01	0.70	0.44	0.19	0.46
	0.01	0.70	0.90	0.38	0.29
1.0	4.68	0.34	1.02	0.46	0.20
	8.60	0.00	1.22	0.60	0.12

Table 5.1: Parameters of the  $Z_\star = 0.02$  MS star models. The columns indicate stellar parameters - the mass  $m_\star$ , the age  $t_\star$ , the central hydrogen abundance  $H_c$ , the radius  $r_\star$ , the dynamical time  $t_{\text{dyn},\star}$  and the inverse of the density concentration parameter  $\rho_{\text{conc}}^{-1}$ .

Stellar density profiles are a major factor in determining whether a star undergoes a partial tidal disruption (PTDE) or a full tidal disruption (FTDE) for a given periapsis distance (e.g., [Ryu et al., 2020c](#)). To that end, we consider MESA models of three evolutionary stages of  $1.0 M_\odot$  MS stars with varying core hydrogen abundances  $H_c$ , which correspond to distinct density profiles (see also [Gallegos-Garcia et al., 2018](#); [Golightly et al., 2019](#); [Law-Smith et al., 2019](#); [Goicovic et al., 2019](#)). The first is close to the onset of hydrogen burning ( $H_c \approx 0.70$ ), i.e., zero-age main-sequence (hereafter ZAMS), the second is approximately midway through the main-sequence ( $H_c \approx 0.34$ ), i.e., middle-age main-sequence (hereafter MAMS), and the third is close to the depletion of core hydrogen ( $H_c \approx 0.00$ ), i.e., terminal-age main-sequence (hereafter TAMS). The total stellar mass remains nearly constant throughout the MS lifetime owing to the insignificant wind mass loss. In the case of the  $0.5 M_\odot$  stars, we examine only ZAMS profiles ( $H_c \approx 0.70$ ). This choice is motivated by the fact that their internal structure barely changes over time (see [Figure 5.2](#)) owing to their large MS lifetimes. One could choose a  $0.5 M_\odot$  star at an age comparable to a Hubble time (e.g., [Ryu et al., 2020a,c](#)) but the results are expected to be very similar. [Table 5.1](#) lists the stellar parameters of the MS star models for the stellar masses and ages we simulate.

Furthermore, we performed resolution scaling tests to ensure that the PTDE simulations were robust. To this end, we varied the number of fluid (star) cells making up a  $1 M_\odot$  star –  $5 \times 10^4$ ,  $8 \times 10^4$ ,  $2 \times 10^5$ ,  $5 \times 10^5$ , and  $8 \times 10^5$ . We then performed PTDE simulations involving a  $1 M_\odot$  star and a  $10 M_\odot$  BH for each resolution. The masses lost due to tidal disruption plateaued close to the resolutions  $2 \times 10^5$  and  $5 \times 10^5$ , with the mass loss values using  $5 \times 10^5$  and  $8 \times 10^5$  cells being essentially the same. Hence, we chose an initial resolution of  $5 \times 10^5$  fluid cells for the stars in this study. It should be noted that the number of cells increases as the simulations progress since AREPO automatically adds extra cells when the density gradient is high.

[Figure 5.1](#) shows that more evolved  $1 M_\odot$  MS stars have a denser (left panel) and hotter (right panel) core and a puffer outer layer than less evolved MS stars. Since the three stars have different radii  $r_\star$ , they also have different  $t_{\text{dyn},\star}$  and different tidal radii  $r_t = (m_{\text{BH}}/m_\star)^{1/3} r_\star$  for the same BH mass  $m_{\text{BH}}$ . [Figure 5.2](#) shows that  $0.5 M_\odot$  stars of different ages – ZAMS ( $H_c = 0.70$ ) and  $\sim 13.5$  Gyr ( $H_c = 0.60$ ) – have very similar density

$m_\star$ [ $M_\odot$ ]	$m_{\text{BH}}$ [ $M_\odot$ ]	$H_c$	$b = r_p/r_t$
0.5	10.0, 40.0	0.70	0.25, 0.33, 0.50, 0.75, 1.00, 1.50, 2.00, 2.50
1.0	10.0, 40.0	0.70, 0.34, 0.00	0.25, 0.33, 0.50, 0.75, 1.00, 1.50, 2.00

Table 5.2: Initial parameters of our suite of simulations. The columns indicate the initial parameters - the stellar mass  $m_\star$ , the BH mass  $m_{\text{BH}}$ , the core hydrogen fraction  $H_c$ , and the impact parameter  $b$ . In each row, every comma-separated combination of values in all columns is simulated, to give a total of 58 simulations.

and temperature profiles, which justifies excluding the latter from our simulation runs. It should be noted that the **AREPO** profiles, especially the temperature, diverge significantly from the **MESA** ones near the surface of the star (corresponding to a fractional mass of  $\sim 10^{-4}$ – $10^{-3}$ ). This amount of mass near the surface that deviates from the **MESA** model sets the minimum amount of stripped mass in PTDEs that we can resolve. Therefore, we only present the results of PTDEs yielding a mass loss  $\gtrsim 10^{-4}m_\star$  in this paper.

### 5.2.3 Black hole

The black holes are initialized in **AREPO** as non-rotating sink particles that interact gravitationally and grow in mass through accretion. We set the gravitational softening length of the BH to be ten times the minimum softening length of the gas (star) cells. The scheme we use for accretion onto the BH, described here briefly, is the same as the one used in [Ryu et al. \(2022, 2023a,b, 2024b\)](#). Firstly, the cells around the BH within a radius of  $10^4 r_g$ , where gravitational radius  $r_g = Gm_{\text{BH}}/c^2$ , are identified. Secondly, the accretion onto the BH is calculated using a weighted average of radial flux to account for the higher contribution of gas closer to the BH and vice-versa. Thirdly, mass is extracted from the neighboring cells of the BH, and momentum is inserted in the BH to conserve these quantities. Finally, the BH is spun up from accretion by adding angular momentum from the selected neighboring cells. The radiation feedback from accretion is not taken into account. Although angular momentum is conserved through this scheme, there is no guarantee that the total energy is conserved. However, given that accretion onto the black hole is small in our simulations, the energy lost due to accretion is negligible.

We run simulations with SBH masses of  $10 M_\odot$  and  $40 M_\odot$ , which are in proximity to the lower- and higher-mass peaks of observed LIGO BH masses (e.g., [Abbott et al., 2021b, 2023](#)). Given the mass of the BH  $m_{\text{BH}}$ , the mass of the star  $m_\star$ , and the radius of the star  $r_\star$ , the classical tidal radius is defined as  $r_t = (m_{\text{BH}}/m_\star)^{1/3}r_\star$ .

### 5.2.4 Initial conditions

The distance of the closest approach is characterized by the impact parameter:  $b \equiv r_p/r_t$ <sup>1</sup>, where  $r_p$  is the periapsis distance of the initially parabolic orbit. We vary the mass of the star:  $0.5 M_\odot$  and  $1 M_\odot$ , and the mass of the black hole:  $10 M_\odot$  and  $40 M_\odot$ . We then generate a suite of simulations of  $b$  varying from 0.25 to 2.00 ( $1 M_\odot$  stars) or 2.50 ( $0.5 M_\odot$  stars), and the three stellar ages (density profiles) to determine the post-disruption orbital, mass and spin parameter. The additional simulations for  $0.5 M_\odot$  and  $b = 2.50$  are performed to properly analyze the PTDE trends since  $0.5 M_\odot$  stars are fully disrupted for  $b \lesssim 1.00$ .

We also assume that the initial stars are non-rotating and that the star-BH encounters are parabolic. This can be justified for encounters in globular clusters because the velocity dispersions of Milky Way globular clusters are in the range  $\sim 1\text{--}20 \text{ km s}^{-1}$  (e.g., [Baumgardt & Hilker, 2018](#)). For instance, given a velocity dispersion  $\sigma \simeq 10 \text{ km s}^{-1}$ ,  $|1 - e| \simeq 10^{-4}$  (very close to parabolic) for the parameters considered in this paper.

Each simulation is run for  $\sim 70 t_{\text{dyn},\star}$  after periapsis passage. This duration was chosen to ensure that the stellar masses reach steady values for proper analysis. Table 5.2 provides an overview of the parameters we use in our suite of simulations.

## 5.3 Analysis

### 5.3.1 Calculation of bound and unbound mass

To find the center of mass of a self-bound object (i.e., star before disruption, remnant after disruption) in each snapshot, we used an iterative procedure fairly similar to [Guillochon & Ramirez-Ruiz \(2013\)](#), with some differences to improve the accuracy of the identification of bound and unbound cells. For each snapshot, we chose the gas cell with the maximum density as the ‘initial’ guess for the center of mass (CoM) position. Subsequently, we calculate the specific total energies of all the star cells relative to the star CoM,  $\varepsilon_{\text{cell,CoM}}$ , and the BH,  $\varepsilon_{\text{cell,BH}}$ , as the sum of their relative kinetic, potential and internal energies. We consider a cell to be bound to a self-gravitating object if  $\varepsilon_{\text{cell,CoM}} < 0$ ,  $\varepsilon_{\text{cell,CoM}} < \varepsilon_{\text{cell,BH}}$ . The last condition ensures that the cells bound to the star are ‘close’ to the CoM. We compute a ‘new’ CoM position (and velocity) using these bound cells and determine the ‘new’ specific energy. We iterate this process until there is no change in the relative position of the CoM. Subsequently, we calculate its ‘final’ bound mass. In the case of an FTDE, we also visually inspect the surface density plots and assign the mass bound to the star to be zero.

The mass bound to the BH is calculated in a similar fashion, though the position of the BH is trivially known from the simulation. Finally, we consider any cells with  $\varepsilon_{\text{cell,CoM}} \geq 0$  and  $\varepsilon_{\text{cell,CoM}} \geq 0$  unbound from the system.

---

<sup>1</sup> $\beta \equiv b^{-1}$  is often introduced in the literature for TDEs by SMBHs as the ‘penetration factor’.

### 5.3.2 Calculation of orbital and spin parameters

For each snapshot post-disruption, we compute the instantaneous Keplerian orbital parameters – the semimajor axis  $a$  and orbital eccentricity  $e$  – using the current values of the mass bound to the star  $m_\star$ , the mass of the BH (plus the gas mass bound to it)  $m_{\text{BH}}$ , the positions and velocities of the star’s CoM ( $\mathbf{r}_{\text{CoM}}, \mathbf{v}_{\text{CoM}}$ ) and the BH ( $\mathbf{r}_{\text{BH}}, \mathbf{v}_{\text{BH}}$ ). For completeness, with  $\mathbf{r} \equiv \mathbf{r}_{\text{CoM}} - \mathbf{r}_{\text{BH}}$  and  $\mathbf{v} \equiv \mathbf{v}_{\text{CoM}} - \mathbf{v}_{\text{BH}}$ , the equations are as follows:

$$a = \left( \frac{2}{r} - \frac{v^2}{G(m_\star + m_{\text{BH}})} \right)^{-1} \quad (5.1)$$

$$e = \left( 1 - \frac{(\mathbf{r} \times \mathbf{v})^2}{G(m_\star + m_{\text{BH}})a} \right)^{0.5} \quad (5.2)$$

We determine the spin angular momentum  $\mathbf{L}_\star$  about the star’s CoM using the masses  $m_i$ , relative positions  $\mathbf{r}_i$  and velocities  $\mathbf{v}_i$  of the bound gas cells. In the cases of full disruption, we ignore the orbital and spin parameters.

The ‘final’ post-disruption mass, orbital, and spin parameters reported in the following section are the means and standard deviations of these quantities during the last ten snapshots of each simulation (the time between consecutive snapshots was chosen to be approximately equal to the initial dynamical timescale of the star). In the cases where a partially disrupted star returns on a second passage within the simulation time, we chose snapshots close to the apoapsis of the first passage for the parameter calculations.

## 5.4 Results

Figure 5.3 shows selected snapshots of our suite of simulations. It can be visually seen that the final outcomes (FTDE or PTDE) depend on all the parameters that we considered – the stellar mass  $m_\star$ , the core hydrogen fraction  $H_c$ , the BH mass  $m_{\text{BH}}$ , and the impact parameter  $b$ .

The following sections detail the quantitative results. It should be noted that, henceforth, initial star parameters are given the subscript  $\star$  (e.g.  $m_\star, L_\star$ ), while the post-disruption remnant parameters are given the subscript  $\diamond$  (e.g.  $m_\diamond, L_\diamond$ ). Table 6.1 provides detailed initial and post-disruption parameters for our 58 simulations.

### 5.4.1 Effect of density concentration factor

Ryu et al. (2020b) showed that, in the case of SMBHs, the critical impact parameter for full disruption,  $b_{\text{FTDE}}$ , is inversely proportional to the density concentration factor  $\rho_{\text{conc}} \equiv (\rho_c/\bar{\rho})^{1/3}$ , where  $\bar{\rho}$  and  $\rho_c$  are average and central stellar density respectively (see also Law-Smith et al., 2020). A larger value of  $\rho_{\text{conc}}$  represents a denser core with a puffier outer layer, and vice-versa. This indicates that a star with higher core density requires a smaller impact parameter to fully disrupt. Quantitatively,  $b_{\text{FTDE}}$  can be written as:

$$b_{\text{FTDE}} = \rho_{\text{conc}}^{-1} \tilde{b}_{\text{FTDE}} \quad (5.3)$$



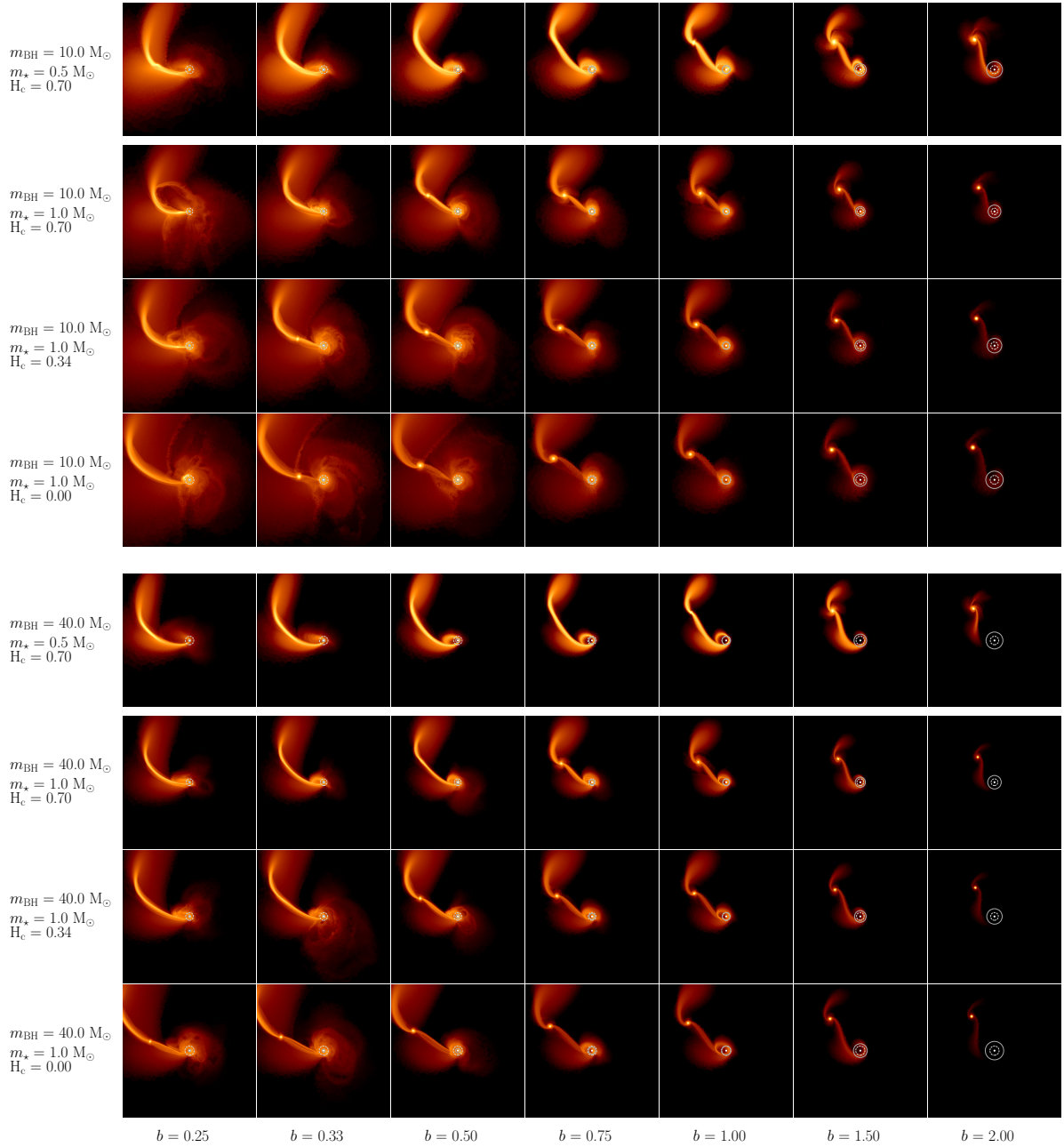


Figure 5.3: Grid of log density slices of stars  $\sim 20 t_{\text{dyn},\star}$  after undergoing  $\mu$ TDEs, with the BH at the center of each panel. Each row is for a different  $m_{\text{BH}}$  (top and bottom half for  $10 M_{\odot}$  and  $40 M_{\odot}$  respectively),  $m_{\star}$  or  $H_c$ , whereas the columns represent increasing  $b$  (from left to right). The dashed and solid circles around the BH, most visible in the rightmost panels, denote the tidal radius,  $r_t$ , and the periaapsis distance,  $r_p$ , respectively. Note that the spatial range of each panel is not the same.

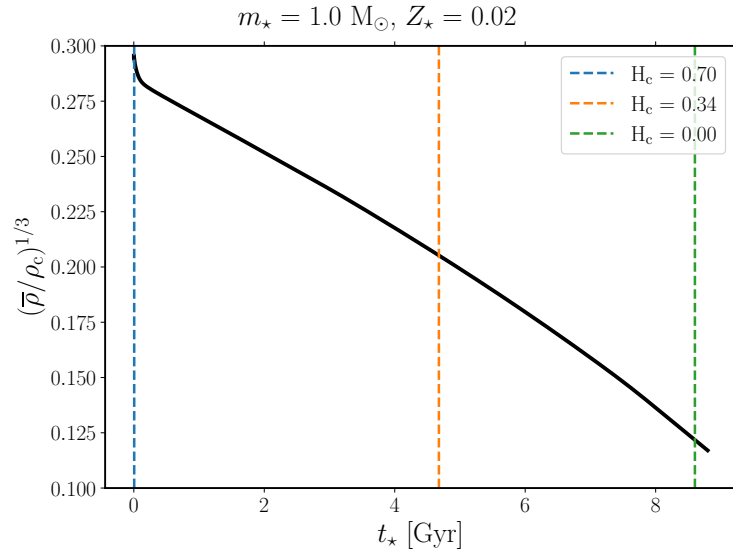


Figure 5.4: MESA-derived inverses of density concentration factors  $\rho_{\text{conc}}^{-1}$  for a  $1 M_{\odot}$  MS star as a function of stellar age. The three dashed vertical lines represent the ages of three chosen MS models in our study, corresponding to the profiles in Figure 5.1 and the values in Table 5.1. The dependence with age is very close to linear.

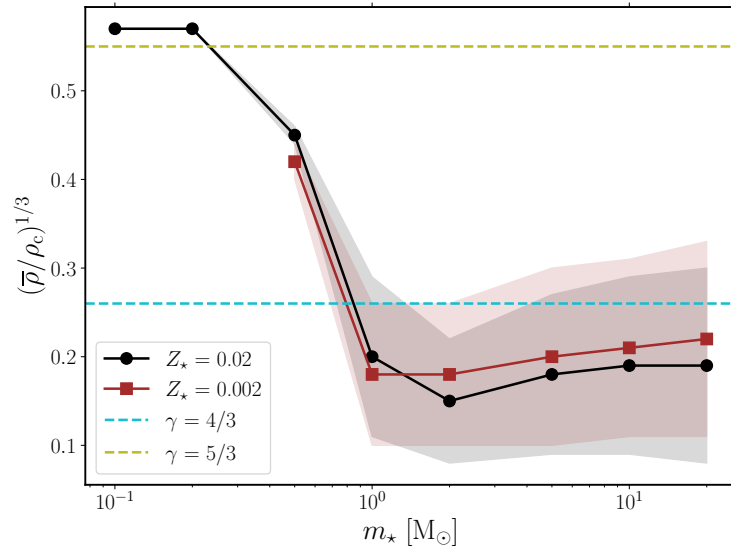


Figure 5.5: MESA-derived inverses of density mean concentration factors  $\rho_{\text{conc}}^{-1}$  for MS stars of a range of masses (0.1, 0.2, 0.5, 1.0, 2.0, 5.0, 10.0 and 20.0 in units of  $M_{\odot}$ ) and two metallicities – 0.02 and 0.002. The shaded regions illustrate the variation in  $\rho_{\text{conc}}^{-1}$  over the MS lifetime, with a TAMS star having the lowest  $\rho_{\text{conc}}^{-1}$  value and a ZAMS star having the highest (the values are for ZAMS stars only in the cases of stars of masses  $< 1 M_{\odot}$ ). The two dashed horizontal lines represent the corresponding values for polytropic stars, shown in Table 5.3.

$\gamma$	$b_{\text{FTDE}}$	$\rho_{\text{conc}}^{-1}$	$\tilde{b}_{\text{FTDE}}$
4/3	0.50	0.26	1.92
5/3	1.08	0.55	1.96

Table 5.3: Evaluated values of the impact parameter for the full disruption of a star with uniform density,  $\tilde{b}_{\text{FTDE}} = b_{\text{FTDE}}/\rho_{\text{conc}}$ , for polytropic stars using [Mainetti et al. \(2017\)](#). The columns indicate the polytropic index  $\gamma$ , the impact parameter for full disruption  $b_{\text{FTDE}}$ , the inverse of the density concentration factor  $\rho_{\text{conc}}^{-1}$  and the aforementioned parameter  $\tilde{b}_{\text{FTDE}}$ .

Here,  $\tilde{b}_{\text{FTDE}}$  is the critical impact parameter for the full disruption of a hypothetical star with uniform density, i.e.,  $\rho_{\text{conc}} = 1$  (see also Equation 15 of [Ryu et al., 2020b](#)). Table 5.3 displays the values of  $b_{\text{FTDE}}$  of stars with polytropic indices  $\gamma$  (where  $P \propto \rho^\gamma$ ) 4/3 and 5/3 as calculated by [Mainetti et al. \(2017\)](#). Shown also are the analytically computed  $\rho_{\text{conc}}$  for these polytropes, and the subsequently evaluated (using Equation 5.3)  $\tilde{b}_{\text{FTDE}}$  values. We also estimate  $\tilde{b}_{\text{FTDE}}$  to be  $1.95 \pm 0.20$  from our suite of simulations by fitting the remnant masses for given initial stellar and BH masses (see the following section for details), and find the values of  $b_{\text{FTDE}}$ . Despite the significant difference in the masses of the black holes, our estimated values agree with those from [Mainetti et al. \(2017\)](#). Estimates of this factor calculated by [Ryu et al. \(2020b\)](#), [Law-Smith et al., 2020](#) and [Kiroğlu et al. \(2023\)](#) all lie within the error range. Since the former two studies are on SMBHs and the latter is on IMBHs, we reiterate that  $\tilde{b}_{\text{FTDE}}$  is almost independent of the mass of the BH for a very large range of BH masses. The consensus between the previous works in spite of different numerical schemes (general relativistic grid-based hydrodynamics, adaptive-mesh refinement, and SPH respectively) and the current work strengthens this point. Therefore, we will use our computed value of  $\tilde{b}_{\text{FTDE}} = 1.95 \pm 0.20$  for the fit functions in the following sections.

For completeness, Figure 5.4 (and Table 5.1) shows the trend  $\rho_{\text{conc}}^{-1}$  for MESA  $1 M_\odot$  MS stars, with our three stellar models highlighted. We see that a more evolved star has a smaller  $\rho_{\text{conc}}^{-1}$  (harder to fully disrupt) compared to a less evolved star (easier to fully disrupt) and that this relation is close to linear as a function of stellar age  $t_\star$ . Figure 5.5 shows the averaged  $\rho_{\text{conc}}^{-1}$  values for a range of masses of MESA-generated MS stars ( $0.1 M_\odot - 20.0 M_\odot$ ) of two metallicities – 0.02 (near-Solar) and 0.002 (sub-Solar). We see that higher mass MS stars have denser cores and puffier outer layers (hence lower  $\rho_{\text{conc}}^{-1}$  values, which plateau for stars of masses  $\gtrsim 1 M_\odot$  at  $\sim 1.6-2.0$ ), while the opposite is true for lower mass MS stars. Moreover, metallicity affects  $\rho_{\text{conc}}^{-1}$  only slightly, with the metal-poor stars being slightly less (more) centrally concentrated when  $m_\star > 1.0 M_\odot$  ( $m_\star \leq 1.0 M_\odot$ ). The (approximate) values of  $\rho_{\text{conc}}^{-1}$  are crucial to applying our fits (see the following sections).

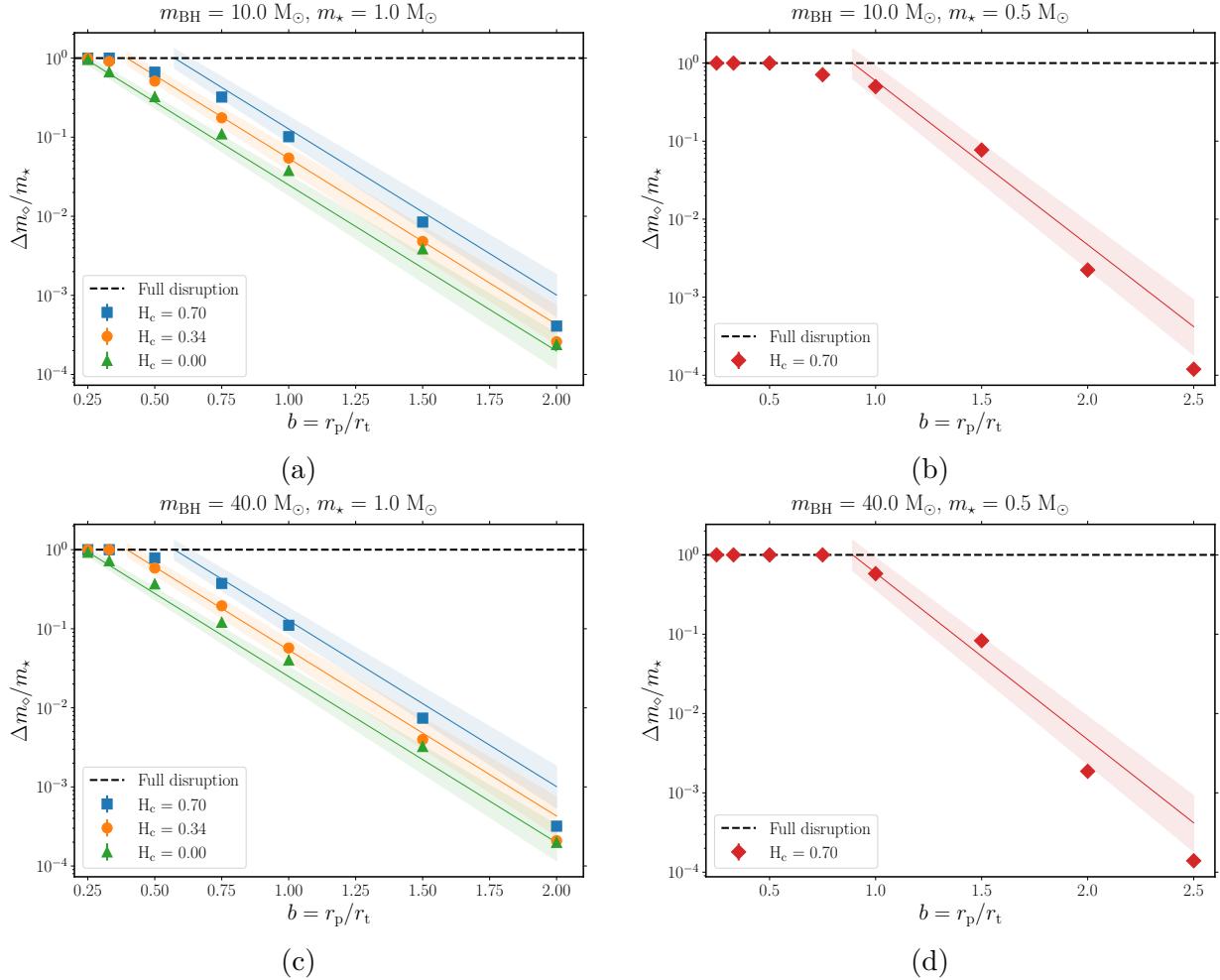


Figure 5.6: Post-disruption fractional mass loss,  $\Delta m_{\odot}/m_{\star}$ , for a star of mass  $1 M_{\odot}$  (left) and  $0.5 M_{\odot}$  (right), due to a BH of mass  $10 M_{\odot}$  (top) and  $40 M_{\odot}$  (bottom), as a function of impact parameter  $b$  and MS age ( $H_c$  abundance). The dashed line at the top signifies the full disruption of the star. The fractional mass losses are largely independent of BH mass. Mass loss is higher for lower  $b$  values, and this decreases roughly exponentially (best-fit lines and standard error regions shown) with increasing  $b$ . A less evolved star (higher  $H_c$ ) loses more mass for the same value of  $b$ . A  $0.5 M_{\odot}$  star has a higher mass loss than a  $1 M_{\odot}$  star for the same  $b$ .

### 5.4.2 Post-disruption stellar and BH masses

After a disruption event, a star loses mass, some of which gets bound to (and eventually accreted onto) the BH while the rest of it becomes unbound from the system. Evidently, the closer the approach of the star is to the BH, the larger the mass lost from the star.

Figure 5.6 shows this trend for the case of a  $1 M_{\odot}$  (left) and a  $0.5 M_{\odot}$  (right) star that is disrupted by a  $10 M_{\odot}$  (top) and a  $40 M_{\odot}$  (bottom) BH. The post-disruption fractional mass loss  $\Delta m_{\diamond}/m_{\star}$ , where  $\Delta m_{\star}$  is the difference between the star's initial mass  $m_{\star}$  and the remnant mass  $m_{\diamond}$ . It decreases almost exponentially with the impact parameter  $b$ . Moreover, a more evolved MS star loses less mass compared to a less evolved star for the same value of  $b$ . This is because a more evolved star, with a higher central concentration, requires a stronger tidal force (or smaller  $b$ ) to strip the same amount of mass when compared to a less evolved star. Consequently,  $b_{\text{FTDE}}$ , corresponding to  $\Delta m_{\diamond}/m_{\star} = 1$ , is also lower for more evolved stars.

Furthermore, we see that roughly half the mass lost from the star stays bound to the BH, although this is not always true, especially when there is little mass loss (see Table 6.1). This bound mass decreases through time due to continuous debris interaction resulting in mass unbinding, and hence is an upper limit for the mass that can be accreted onto the BH. Details of the accretion process and feedback from the BH might prevent some of the mass bound to the BH from being accreted, but following this process is beyond the scope of our paper. The other half of the stripped mass is unbound from the BH-star system.

We can fit (with standard  $1\sigma$  errors) the fractional mass loss  $\Delta m_{\star}$  well by:

$$\log_{10} \left( \frac{\Delta m_{\diamond}}{m_{\star}} \right) = \min \{ (-2.10 \pm 0.10) (b - b_{\text{FTDE}}), 0 \} \quad (5.4)$$

Here,  $b_{\text{FTDE}}$  is as given in Equation 5.3. Since  $\rho_{\text{conc}}$  is taken into account, this fit differs from those obtained by Guillochon & Ramirez-Ruiz (2013) and Ryu et al. (2020c) for TDEs due to SMBHs. The remnant mass fit function does not explicitly depend on  $m_{\star}$  and  $m_{\text{BH}}$ , but only on  $b$  and  $\rho_{\text{conc}}$ . Since  $\rho_{\text{conc}}$  is higher for more evolved stars, they have a smaller  $b_{\text{FTDE}}$  and hence, less fractional mass loss. Figure 5.6 plots these best-fit curves, with the error bars shaded. It should be noted that this trend may not hold for larger values of  $b$ .

### 5.4.3 Post-disruption stellar spins

An initially non-rotating star gains spin after a tidal encounter due to tidal torques from the BH. Although we do not delve into the details of the spin-up, this results in *differential*, and not rigid, rotation of the star. It should be noted that, due to spurious motions in our initial AREPO stellar models, the spin angular momenta  $L_{\star}$  are not zero but  $\sim 1-2 \times 10^{47} \text{ g cm}^2 \text{ s}^{-1}$  ( $\sim 2 \times 10^{46} \text{ g cm}^2 \text{ s}^{-1}$ ) for  $1 M_{\odot}$  ( $0.5 M_{\odot}$ ) stars. Since these values correspond to negligible equatorial surface velocities<sup>2</sup> of  $\sim 10 \text{ m s}^{-1}$ , the stars are considered to be non-rotating. The spin angular momentum of the remnant  $L_{\diamond}$  depends on the internal structure of the original star and the impact parameter.

<sup>2</sup>In contrast, the Sun, a very slow rotator, has an equatorial surface velocity of  $\sim 2 \text{ km s}^{-1}$ .

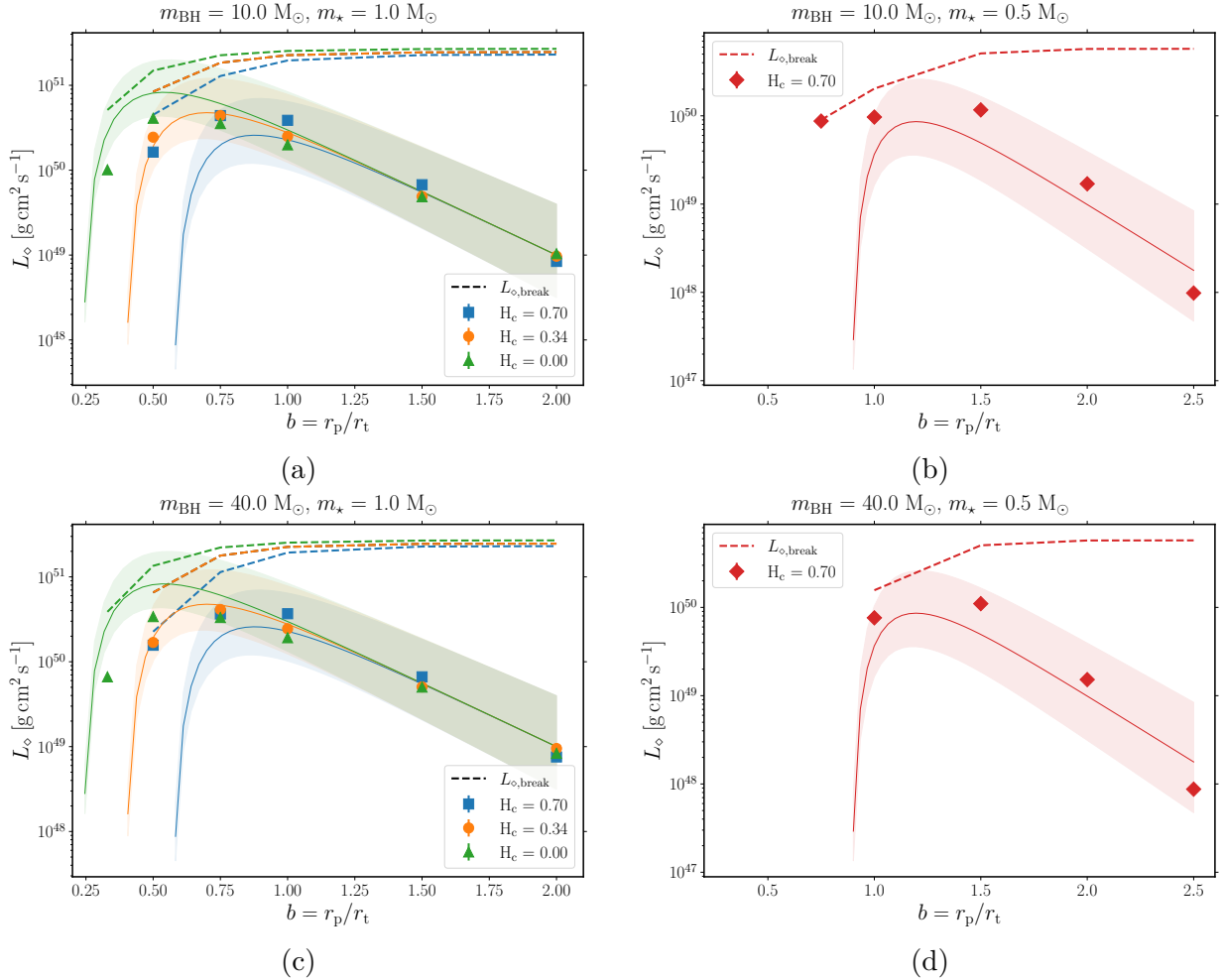


Figure 5.7: Post-disruption spin angular momentum,  $L_{\odot}$ , for an initially non-rotating star of mass  $1 M_{\odot}$  (left) and  $0.5 M_{\odot}$  (right), due to a BH of mass  $10 M_{\odot}$  (top) and  $40 M_{\odot}$  (bottom), as a function of impact parameter  $b$  and MS age ( $H_c$  abundance). The dashed lines indicate the (approximate) estimated break-up angular momenta of the remnants  $L_{\odot, \text{break}}$  respectively. The spin angular momenta are largely independent of BH mass. It decreases almost exponentially for sufficiently high  $b$  values, and it drops for very low  $b$  values when the remnant mass is small (best-fit lines and standard error regions shown). The drop-off of angular momentum occurs at larger  $b$  for a less evolved star.

Figure 5.7 shows the trend of  $L_\diamond$  with respect to the impact parameter  $b$  for the case of a  $1 M_\odot$  (left) and a  $0.5 M_\odot$  (right) star being *partially* disrupted by a  $10 M_\odot$  (top) and a  $40 M_\odot$  (bottom) BH. In addition, we indicate the approximate, order-of-magnitude estimates of the break-up angular momenta (assuming uniform density and rigid rotation) of the remnant stars,  $L_{\diamond,\text{break}} = 0.4 m_\diamond r_\diamond v_{\diamond,\text{break}}$ <sup>3</sup>. Here, we crudely estimate the remnant radius as  $(r_\diamond/R_\odot) = (m_\diamond/M_\odot)^{0.7}$  and assume the break-up velocity to be the Keplerian velocity at  $r_\star$ , i.e.,  $v_{\diamond,\text{break}} = \sqrt{Gm_\diamond/r_\diamond}$ . In reality, the remnant is significantly puffed up, and the break-up velocity would depend on the true moment of inertia of the remnant (and thus, its density profile) and the differential rotation due to spin-up. For our range of simulation parameters,  $L_\diamond$  remains below  $L_{\diamond,\text{break}}$ , although significant mass loss can bring the remnant very close to break-up, e.g.,  $m_\star = 0.5 M_\odot$  and  $b \lesssim 1.00$ . For higher values of  $b$  (but still less than  $b \sim 2$ ),  $L_\diamond$  decreases almost exponentially as  $b$  increases. On the other hand, when  $b$  is less such that a fractional mass loss is  $\geq 2 \times 10^{-1}$ , the trend reverses until FTDE. This trend reflects the counter-balance between mass loss and spin-up: for stronger PTDEs, although the remnant is spun up more rapidly, the remnant mass is smaller.

The large spin-up for smaller  $b$  indicates that the specific angular momentum monotonically increases as  $b$  decreases. Motivated by this, we considered the *scaled* (moment of inertia-adjusted) parameter  $L_{\diamond,\text{scaled}} \equiv L_\diamond / (m_{\diamond,\text{frac}} \tilde{r}_{\diamond,\text{frac}}^2)$ . Here, the fractional remnant mass  $m_{\diamond,\text{frac}} \equiv m_\diamond / m_\star$  and the post-disruption estimated fractional radius  $\tilde{r}_{\diamond,\text{frac}} / R_\odot = m_{\diamond,\text{frac}}^{0.7}$  is a crude estimate of the radius of an MS star.

We found the following exponential fit (with standard  $1\sigma$  errors) describes  $L_{\diamond,\text{scaled}}$  well:

$$\log_{10} \left( \frac{L_{\diamond,\text{scaled}}}{\text{g cm}^2 \text{ s}^{-1}} \right) = (-1.50 \pm 0.15) b + (52.00 \pm 0.30) \quad (5.5)$$

From the definition of  $\tilde{r}_{\star,\text{frac}}$  before, we have:

$$L_\diamond = L_{\diamond,\text{scaled}} \left( \frac{m_\diamond}{m_\star} \right)^{2.4} = L_{\diamond,\text{scaled}} \left( 1 - \frac{\Delta m_\diamond}{m_\star} \right)^{2.4} \quad (5.6)$$

Here,  $(\Delta m_\diamond / m_\star)$  is estimated using Equation 5.4. This equation implies that the post-disruption spin depends significantly on the fractional mass loss. Moreover, there is no dependence on  $m_{\text{BH}}$ . Figure 5.7 plots these best-fit curves, with the error bars shaded.

#### 5.4.4 Post-disruption orbital parameters

Depending on the stellar structure and the BH mass, a star in an initially parabolic orbit ends up in an eccentric or even a hyperbolic orbit after a PTDE (see also Ryu et al., 2020c; Kremer et al., 2022; Kiroğlu et al., 2023). The specific orbital energy of the star-BH system,  $\varepsilon_{\text{orb}}$ , is the sum of the specific energy injected into stellar tides,  $\varepsilon_{\text{tide}}$ , the specific binding energy of the ejected material,  $\varepsilon_{\text{bind}}$ , and the specific ‘kick’ energy,  $\varepsilon_{\text{kick}}$  (see Kremer et al.,

<sup>3</sup>This is because hypothetical star (sphere) of uniform density has a moment of inertia of  $I_{\star,\text{uniform}} = 0.4 m_\star r_\star^2$  about an axis of rotation passing through the center.

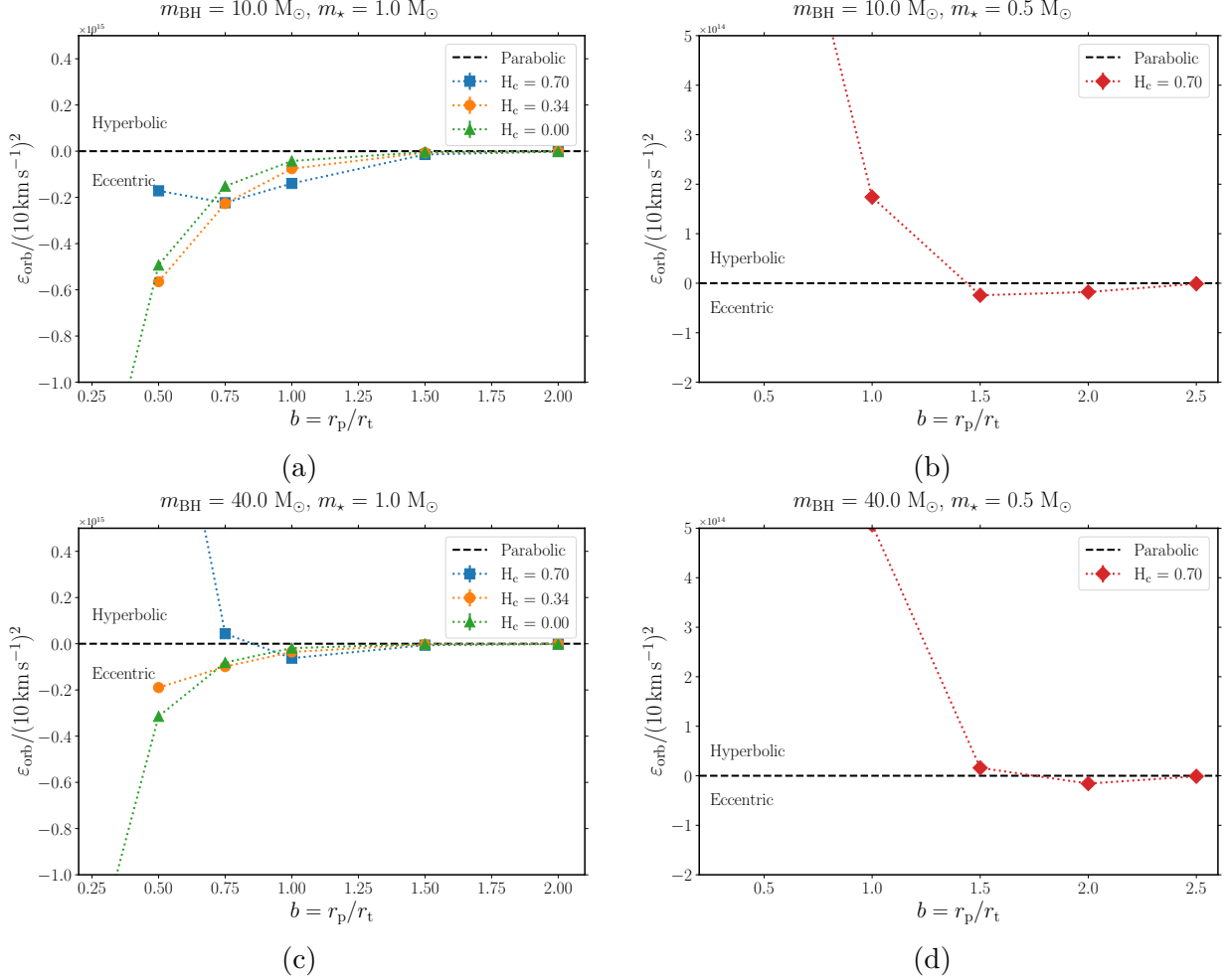


Figure 5.8: Post-disruption normalized specific orbital energy of the star-BH system,  $\varepsilon_{\text{orb}}$ , for a star of mass  $1 M_{\odot}$  (left) and  $0.5 M_{\odot}$  (right) initially in a parabolic orbit, due to a BH of mass  $10 M_{\odot}$  (top) and  $40 M_{\odot}$  (bottom), as a function of impact parameter  $b$  and MS age ( $H_c$  abundance). The dashed line represents parabolic orbits and separates the parameter space into bound (eccentric) and unbound (hyperbolic) orbits. When mass loss is relatively low, a lower value of  $b$  generally results in more negative  $\varepsilon_{\text{orb}}$  in the case of  $1 M_{\odot}$  star. This trend continues for the TAMS star. However, for the ZAMS and MAMS stars, significant mass losses can reverse this trend, with hyperbolic orbits also being a possibility (e.g.,  $1 M_{\odot}$  ZAMS star and  $40 M_{\odot}$  BH mass with  $b < 1.00$ ).  $0.5 M_{\odot}$  stars, on the other hand, can become unbound for larger  $b$ , with boundedness also depending on the mass of the BH.



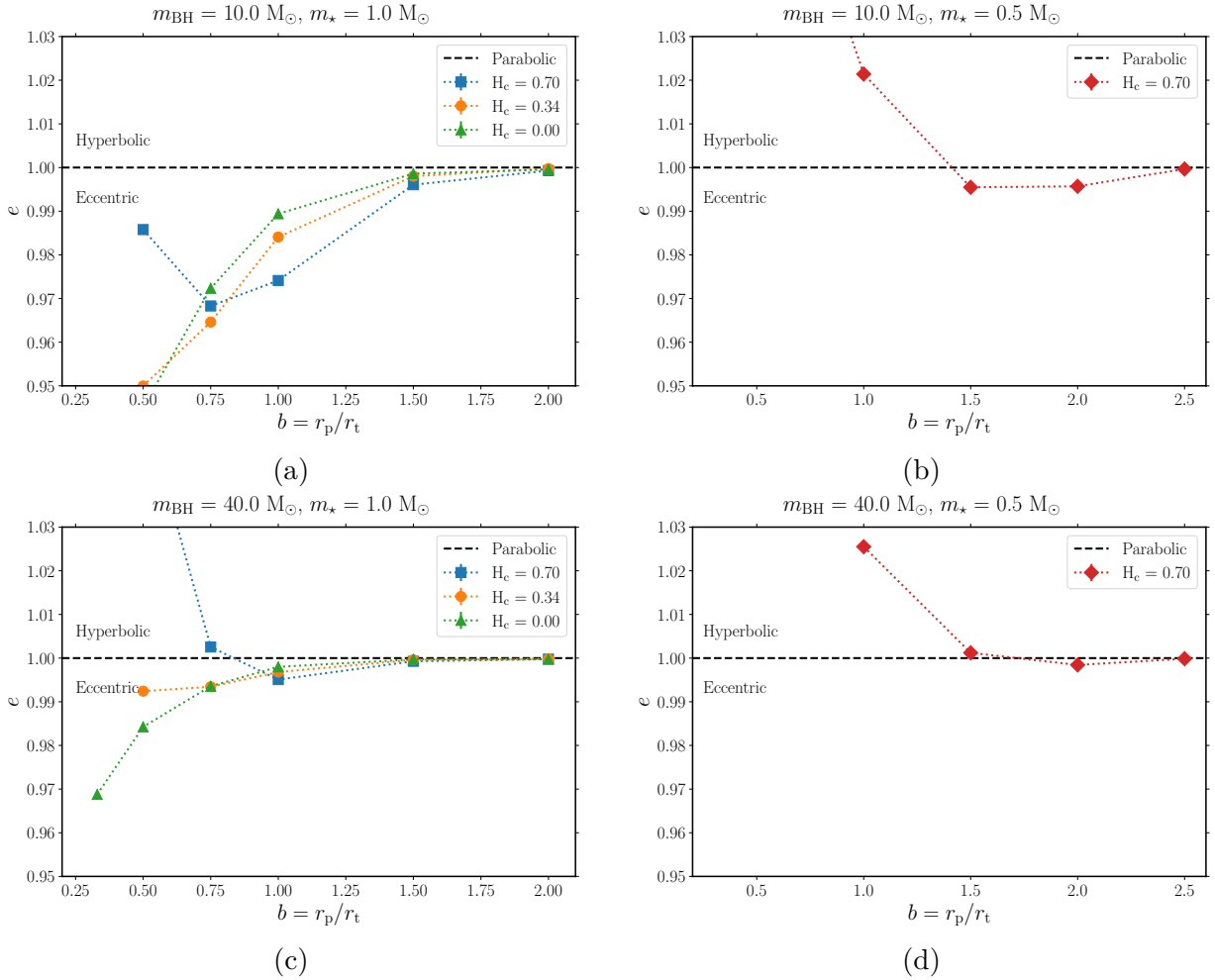


Figure 5.9: Post-disruption orbital eccentricity,  $e$ , for a star of mass  $1 M_{\odot}$  (left) and  $0.5 M_{\odot}$  (right) initially in a parabolic orbit, due to a BH of mass  $10 M_{\odot}$  (top) and  $40 M_{\odot}$  (bottom), as a function of impact parameter  $b$  and MS age ( $H_c$  abundance). The dashed line represents parabolic orbits and separates the parameter space into bound (eccentric) and unbound (hyperbolic) orbits. The reasoning for the trends is the same as that for Figure 5.8.

2022). Manukian et al. (2013) estimated the potentially unbinding ‘kick’ received by a star undergoing PTDE due to an SMBH from asymmetric mass loss and observed that it depends solely on the mass loss and not on the star-SMBH mass ratio. However, this is not true for  $\mu$ TDEs – the mass ratio determines the kick, and hence the boundedness, of the star-SBH system (see also Figure 2 of Kiroğlu et al., 2023 for TDEs due to IMBHs).

Figure 5.8 shows the post-disruption specific orbital energy of the star-BH system,  $\varepsilon_{\text{orb}}$ , for the disruption of a  $1 M_{\odot}$  and a  $0.5 M_{\odot}$  star by a  $10 M_{\odot}$  (top panel) and a  $40 M_{\odot}$  (bottom panel) BH. The values are normalized to the square of  $\sigma = 10 \text{ km s}^{-1}$ , the typical velocity dispersion of Milky Way globular clusters (e.g., Baumgardt & Hilker, 2018). More negative (positive) values represent more bound (unbound) orbits. In general,  $\varepsilon_{\text{orb}}$  becomes more

negative with decreasing  $b$ . If the density concentration factor  $\rho_{\text{conc}}$  is high enough (as in the case of a TAMS  $1 M_{\odot}$  star; see Figure 5.4), this trend continues till FTDE. However, in the case of a ZAMS  $1 M_{\odot}$  star (and less extremely in a MAMS star), there is a certain value of  $b$  at which  $\varepsilon_{\text{orb}}$  starts to increase with decreasing  $b$ . This is due to the momentum kick from asymmetric mass loss, which becomes significant when the mass loss is high. In the case of a PTDE of a  $1 M_{\odot}$  ZAMS star by a  $40 M_{\odot}$  BH, the post-disruption orbit can be hyperbolic (unbound) for  $b$  values close to FTDE. This trend is more extreme for a  $0.5 M_{\odot}$  star, with hyperbolic orbits being possible even in the case of PTDE by a  $10 M_{\odot}$  BH. Moreover, their velocities at infinity are high enough ( $\sim 100\text{--}300 \text{ km s}^{-1}$ ) to escape the cluster entirely. The two different BH masses result in quite different quantitative orbital parameters. Similar to Kremer et al., 2022, we can write each of the energy components as follows:

$$\varepsilon_{\text{tide}} = -\frac{Gm_{\text{BH}}^2}{r_{\star}m_{\diamond}} \left[ \left(\frac{r_{\star}}{r_{\text{p}}}\right)^6 T_2 + \left(\frac{r_{\star}}{r_{\text{p}}}\right)^8 T_3 \right] \quad (5.7)$$

$$\varepsilon_{\text{bind}} = -\frac{G\Delta m_{\diamond}}{2r_{\star}} \quad (5.8)$$

$$\varepsilon_{\text{kick}} = \frac{Gm_{\text{BH}}\Delta m_{\diamond}r_{\star}^2}{r_{\text{p}}^3m_{\diamond}} \quad (5.9)$$

Here,  $T_2$  and  $T_3$  are terms which depend on the stellar mass, radius, and density structure, BH mass, and distance of approach (Press & Teukolsky, 1977; Lee & Ostriker, 1986). For the range of parameters considered, with  $m_{\text{BH}} > m_{\star}$  and  $r_{\text{p}} \sim r_{\star}$ , the values of  $T_2$  and  $T_3$  lie in the range  $0.01 - 0.1$ . These values are systematically lower for stars with lower  $\rho_{\text{conc}}$  values. As a result, in  $0.5 M_{\odot}$  stars (and ZAMS  $1 M_{\odot}$  stars),  $\varepsilon_{\text{tide}}$  is dominated by  $\varepsilon_{\text{kick}}$ , resulting in them becoming unbound from the BH. It should be noted that  $\varepsilon_{\text{tide}}$  depends very strongly on the distance of approach.

In addition, we find that the change in the specific orbital angular momentum of the star-BH system,  $h_{\text{orb}}$ , is not significant. For orbits very close to being parabolic, which is the case for all our post-disruption orbits (see Figure 5.9),  $h_{\text{orb}} \approx \sqrt{2G(m_{\star} + m_{\text{BH}})r_{\text{p}}} \approx \sqrt{2Gm_{\text{BH}}r_{\text{p}}}$ . This implies that the post-disruption periapsis distance  $r_{\text{p}} = a(1 - e)$ , where  $a$  is the semimajor axis and  $e$  is the eccentricity, is nearly the same as the initial periapsis distance  $r_{\text{p}} \equiv br_{\text{t}}$ , which is also seen in PTDEs by SMBHs (Ryu et al., 2020c). Consequently, given that  $a = -0.5 G(m_{\star} + m_{\text{BH}})/\varepsilon_{\text{orb}}$ , the calculation of  $e$  is straightforward. Figure 5.9 shows the post-disruption  $e$ , computed using Equations 5.1 and 5.2, as a function of  $b$  which follows the trend in  $\varepsilon_{\text{orb}}$ .

### 5.4.5 Rates of tidal encounters

The rate of  $\mu$ TDEs per year per Milky Way-like galaxy (similar to Perets et al., 2016) can be expressed as:

$$R_{\mu\text{TDE}} \sim N_{\text{clus}}N_{\star,c} N_{\text{BH},c} \Sigma \sigma V_c^{-1} \quad (5.10)$$

Here,  $N_{\text{clus}} \sim 150 \text{ MWGal}^{-1}$  is the number of globular clusters (in the Milky Way, e.g., [Harris, 2010](#)),  $N_{\star,c}$  is the number of stars in a cluster core,  $N_{\text{BH},c}$  is the number of BHs in a cluster core,  $\Sigma = \pi r_p^2 (1 + v_p^2/\sigma^2)$  is the gravitational focused encounter cross-section with periaapsis distance  $r_p = br_t$  (see Section 5.2) and periaapsis velocity  $v_p = \sqrt{G(m_{\text{BH}} + m_{\star})/r_p}$ , and  $\sigma$  is the velocity dispersion of the cluster. For globular clusters in the Milky Way Galaxy, the typical values of these parameters are  $n_{\star,c} = N_{\star,c} V_c^{-1} \sim 10^2\text{--}10^7 \text{ pc}^{-3}$  (e.g., [Baumgardt & Hilker, 2018](#)),  $N_{\text{BH},c} \sim 10\text{--}100$  (e.g., [Morscher et al., 2015](#); [Askar et al., 2018](#)),  $\sigma \sim 1\text{--}20 \text{ km s}^{-1}$  (e.g., [Baumgardt & Hilker, 2018](#)). With these values, and assuming  $v_p \gg \sigma$  in globular clusters, and typical star and BH masses of  $1 M_{\odot}$  and  $10 M_{\odot}$  respectively, the rate is:

$$R_{\mu\text{TDE}} \sim 10^{-6} \text{ yr}^{-1} \text{ MWGal}^{-1} \left( \frac{N_{\text{clus}}}{150 \text{ MWGal}^{-1}} \right) \left( \frac{n_{\star,c}}{10^5 \text{ pc}^{-3}} \right) \left( \frac{N_{\text{BH},c}}{100} \right) \left( \frac{\sigma}{10 \text{ km s}^{-1}} \right) \left( \frac{m_{\text{BH}} + m_{\star}}{11 M_{\odot}} \right) \left( \frac{r_p/r_t}{1.0} \right) \quad (5.11)$$

This equation implies that PTDEs (with larger  $r_p/r_t$ ) are more frequent than FTDEs. More specifically, from our simulations of TDEs of  $1 M_{\odot}$  stars by  $10 M_{\odot}$ , encounters with  $b \sim 1\text{--}2$  would result in eccentric bound orbits, which can circularize over time through tides. A more detailed rate calculation would involve integrating Equation 5.11 over a range of star and black hole masses.

The above rates are derived for  $\mu\text{TDEs}$  produced in dense stellar systems such as globular clusters and nuclear star clusters. However, other channels also contribute to  $\mu\text{TDEs}$  (see discussion in [Perets et al., 2016](#)), such as ultra-wide binaries and triples in the field ([Michaely & Perets, 2016, 2020](#)) and post-natal-kicks leading to close encounter between a newly formed BH and a stellar companion ([Michaely et al., 2016](#)). These channels may give rise  $\mu\text{TDEs}$  in young environments and in the field.

### 5.4.6 Summary of fits

Below we present the post-disruption fits detailed in previous sections for use in globular cluster codes.  $m_{\star \rightarrow \text{BH}}$  refers to the gas mass bound to the black hole after disruption, including the accreted mass.

#### Masses of remnant star and BH

$$\left( \frac{\Delta m_{\diamond}}{m_{\star}} \right) = 10^{\min \{-2.10(b-1.95\rho_{\text{conc}}^{-1}), 0\}} \quad (5.12)$$

$$\left( \frac{m_{\star \rightarrow \text{BH}}}{m_{\star}} \right) \leq 0.5 \left( \frac{\Delta m_{\diamond}}{m_{\star}} \right) \quad (5.13)$$

## Spin of remnant star

$$\left(\frac{L_\diamond}{\text{g cm}^2 \text{ s}^{-1}}\right) = 10^{(-1.50b+52.00)} \left(\frac{m_\star}{M_\odot}\right)^{-1} \left(1 - \frac{\Delta m_\diamond}{m_\star}\right)^{2.4} \quad (5.14)$$

## Validity of fits

It should be noted that the density concentration factor,  $\rho_{\text{conc}}$ , only captures the full disruption of a star. Similarly defined factors for each radius  $r$ , i.e.  $(\rho(r)/\bar{\rho})^{1/3}$ , are required to calculate the distance at which mass beyond  $r$  is lost (see [Ryu et al., 2020b](#)). Stars of higher masses tend to have much steeper density profiles when compared to  $1 M_\odot$  stars, thus Equation 5.4, which fits the mass loss, is not universal. In particular, the mass loss fit for  $2 M_\odot$  stars would involve an exponent of  $\sim 3$ , unlike our derived exponent of  $\sim 2.1$  in Equation 5.4. Similar arguments follow for the fits of spins and orbits.

	$m_\star$ [ $M_\odot$ ]	$m_{\text{BH}}$ [ $M_\odot$ ]	$b$	$H_c$	$L_\star/10^{46}$ [CGS]	$m_\diamond$ [ $M_\odot$ ]	$m_{\star \rightarrow \text{BH}}$ [ $M_\odot$ ]	$m_{\text{unbound}}$ [ $M_\odot$ ]	$L_\diamond/10^{48}$ [CGS]	$a$ [AU]	$e$
1	0.5	10.0	0.70	0.25	2	0.00	0.29	0.21	N/A	N/A	N/A
2	0.5	10.0	0.70	0.33	2	0.00	0.22	0.28	N/A	N/A	N/A
3	0.5	10.0	0.70	0.50	2	0.00	0.23	0.17	N/A	N/A	N/A
4	0.5	10.0	0.70	0.75	2	0.15	0.21	0.14	87	-0.07	1.06
5	0.5	10.0	0.70	1.00	2	0.25	0.14	0.11	97	-0.27	1.02
6	0.5	10.0	0.70	1.50	2	0.46	0.03	0.01	117	1.91	0.995
7	0.5	10.0	0.70	2.00	2	0.50	0.00	0.00	17	2.61	0.996
8	0.5	10.0	0.70	2.50	2	0.50	0.00	0.00	1	42.3	1.00
9	0.5	40.0	0.70	0.25	2	0.00	0.27	0.23	N/A	N/A	N/A
10	0.5	40.0	0.70	0.33	2	0.00	0.30	0.20	N/A	N/A	N/A
11	0.5	40.0	0.70	0.50	2	0.00	0.30	0.20	N/A	N/A	N/A
12	0.5	40.0	0.70	0.75	2	0.00	0.31	0.19	N/A	N/A	N/A
13	0.5	40.0	0.70	1.00	2	0.21	0.18	0.11	76	-0.35	1.03
14	0.5	40.0	0.70	1.50	2	0.46	0.03	0.01	110	-0.11	1.00
15	0.5	40.0	0.70	2.00	2	0.50	0.00	0.00	15	11.4	0.998
16	0.5	40.0	0.70	2.50	2	0.50	0.00	0.00	1	161	1.00
17	1.0	10.0	0.00	0.25	12	0.04	0.42	0.54	2	0.02	0.916
18	1.0	10.0	0.00	0.33	12	0.33	0.27	0.40	101	0.04	0.923
19	1.0	10.0	0.00	0.50	12	0.68	0.11	0.21	410	0.10	0.945
20	1.0	10.0	0.00	0.75	12	0.89	0.05	0.06	354	0.32	0.972
21	1.0	10.0	0.00	1.00	12	0.97	0.02	0.01	199	1.15	0.989
22	1.0	10.0	0.00	1.50	12	1.00	0.00	0.00	49	13.2	0.999
23	1.0	10.0	0.00	2.00	12	1.00	0.00	0.00	10	54.6	1.00
24	1.0	10.0	0.34	0.25	10	0.00	0.47	0.53	N/A	N/A	N/A
25	1.0	10.0	0.34	0.33	10	0.09	0.47	0.44	99	-0.06	1.12
26	1.0	10.0	0.34	0.50	10	0.49	0.20	0.31	245	0.08	0.950
27	1.0	10.0	0.34	0.75	10	0.83	0.09	0.08	440	0.21	0.965
28	1.0	10.0	0.34	1.00	10	0.95	0.03	0.02	250	0.64	0.984

29	1.0	10.0	0.34	1.50	10	1.00	0.00	0.00	49	7.77	0.998
30	1.0	10.0	0.34	2.00	10	1.00	0.00	0.00	10	87.3	1.00
31	1.0	10.0	0.70	0.25	16	0.00	0.37	0.63	N/A	N/A	N/A
32	1.0	10.0	0.70	0.33	16	0.00	0.49	0.51	N/A	N/A	N/A
33	1.0	10.0	0.70	0.50	16	0.34	0.29	0.37	163	0.28	0.986
34	1.0	10.0	0.70	0.75	16	0.68	0.16	0.16	440	0.2.2	0.968
35	1.0	10.0	0.70	1.00	16	0.90	0.06	0.04	387	0.35	0.974
36	1.0	10.0	0.70	1.50	16	1.00	0.00	0.00	67	3.43	0.996
37	1.0	10.0	0.70	2.00	16	1.00	0.00	0.00	8	25.5	0.999
38	1.0	40.0	0.00	0.25	12	0.07	0.45	0.48	56	-0.05	1.14
39	1.0	40.0	0.00	0.33	12	0.28	0.27	0.45	66	0.17	0.969
40	1.0	40.0	0.00	0.50	12	0.63	0.16	0.21	340	0.58	0.984
41	1.0	40.0	0.00	0.75	12	0.88	0.06	0.06	332	2.24	0.994
42	1.0	40.0	0.00	1.00	12	0.96	0.02	0.02	192	9.63	0.998
43	1.0	40.0	0.00	1.50	12	1.00	0.00	0.00	50	102	1.00
44	1.0	40.0	0.00	2.00	12	1.00	0.00	0.00	8	153	1.00
45	1.0	40.0	0.34	0.25	10	0.00	0.42	0.58	N/A	N/A	N/A
46	1.0	40.0	0.34	0.33	10	0.00	0.39	0.61	N/A	N/A	N/A
47	1.0	40.0	0.34	0.50	10	0.42	0.22	0.36	169	0.95	0.992
48	1.0	40.0	0.34	0.75	10	0.81	0.09	0.10	413	1.84	0.993
49	1.0	40.0	0.34	1.00	10	0.95	0.03	0.02	245	5.09	0.997
50	1.0	40.0	0.34	1.50	10	1.00	0.00	0.00	50	62.6	1.00
51	1.0	40.0	0.34	2.00	10	1.00	0.00	0.00	10	180	1.00
52	1.0	40.0	0.70	0.25	16	0.00	0.55	0.45	N/A	N/A	N/A
53	1.0	40.0	0.70	0.33	16	0.00	0.50	0.50	N/A	N/A	N/A
54	1.0	40.0	0.70	0.50	16	0.21	0.39	0.40	156	-0.12	1.06
55	1.0	40.0	0.70	0.75	16	0.63	0.18	0.19	365	-4.17	1.00
56	1.0	40.0	0.70	1.00	16	0.89	0.06	0.05	368	2.91	0.995
57	1.0	40.0	0.70	1.50	16	1.00	0.00	0.00	66	29.4	0.999
58	1.0	40.0	0.70	2.00	16	1.00	0.00	0.00	8	119	1.00

Table 5.4: Post-disruption parameter values for our 58 simulations. The columns, respectively, denote star mass  $m_*$ , BH mass  $m_{\text{BH}}$ , impact parameter  $b$ , central hydrogen abundance  $H_c$ , initial (almost non-rotating) star spin angular momentum  $L_*$ , remnant mass  $m_\diamond$ , gas mass bound to BH  $m_{*\rightarrow\text{BH}}$ , gas mass unbound from the BH-star system  $m_{\text{unbound}}$ , remnant spin angular momentum  $L_\diamond$ , orbital semimajor axis  $a$  and orbital eccentricity  $e$ .

## 5.5 Implications

In this section, we discuss the general observational implications and the caveats of our study.  $\mu$ TDEs can potentially produce both unique and peculiar transient events as well as longer-lived systems.

### 5.5.1 Low-mass X-ray binaries

Low-mass X-ray binaries (LMXBs) are interacting binary systems which consist of compact objects (neutrons stars or black holes) accreting mass from their low-mass ( $\lesssim 1 M_{\odot}$ ) stellar companions, thereby producing X-rays. A few hundred of LMXBs have been detected in the Milky Way Galaxy (e.g., Liu et al., 2007; Avakyan et al., 2023), highlighting the prevalence of such systems. However, theoretical (e.g., Portegies Zwart et al., 1997; Kalogera, 1999) and population synthesis (e.g., Podsiadlowski et al., 2003; Kiel & Hurley, 2006) studies have not been able to match the rates of observed LMBXs through isolated binary evolution alone. The primary reason is that a low-mass companion has insufficient energy to expel a common envelope during the giant phase of the primary star, thereby resulting in the spiraling in of the companion and an eventual merger. Thus, a dynamical channel formation channel for LMXBs, where a low-mass star is tidally captured by a black hole in a globular/nuclear cluster, holds promise (e.g., Voss & Gilfanov, 2007; Michaely & Perets, 2016; Klencki et al., 2017).

Some of our simulations of encounters of low-mass stars with black holes are not close enough for significant mass loss and can result in highly eccentric bound orbits. For example, in the parabolic encounter of a  $1 M_{\odot}$  star and a  $10 M_{\odot}$  BH, for  $b \sim 1.0\text{--}1.5$  (see Section 5.4), the fractional mass loss is  $\sim 1\text{--}10\%$ , and the post-disruption bound orbit has a period of  $0.1\text{--}1$  yr and an eccentricity of  $\sim 0.97\text{--}0.98$ . However, tidal dissipation at subsequent periapsis passages can reduce the eccentricity and orbital period (e.g., Klencki et al., 2017) such that the resulting bound system evolves into a compact LMXB.

Another type of system that is potentially formed through dynamical encounters are non-interacting BH-star systems, e.g., El-Badry et al. (2023b,a); Chakrabarti et al. (2023). These systems consist of  $\sim 1 M_{\odot}$  stars orbiting  $\sim 10 M_{\odot}$  black holes in moderately-eccentric orbits with periods of  $\sim 1$  yr. These parameters correspond quite well with our simulations with  $b \sim 1.0\text{--}1.5$ , which lends credence to dynamical formation.

### 5.5.2 Intermediate-mass black hole growth

Intermediate-mass black holes (IMBHs; see Greene et al., 2020 for a review), with masses greater than those of stellar-mass black holes ( $\gtrsim 10^2 M_{\odot}$ ) and less than those of supermassive black holes ( $\lesssim 10^6 M_{\odot}$ ), are expected to exist in the centers of dwarf galaxies (e.g., Kunth et al., 1987; Filippenko & Sargent, 1989; Reines, 2022; Gültekin et al., 2022) and globular clusters (e.g., Davis et al., 2011; Farrell et al., 2014; Pechetti et al., 2022). Among several IMBH formation mechanisms (see Volonteri et al., 2021 for review), one possible avenue is runaway mass growth through tidal capture and disruption, which has been examined analytically (e.g., Stone et al., 2017b) and numerically (e.g., Rizzuto et al., 2023; Arca Sedda et al., 2023). One of the most critical factors in this mechanism for BH growth is the amount of debris mass that ultimately accretes onto the BH. For example, Rizzuto et al. (2023) assume that a star approaching a BH within the nominal tidal radius  $r_t$  is fully destroyed and 50% of the stellar mass is accreted onto the BH.

While these assumptions may be valid for a part of the parameter space, it is important

to develop a prescription for the outcomes of TDEs that works over a broader parameter range to more accurately assess the possibility of BH mass growth through TDEs. Our simulations can provide such prescriptions that can improve the treatment of TDEs. Firstly, our simulations show, like previous work on TDEs by supermassive black holes (e.g., Guillochon & Ramirez-Ruiz, 2013; Mainetti et al., 2017; Goicovic et al., 2019; Ryu et al., 2020a,b,c,d; Law-Smith et al., 2020), that the periapsis distances at which stars are fully or partially destroyed depend on the stellar internal structure. Ryu et al. (2020b) analytically demonstrated that the nominal tidal radius  $r_t$  is a more relevant quantity for partial disruption events involving stars with  $m_\star \gtrsim 1 M_\odot$ . Only for lower-mass stars, where  $\rho_{\text{conc}} \sim 1$ , does  $r_t$  come close to the genuine full disruption radius<sup>4</sup>. Our fitting formula for the fractional mass loss, Equation 5.4, can provide a better prescription for determining the fate of the star (full or partial disruption) as well as the mass of the remnant.

The amount of debris accreted onto the BH remains highly uncertain. To the zeroth order, if the accretion rate is super-Eddington, the strong radiation pressure gradient would drive strong outflows, hindering continuous and steady accretion (Sądowski et al., 2014). However, the accretion efficiency would be collectively affected by many factors, including magnetic fields, black hole spins, accretion flow structure, and jet formation (e.g., Sądowski et al., 2014; Jiang et al., 2019; Curd & Narayan, 2023; Kaaz et al., 2023). Our fitting formulae for the fractional mass loss cannot provide an accurate prescription for the accreted mass but can place constraints on the maximum mass that can be accreted onto the BH.

### 5.5.3 Fast blue optical transients

Fast blue optical transients (FBOTs) are a class of optical transients characterized by high peak luminosities  $> 10^{43} \text{ erg s}^{-1}$ , rapid rise and decay times of the order of a few days, blue colors (Perets et al., 2011; Drout et al., 2014), and peak blackbody temperatures of a few  $10^4 \text{ K}$ . Although a majority of these events can be explained by supernovae with low-mass ejecta (Pursiainen et al., 2018), a ‘luminous’ subset, e.g., AT2018cow (‘the Cow’; Smartt et al., 2018; Prentice et al., 2018), AT2018lqh (Ofek et al., 2021), AT2020mrf (Yao et al., 2022), CSS161010 (Coppejans et al., 2020), ZTF18abvkwla (‘the Koala’; Ho et al., 2020), AT2020xnd (‘the Camel’; Perley et al., 2021), AT2022tsd (‘the Tasmanian Devil’; Matthews et al., 2023), AT2023fhn (‘the Finch’; Chrimes et al., 2024), are too bright at their peaks and fade too rapidly to be explained by supernovae. Proposed mechanisms involve compact objects, such as black hole accretion or magnetars formed in core-collapse supernovae (Prentice et al., 2018), mergers between Wolf-Rayet stars and compact objects accompanied by hyper-accretion (Metzger, 2022), or tidal disruption events by intermediate-mass BHs (Kuin et al., 2019) or stellar-mass BHs (Kremer et al., 2021).

Some luminous FBOTs also emit in radio or X-ray (e.g., Margutti et al., 2019; Ho et al., 2020) which indicates the presence of a circumstellar medium that may result from

---

<sup>4</sup>The genuine full disruption radius and the partial disruption radius are proportional to  $\rho_c^{-1/3}$  and  $\bar{\rho}^{-1/3}$  respectively (see Section 4 of (Ryu et al., 2020b)).

partial TDEs (Kremer et al., 2021). Our simulations support this notion by showing the presence of debris near the BH with occasional weak outflows from the BH. In addition, the remnants in our simulations are often bound to the BH and can subsequently undergo multiple partial disruptions, e.g., our simulations of TAMS  $1 M_{\odot}$  stars and  $10 M_{\odot}$  BHs for  $b = 0.25$  or  $b = 0.33$ . While we cannot confirm a direct correlation between FBOTs and  $\mu$ TDEs, multiple disruption events of a star may fulfill some of the astrophysical conditions (e.g., the presence of a gas medium and rapid accretion onto a compact object) necessary to explain FBOTs with radio emission. For such cases, the detection of repeated bursts in FBOTs could provide valuable constraints on their formation mechanisms.

### 5.5.4 Ultra-long gamma-ray bursts and X-ray flares

The exact appearance of transients resulting from  $\mu$ TDEs is highly uncertain and depends on various assumptions. Perets et al. (2016) suggested that, if the accretion onto the BH is efficient and gives rise to jets, there is a possibility of producing ultra-long gamma-ray bursts (GRBs) and/or X-ray flares (XRFs).

Assuming a proportional relation between the material accreted to the compact object and the luminosity produced by the jet, we can generally divide  $\mu$ TDEs into two regimes: (1)  $t_{\min} \gg t_{\text{acc}}$  and (2)  $t_{\min} \ll t_{\text{acc}}$ , where  $t_{\min}$  is the typical fallback time of the debris following the disruption, and  $t_{\text{acc}}$  is the typical viscous time of the accretion disk that can form around the BH (see Perets et al., 2016 for more details).

- $t_{\min} \gg t_{\text{acc}}$ : When the mass of the star is much smaller than that of the BH, the accretion evolution is dominated by the fallback rate, i.e., the light curve should generally follow the regular power-law (e.g.  $t^{-5/3}$  power-law for a full disruption).
- $t_{\min} \ll t_{\text{acc}}$ : When the masses of the star and the BH are comparable, the fallback material is expected to accumulate and form a disk on the fallback time, which then drains on the longer viscous time maintaining a low accretion rate. We would expect the flaring to begin only once the material is accreted onto the compact object. Therefore, we expect four stages in the light curve evolution: (1) A fast rise of the accretion flare once the disk material is processed and evolves to accrete on the compact object. (2) Accretion from the disk until the accumulated early fallback material is drained; if we *assume* a steady state accretion until drainage, one might expect a relatively flat light curve. (3) Once the disk drains the accumulated early fall-back material the light curve should drop steeply. (4) The continuous fall-back of material would govern the accretion rate at times longer than the viscous time, and the accretion rate should then follow the  $t^{-5/3}$  rate (or a different power-law). The exact light curve at the early stages is difficult to predict, but we do note a non-trivial signature of the  $\mu$ TDEs relating to the early and late stages.

The expected properties of  $\mu$ TDEs are consistent with and might explain the origins of ultra-long GRBs (Levan et al., 2014): long-lived ( $\sim 10^4$  s) GRBs which show an initial plateau followed by a rapid decay.  $\mu$ TDEs may also explain the origin of some Swift TDE



candidates (Bloom et al., 2011; Burrows et al., 2011; Cenko et al., 2012; Brown et al., 2015), suggested to be produced through a TDE by a supermassive BH. The typical timescales for the latter are longer than the observed  $10^5$  s, challenging the currently suggested origin, but quite consistent with a  $\mu$ TDE scenario.

$\mu$ TDEs producing ultra-long GRBs are also expected to produce afterglow emission if/when the strong outflows and jets launched by accretion propagate into the surrounding medium and the resulting shock interaction produces high energy particles which give rise to synchrotron and inverse Compton radiation. Such observational signature of  $\mu$ TDE has been little explored, though analogous observation and modeling have been suggested for TDEs by massive black holes (e.g., Giannios & Metzger, 2011; Zauderer et al., 2011). Detection of afterglows from  $\mu$ TDEs would provide information on the energetics and dynamics of the outflow, robust independent evidence for the jet collimation, as well as identification of the host galaxy.

### 5.5.5 Remnants

Partial  $\mu$ TDEs of stars by stellar BHs can spin up the stars significantly due to strong tidal interactions (see Fig.5.7 and Alexander & Kumar, 2001). Though magnetic braking can potentially spin down such stars over time, observations of highly spun-up low-mass old stars in globular clusters could provide potential signatures for partial  $\mu$ TDEs. In addition, the remnant undergoes violent chemical mixing during the first pericenter passage and has higher entropy than an ordinary star of the same mass and age (Ryu et al., 2020c, 2023a). If the mass loss is significant, a unique chemical composition profile may persist even after the remnant has relaxed to a stable state. This suggests that the remnant could exhibit unique asteroseismic signatures that distinguish it from ordinary stars (Bellinger et al., 2023, in prep).

### 5.5.6 Caveats

As mentioned in Section 5.2, we exclude the effects of relativity and magnetic fields in our study. The Newtonian approximation is justified for TDEs by SBHs because most of the debris stays outside  $r_p$ , which is approximately four orders of magnitude greater than the gravitational radius  $r_g \equiv Gm_{\text{BH}}/c^2$ <sup>5</sup>. However, relativistic effects and proper treatment of radiation are more important for the accretion flow, which is beyond the scope of our paper. The effect of magnetic fields on the dynamics of the remnant is unclear, which we will leave for our future work. A final point to note is that, unlike globular clusters, nuclear star clusters have typical velocity dispersions of  $\sigma \gtrsim 100 \text{ km s}^{-1}$  (Figer et al., 2003; Schödel et al., 2009) depending on the galaxy, and subsequently,  $|1 - e| \gtrsim 10^{-2}$ . Thus, encounters are not always parabolic, and for a more thorough study, hyperbolic encounters must be taken into account.

<sup>5</sup>On the other hand, for TDEs with SMBHs,  $r_g$  and  $r_t$  can be comparable in scale.

## 5.6 Summary and conclusion

We performed a grid of 58 hydrodynamics simulations, using the moving-mesh code `AREPO`, of partial (PTDE) and full (FTDE) tidal disruptions of main-sequence (MS) stars with stellar-mass black holes (SBH) on initially-parabolic orbits. Our varied parameters include stellar mass  $m_\star$  ( $0.5 M_\odot$  and  $1.0 M_\odot$ ), SBH mass ( $10 M_\odot$  and  $40 M_\odot$ ), core hydrogen abundance  $H_c$  (a proxy for MS age  $t_\star$ ) and impact parameter  $b \equiv r_p/r_t$ . Our stellar models are initialized in accordance with 1D detailed non-rotating stellar profiles from `MESA`. We also define a star’s density concentration parameter  $\rho_{\text{conc}} \equiv (\rho_c/\bar{\rho})^{1/3}$ . Our main results are summarized below:

- The mass of a post-disruption stellar remnant  $m_\diamond$  decreases with decreasing  $b$ . A higher  $\rho_{\text{conc}}$  (more centrally concentrated) results in a lesser mass loss for the same  $b$ .  $m_\diamond$  depends only on  $b$  and  $\rho_{\text{conc}}$ , and not on  $m_{\text{BH}}$ . Roughly half of the disrupted mass remains bound to the black hole, while the other half is unbound from the system.
- The spin angular momentum of a stellar remnant  $L_\diamond$  increases after periapsis passage. For large  $b$  (when the mass loss is small),  $L_\diamond$  increases with decreasing  $b$ , but this trend reverses for very small  $b$  (close to FTDE) due to significant mass loss. This reversal occurs for lower  $b$  when  $\rho_{\text{conc}}$  is higher. The final spin is also independent of  $m_{\text{BH}}$ . For low  $b$  values, the rotational velocities can be very close to break-up velocities.
- Unlike mass and spin, the orbit of the remnant star also depends on  $m_{\text{BH}}$ . For large  $b$ , eccentricity  $e$  and semimajor axis  $a$  decrease with decreasing  $b$  keeping a constant periapsis distance, i.e., the remnant tends to be more ‘bound’. Depending on  $m_{\text{BH}}$  and  $\rho_{\text{conc}}$ , this no longer holds for approaches close to FTDE –  $e$  can increase and the remnant can become unbound. In general, a higher  $m_{\text{BH}}/m_\star$  ratio and a lower  $\rho_{\text{conc}}$  tend to be unbinding.
- We provide relatively simple and accurate fitting formulae for the masses and spins of the remnant stars. These analytical fits are listed in Section 5.4.6 for easy access.

We discussed the implications that  $\mu$ TDEs can have on low-mass X-ray binary formation, intermediate-mass black hole formation, and transient searches. Given the limited range of stellar masses and ages that we covered in this work, we will extend our suite of simulations in the future to cover a wider parameter space, including massive stars. It is necessary to explore this regime to model stellar dynamics in dense stellar clusters.

# Chapter 6

## Conclusions

The preceding chapters have highlighted the pivotal role of gravitational dynamics in the evolution of stellar systems. I specifically explored the influence of multiple-star dynamics on gravitational wave emission, the stability of these systems, and the consequences of close tidal encounters between stars and black holes on stellar structure and dynamics. In the following paragraphs, I provide an overview of these studies, discussing the results and offering a general outlook.

In Chapter 2, I conducted a population synthesis study using the MSE code ([Hamers et al., 2021a](#)) to statistically analyze compact object mergers in 2+2 and 3+1 quadruples. Given the vast parameter space and numerous uncertainties, I compared different models by adjusting parameters such as supernova kicks, metallicities, and the occurrence of fly-bys. Notably, I found that secular orbital evolution significantly influences (15–30)% of all compact object mergers in quadruple-star systems. Furthermore, binary black hole mergers in quadruple-star systems can account for a notable fraction of detected LIGO rates, while the rates of binary neutron star mergers and black hole-neutron star mergers fall short. Supernova kicks emerged as the most crucial factor in compact object mergers, as they dictate the boundedness of binaries. The distributions of LIGO band eccentricities and effective spin parameters of these mergers closely resemble those from isolated binary evolution. These findings underscore the importance of quadruples and triples in the search for gravitational wave progenitors, calling for further population synthesis studies to validate and refine our results.

In Chapter 3, I explored the dynamical stability of triple-star systems using the MSTAR code ([Rantala et al., 2020](#)). By integrating orbits across a broad parameter space of triples, encompassing variations in masses, semimajor axes, eccentricities, and orbital angles, I developed two classifiers to categorize stable and unstable triples. The first classifier involved updating the analytical criterion proposed by [Mardling & Aarseth \(2001\)](#), aiming to improve the dependence of stability on inclination and eccentricity. The second, a neural network classifier, was trained on the large  $N$ -body integrated sample of triples. These classifiers demonstrated remarkable accuracy rates of 93% and 95% respectively, surpassing existing analytical criteria. Thus, they hold significant promise for future studies on triple-star systems.

In Chapter 4, I extended our study on dynamical stability to 2+2 and 3+1 quadruple-star systems. I once more employed the `MSTAR` code to generate a large sample of quadruples for neural network classification. This comprehensive study marked the first detailed exploration of quadruple stability across a large parameter space. Notably, our analysis revealed that the 'nested' triple approach, approximating quadruples as two triples each, does not accurately characterize stability, particularly for 3+1 quadruples. However, our neural network classifiers, one each for 2+2 and 3+1 quadruple-star systems, demonstrated impressive classification accuracies of 94% and 93% respectively, enhancing our ability to identify stable and unstable systems. These classifiers can be readily implemented for future investigations into quadruple-star systems.

In Chapter 5, I performed a suite of hydrodynamics simulations of micro-tidal disruption events ( $\mu$ TDE) using the `AREPO` code (Springel, 2010; Weinberger et al., 2020) to examine the post-disruption remnants' properties. Employing realistic stellar models created using the `MESA` code (Paxton et al., 2011), I found that, apart from the stellar and black hole masses, the internal density profile of the star dictates the extent of mass loss during a  $\mu$ TDE. Moreover, the remnant experiences spin-up due to torque from the black hole, with the increase in spin angular momentum being more pronounced for closer approach distances. However, very close approaches result in significant disruption and lower spin angular momentum. The orbital trajectory of the remnant after periapsis passage exhibits a striking non-linear dependence on the distance of approach. While less severe disruptions result in bound orbits, significantly disrupted remnants may become unbound from the black hole entirely. I also provided best-fit functions for these post-disruption properties to integrate into cluster codes. Moving forward, it is crucial to broaden this study across parameter space, encompassing high-mass stars and stars in various evolutionary stages.

# Glossary of abbreviations

MS	Main-Sequence
ZAMS	Zero-Age Main-Sequence
MAMS	Middle-Age Main-Sequence
TAMS	Terminal-Age Main-Sequence
HG	Hertzsprung Gap
RGB	Red Giant Branch
CHeB	Core-Helium Burning
EAB	Early Asymptotic Giant Branch
TPAGB	Thermally Pulsing Asymptotic Giant Branch
HeMS	(Naked) Helium star Main-Sequence
HeHG	(Naked) Helium star Hertzsprung Gap
HeGB	(Naked) Helium star Giant Branch
WD	White Dwarf
HeWD	Helium White Dwarf
COWD	Carbon-Oxygen White Dwarf
ONeWD	Oxygen-Neon White Dwarf
NS	Neutron Star
BH	Black Hole
SBH	Stellar(-mass) Black Hole
IMBH	Intermediate-Mass Black Hole
SMBH	Supermassive Black Hole
SN	Supernova
RLOF	Roche-Lobe Overflow
CE/CEE	Common Envelope (Evolution)
ZLK/LK	(von Zeipel)-Lidov-Kozai
PN	Post-Newtonian
GW	Gravitational Wave
GWTC	Gravitational Wave Transient Catalog
LIGO	Laser Interferometer Gravitational-Wave Observatory
MSE	Multiple Stellar Evolution (code)
SSE	Single Star Evolution (code)
BSE	Binary Star Evolution (code)
MSC	Multiple Star Catalog
StCr	(Analytical) Stability Criterion
ML	Machine Learning
MLP	Multi-Layer Perceptron
ANN	Artificial Neural-Network
TDE	Tidal Disruption Event
$\mu$ TDE	Micro-Tidal Disruption Event

PTDE	Partial Tidal Disruption Event
FTDE	Full Tidal Disruption Event
SPH	Smoothed-Particle Hydrodynamics
LMXB	Low-Mass X-ray Binary
FBOT	Fast Blue Optical Transient
GRB	Gamma-Ray Burst

Table 6.1: Table of abbreviations used in the previous chapters.

# Bibliography

Abbott B. P., et al., 2016, [Phys. Rev. Lett.](#), **116**, 061102

Abbott B. P., et al., 2017, [ApJ](#), **848**, L12

Abbott B. P., et al., 2019, [Physical Review X](#), **9**, 031040

Abbott R., et al., 2020, [Phys. Rev. D](#), **102**, 043015

Abbott R., et al., 2021a, [Physical Review X](#), **11**, 021053

Abbott R., et al., 2021b, [ApJ](#), **913**, L7

Abbott R., et al., 2021c, [ApJ](#), **915**, L5

Abbott R., et al., 2023, [Physical Review X](#), **13**, 011048

Alexander M. E., 1973, [Ap&SS](#), **23**, 459

Alexander T., Kumar P., 2001, [ApJ](#), **549**, 948

Ali-Haïmoud Y., Kovetz E. D., Kamionkowski M., 2017, [Phys. Rev. D](#), **96**, 123523

Antognini J. M. O., 2015, [MNRAS](#), **452**, 3610

Antognini J. M. O., Thompson T. A., 2016, [MNRAS](#), **456**, 4219

Antonini F., Perets H. B., 2012, [ApJ](#), **757**, 27

Antonini F., Rasio F. A., 2016, [ApJ](#), **831**, 187

Antonini F., Chatterjee S., Rodriguez C. L., Morscher M., Pattabiraman B., Kalogera V., Rasio F. A., 2016, [ApJ](#), **816**, 65

Antonini F., Toonen S., Hamers A. S., 2017, [ApJ](#), **841**, 77

Arca-Sedda M., Gualandris A., 2018, [MNRAS](#), **477**, 4423

Arca Sedda M., Li G., Kocsis B., 2021, [A&A](#), **650**, A189

- Arca Sedda M., Kamlah A. W. H., Spurzem R., Rizzuto F. P., Naab T., Giersz M., Berczik P., 2023, *MNRAS*, 526, 429
- Askar A., Arca Sedda M., Giersz M., 2018, *MNRAS*, 478, 1844
- Avakyan A., Neumann M., Zainab A., Doroshenko V., Wilms J., Santangelo A., 2023, *A&A*, 675, A199
- Backer D. C., Kulkarni S. R., Heiles C., Davis M. M., Goss W. M., 1982, *Nature*, 300, 615
- Bagla J. S., 2002, *Journal of Astrophysics and Astronomy*, 23, 185
- Banerjee S., 2017, *MNRAS*, 467, 524
- Banerjee S., Baumgardt H., Kroupa P., 2010, *MNRAS*, 402, 371
- Bartos I., Kocsis B., Haiman Z., Márka S., 2017, *ApJ*, 835, 165
- Baumgardt H., Hilker M., 2018, *MNRAS*, 478, 1520
- Belczynski K., Kalogera V., Bulik T., 2002, *ApJ*, 572, 407
- Belczynski K., Holz D. E., Bulik T., O’Shaughnessy R., 2016, *Nature*, 534, 512
- Bellinger E., Ryu T., Spruit H., 2023, (in prep)
- Bellm E. C., et al., 2019, *PASP*, 131, 018002
- Bessel F. W., 1844, *MNRAS*, 6, 136
- Binney J., Tremaine S., 2008, *Galactic Dynamics: Second Edition*
- Bird S., Cholis I., Muñoz J. B., Ali-Haïmoud Y., Kamionkowski M., Kovetz E. D., Raccañelli A., Riess A. G., 2016, *Phys. Rev. Lett.*, 116, 201301
- Blaes O., Lee M. H., Socrates A., 2002, *ApJ*, 578, 775
- Bloom J. S., et al., 2011, *Science*, 333, 203
- Broekgaarden F. S., et al., 2021, *MNRAS*,
- Brown G. C., Levan A. J., Stanway E. R., Tanvir N. R., Cenko S. B., Berger E., Chornock R., Cucchiaria A., 2015, *MNRAS*, 452, 4297
- Burmester U. P., Ferrario L., Pakmor R., Seitzzahl I. R., Ruiter A. J., Hole M., 2023, *MNRAS*, 523, 527
- Burrows D. N., et al., 2011, *Nature*, 476, 421
- Campbell W. W., 1899, *ApJ*, 10, 177



- Cenko S. B., et al., 2012, [ApJ](#), **753**, 77
- Chakrabarti S., et al., 2023, [AJ](#), **166**, 6
- Chambers K. C., et al., 2016, [arXiv e-prints](#), p. [arXiv:1612.05560](#)
- Chatterjee S., Rodriguez C. L., Kalogera V., Rasio F. A., 2017, [ApJ](#), **836**, L26
- Chirikov B. V., 1979, [Phys. Rep.](#), **52**, 263
- Chrimes A. A., et al., 2024, [MNRAS](#), **527**, L47
- Chruslinska M., Belczynski K., Klencki J., Benacquista M., 2018, [MNRAS](#), **474**, 2937
- Coppejans D. L., et al., 2020, [ApJ](#), **895**, L23
- Curd B., Narayan R., 2023, [MNRAS](#), **518**, 3441
- Davis S. W., Narayan R., Zhu Y., Barret D., Farrell S. A., Godet O., Servillat M., Webb N. A., 2011, [ApJ](#), **734**, 111
- De Angeli F., Piotto G., Cassisi S., Busso G., Recio-Blanco A., Salaris M., Aparicio A., Rosenberg A., 2005, [AJ](#), **130**, 116
- Delgado-Donate E. J., Clarke C. J., Bate M. R., Hodgkin S. T., 2004, [MNRAS](#), **351**, 617
- Dominik M., Belczynski K., Fryer C., Holz D. E., Berti E., Bulik T., Mandel I., O'Shaughnessy R., 2012, [ApJ](#), **759**, 52
- Dosopoulou F., Kalogera V., 2016, [ApJ](#), **825**, 71
- Drout M. R., et al., 2014, [ApJ](#), **794**, 23
- Duchêne G., Kraus A., 2013, [ARA&A](#), **51**, 269
- Dunlop J., 1828, *Philosophical Transactions of the Royal Society of London Series I*, **118**, 113
- Eggleton P. P., 1983, [ApJ](#), **268**, 368
- Eggleton P., Kiseleva L., 1995, [ApJ](#), **455**, 640
- Eggleton P. P., Kiseleva L. G., Hut P., 1998, [ApJ](#), **499**, 853
- El-Badry K., et al., 2023a, [MNRAS](#), **518**, 1057
- El-Badry K., et al., 2023b, [MNRAS](#), **521**, 4323
- Farrell S. A., et al., 2014, [MNRAS](#), **437**, 1208

- Figer D. F., et al., 2003, [ApJ](#), 599, 1139
- Filippenko A. V., Sargent W. L. W., 1989, [ApJ](#), 342, L11
- Flammarion C., 1877, *Astronomical register*, 15, 186
- Fragione G., Kocsis B., 2019, [MNRAS](#), 486, 4781
- Fragione G., Loeb A., 2019, [MNRAS](#), 486, 4443
- Fragione G., Grishin E., Leigh N. W. C., Perets H. B., Perna R., 2019, [MNRAS](#), 488, 47
- Fragione G., Loeb A., Rasio F. A., 2020, [ApJ](#), 895, L15
- Fragione G., Loeb A., Rasio F. A., 2021, [ApJ](#), 918, L38
- Furuhjelm R., 1914, [Astronomische Nachrichten](#), 197, 181
- Gallegos-Garcia M., Law-Smith J., Ramirez-Ruiz E., 2018, [ApJ](#), 857, 109
- Gehrels N., et al., 2004, [ApJ](#), 611, 1005
- Gezari S., 2021, [ARA&A](#), 59, 21
- Giacobbo N., Mapelli M., 2018, [MNRAS](#), 480, 2011
- Giacobbo N., Mapelli M., Spera M., 2018, [MNRAS](#), 474, 2959
- Giannios D., Metzger B. D., 2011, [MNRAS](#), 416, 2102
- Ginat Y. B., Perets H. B., 2021, [Physical Review X](#), 11, 031020
- Glanz H., Perets H. B., Pakmor R., 2023, [arXiv e-prints](#), p. arXiv:2309.03300
- Goicovic F. G., Springel V., Ohlmann S. T., Pakmor R., 2019, [MNRAS](#), 487, 981
- Golightly E. C. A., Nixon C. J., Coughlin E. R., 2019, [ApJ](#), 882, L26
- Greene J. E., Strader J., Ho L. C., 2020, [ARA&A](#), 58, 257
- Grishin E., Perets H. B., Zenati Y., Michaely E., 2017, [MNRAS](#), 466, 276
- Grishin E., Lai D., Perets H. B., 2018, [MNRAS](#), 474, 3547
- Gronow S., Collins C. E., Sim S. A., Röpkke F. K., 2021, [A&A](#), 649, A155
- Guillochon J., Ramirez-Ruiz E., 2013, [ApJ](#), 767, 25
- Gültekin K., et al., 2022, [MNRAS](#), 516, 6123

- Halley E., 1715, Philosophical Transactions of the Royal Society of London Series I, [29](#), [390](#)
- Hamers A. S., 2017, [MNRAS](#), [466](#), [4107](#)
- Hamers A. S., 2018a, [MNRAS](#), [476](#), [4139](#)
- Hamers A. S., 2018b, [MNRAS](#), [478](#), [620](#)
- Hamers A. S., 2019, [MNRAS](#), [482](#), [2262](#)
- Hamers A. S., 2020, [MNRAS](#), [494](#), [5492](#)
- Hamers A. S., 2021, [MNRAS](#), [500](#), [3481](#)
- Hamers A. S., Lai D., 2017, [MNRAS](#), [470](#), [1657](#)
- Hamers A. S., Portegies Zwart S. F., 2016, [MNRAS](#), [459](#), [2827](#)
- Hamers A. S., Samsing J., 2019, [MNRAS](#), [487](#), [5630](#)
- Hamers A. S., Tremaine S., 2017, [AJ](#), [154](#), [272](#)
- Hamers A. S., Pols O. R., Claeys J. S. W., Nelemans G., 2013, [MNRAS](#), [430](#), [2262](#)
- Hamers A. S., Perets H. B., Antonini F., Portegies Zwart S. F., 2015, [MNRAS](#), [449](#), [4221](#)
- Hamers A. S., Bar-Or B., Petrovich C., Antonini F., 2018, [ApJ](#), [865](#), [2](#)
- Hamers A. S., Rantala A., Neunteufel P., Preece H., Vynatheya P., 2021a, [MNRAS](#), [502](#), [4479](#)
- Hamers A. S., Fragione G., Neunteufel P., Kocsis B., 2021b, [MNRAS](#), [506](#), [5345](#)
- Harris W. E., 2010, [arXiv e-prints](#), p. [arXiv:1012.3224](#)
- Hastie T., Tibshirani R., Friedman J., 2009, The elements of statistical learning: data mining, inference and prediction, 2 edn. Springer, <http://www-stat.stanford.edu/~tibs/ElemStatLearn/>
- Hayashi T., Trani A. A., Suto Y., 2022, [ApJ](#), [939](#), [81](#)
- Hayashi T., Trani A. A., Suto Y., 2023, [ApJ](#), [943](#), [58](#)
- Heggie D. C., 1975, [MNRAS](#), [173](#), [729](#)
- Heggie D. C., Rasio F. A., 1996, [MNRAS](#), [282](#), [1064](#)
- Heintz W. D., 1980, [ApJS](#), [44](#), [111](#)

- Heintz W. D., 1988, [PASP](#), **100**, 834
- Ho A. Y. Q., et al., 2020, [ApJ](#), **895**, 49
- Hoang B.-M., Naoz S., Kocsis B., Rasio F. A., Dosopoulou F., 2018, [ApJ](#), **856**, 140
- Hobbs G., Lorimer D. R., Lyne A. G., Kramer M., 2005, [MNRAS](#), **360**, 974
- Hurley J. R., Pols O. R., Tout C. A., 2000, [MNRAS](#), **315**, 543
- Hurley J. R., Tout C. A., Pols O. R., 2002, [MNRAS](#), **329**, 897
- Hut P., 1981, [A&A](#), **99**, 126
- Hut P., Bahcall J. N., 1983, [ApJ](#), **268**, 319
- Hut P., et al., 1992, [PASP](#), **104**, 981
- Iben Icko J., Livio M., 1993, [PASP](#), **105**, 1373
- Innes R. T. A., 1915, Circular of the Union Observatory Johannesburg, **30**, 235
- Ito T., Ohtsuka K., 2019, [Monographs on Environment, Earth and Planets](#), **7**, 1
- Ivanova N., et al., 2013, [A&ARv](#), **21**, 59
- Jansen F., et al., 2001, [A&A](#), **365**, L1
- Jeans J. H., 1919, [MNRAS](#), **79**, 408
- Jiang Y.-F., Stone J. M., Davis S. W., 2019, [ApJ](#), **880**, 67
- Joy A. H., 1954, [ApJ](#), **120**, 377
- Kaaz N., Murguia-Berthier A., Chatterjee K., Liska M. T. P., Tchekhovskoy A., 2023, [ApJ](#), **950**, 31
- Kalogera V., 1999, [ApJ](#), **521**, 723
- Kameswara-Rao N., Vagiswari A., Louis C., 1984, Bulletin of the Astronomical Society of India, **12**, 81
- Kiel P. D., Hurley J. R., 2006, [MNRAS](#), **369**, 1152
- Kingma D., Ba J., 2014, International Conference on Learning Representations
- Kiroğlu F., Lombardi J. C., Kremer K., Fragione G., Fogarty S., Rasio F. A., 2023, [ApJ](#), **948**, 89
- Klencki J., Wiktorowicz G., Gładysz W., Belczynski K., 2017, [MNRAS](#), **469**, 3088

- Kochanek C. S., et al., 2017, [PASP](#), **129**, 104502
- Kollmeier J., et al., 2019, in *Bulletin of the American Astronomical Society*. p. 274
- Kozai Y., 1962, [AJ](#), **67**, 591
- Kramer M., Schneider F. R. N., Ohlmann S. T., Geier S., Schaffenroth V., Pakmor R., Röpke F. K., 2020, [A&A](#), **642**, A97
- Kremer K., Lu W., Piro A. L., Chatterjee S., Rasio F. A., Ye C. S., 2021, [ApJ](#), **911**, 104
- Kremer K., Lombardi J. C., Lu W., Piro A. L., Rasio F. A., 2022, [ApJ](#), **933**, 203
- Kroupa P., 2001, [MNRAS](#), **322**, 231
- Kuin N. P. M., et al., 2019, [MNRAS](#), **487**, 2505
- Kunth D., Sargent W. L. W., Bothun G. D., 1987, [AJ](#), **93**, 29
- Lada C. J., Lada E. A., 2003, [ARA&A](#), **41**, 57
- Lalande F., Trani A. A., 2022, [ApJ](#), **938**, 18
- Law-Smith J., Guillochon J., Ramirez-Ruiz E., 2019, [ApJ](#), **882**, L25
- Law-Smith J. A. P., Coulter D. A., Guillochon J., Mockler B., Ramirez-Ruiz E., 2020, [ApJ](#), **905**, 141
- Law N. M., et al., 2009, [PASP](#), **121**, 1395
- Lee H. M., Ostriker J. P., 1986, [ApJ](#), **310**, 176
- Lei H., Circi C., Ortore E., 2018, [MNRAS](#), **481**, 4602
- Levan A. J., et al., 2014, [ApJ](#), **781**, 13
- Lidov M. L., 1962, [Planet. Space Sci.](#), **9**, 719
- Lin D. N. C., Tremaine S., 1980, [ApJ](#), **242**, 789
- Lioutas G., Bauswein A., Soutanis T., Pakmor R., Springel V., Röpke F. K., 2024, [MNRAS](#),
- Liu B., Lai D., 2018, [ApJ](#), **863**, 68
- Liu B., Lai D., 2019, [MNRAS](#), **483**, 4060
- Liu Q. Z., van Paradijs J., van den Heuvel E. P. J., 2007, [A&A](#), **469**, 807
- Livio M., Soker N., 1988, [ApJ](#), **329**, 764

- Lopez Martin J., Batta A., Ramirez-Ruiz E., Martinez I., Samsing J., 2019, [ApJ](#), **877**, 56
- Luo L., Katz B., Dong S., 2016, [MNRAS](#), **458**, 3060
- Madau P., Dickinson M., 2014, [ARA&A](#), **52**, 415
- Mainetti D., Lupi A., Campana S., Colpi M., Coughlin E. R., Guillochon J., Ramirez-Ruiz E., 2017, [A&A](#), **600**, A124
- Manukian H., Guillochon J., Ramirez-Ruiz E., O’Leary R. M., 2013, [ApJ](#), **771**, L28
- Mardling R. A., 2008, in Aarseth S. J., Tout C. A., Mardling R. A., eds, , Vol. 760, The Cambridge N-Body Lectures. p. 59, [doi:10.1007/978-1-4020-8431-7\\_3](#)
- Mardling R. A., 2013, [MNRAS](#), **435**, 2187
- Mardling R., Aarseth S., 1999, Dynamics and Stability of Three-Body Systems. Springer Netherlands, Dordrecht, pp 385–392, [doi:10.1007/978-94-015-9221-5\\_38](#)
- Mardling R. A., Aarseth S. J., 2001, [MNRAS](#), **321**, 398
- Margutti R., et al., 2019, [ApJ](#), **872**, 18
- Marín-Franch A., et al., 2009, [ApJ](#), **694**, 1498
- Martin D. C., et al., 2005, [ApJ](#), **619**, L1
- Martinez M. A. S., et al., 2020, [ApJ](#), **903**, 67
- Matthews D., et al., 2023, [Research Notes of the American Astronomical Society](#), **7**, 126
- McCulloch W. S., Pitts W., 1943, The bulletin of mathematical biophysics, **5**, 115
- McKernan B., et al., 2018, [ApJ](#), **866**, 66
- Metzger B. D., 2022, [ApJ](#), **932**, 84
- Michaely E., Perets H. B., 2016, [MNRAS](#), **458**, 4188
- Michaely E., Perets H. B., 2019, [MNRAS](#), **484**, 4711
- Michaely E., Perets H. B., 2020, [MNRAS](#), **498**, 4924
- Michaely E., Ginzburg D., Perets H. B., 2016, [arXiv e-prints](#), p. [arXiv:1610.00593](#)
- Michell J., 1767, Philosophical Transactions of the Royal Society of London Series I, **57**, 234
- Mikkola S., 1983, [MNRAS](#), **203**, 1107

- Moe M., Di Stefano R., 2017, [ApJS](#), **230**, 15
- Morscher M., Pattabiraman B., Rodriguez C., Rasio F. A., Umbreit S., 2015, [ApJ](#), **800**, 9
- Muller P., 1955, *Bulletin Astronomique*, **20**, 145
- Naoz S., 2016, [ARA&A](#), **54**, 441
- Newall H. F., 1899, *The Observatory*, **22**, 436
- O'Leary R. M., Kocsis B., Loeb A., 2009, [MNRAS](#), **395**, 2127
- Ofek E. O., et al., 2021, [ApJ](#), **922**, 247
- Ohlmann S. T., Röpke F. K., Pakmor R., Springel V., Müller E., 2016a, [MNRAS](#), **462**, L121
- Ohlmann S. T., Röpke F. K., Pakmor R., Springel V., 2016b, [ApJ](#), **816**, L9
- Ohlmann S. T., Röpke F. K., Pakmor R., Springel V., 2017, [A&A](#), **599**, A5
- Ondratschek P. A., Röpke F. K., Schneider F. R. N., Fendt C., Sand C., Ohlmann S. T., Pakmor R., Springel V., 2022, [A&A](#), **660**, L8
- Paczynski B., 1971, [ARA&A](#), **9**, 183
- Paczynski B., 1976, in Eggleton P., Mitton S., Whelan J., eds, Vol. 73, *Structure and Evolution of Close Binary Systems*. p. 75
- Pakmor R., Kromer M., Taubenberger S., Springel V., 2013, [ApJ](#), **770**, L8
- Pakmor R., Springel V., Bauer A., Mocz P., Munoz D. J., Ohlmann S. T., Schaal K., Zhu C., 2016, [MNRAS](#), **455**, 1134
- Pakmor R., Zenati Y., Perets H. B., Toonen S., 2021, [MNRAS](#), **503**, 4734
- Pakmor R., et al., 2022, [MNRAS](#), **517**, 5260
- Paxton B., Bildsten L., Dotter A., Herwig F., Lesaffre P., Timmes F., 2011, [ApJS](#), **192**, 3
- Pechetti R., et al., 2022, [ApJ](#), **924**, 48
- Pedregosa F., et al., 2011, *Journal of Machine Learning Research*, **12**, 2825
- Pejcha O., Antognini J. M., Shappee B. J., Thompson T. A., 2013, [MNRAS](#), **435**, 943
- Perets H. B., Badenes C., Arcavi I., Simon J. D., Gal-yam A., 2011, [ApJ](#), **730**, 89
- Perets H. B., Li Z., Lombardi James C. J., Milcarek Stephen R. J., 2016, [ApJ](#), **823**, 113

- Perley D. A., et al., 2021, [MNRAS](#), 508, 5138
- Peters P. C., 1964, [Physical Review](#), 136, 1224
- Petrovich C., Antonini F., 2017, [ApJ](#), 846, 146
- Podsiadlowski P., Rappaport S., Han Z., 2003, [MNRAS](#), 341, 385
- Portegies Zwart S. F., McMillan S. L. W., 2000, [ApJ](#), 528, L17
- Portegies Zwart S. F., Verbunt F., Ergma E., 1997, [A&A](#), 321, 207
- Portegies Zwart S. F., Boekholt T. C. N., Por E. H., Hamers A. S., McMillan S. L. W., 2022, [A&A](#), 659, A86
- Prentice S. J., et al., 2018, [ApJ](#), 865, L3
- Press W. H., Teukolsky S. A., 1977, [ApJ](#), 213, 183
- Pursiainen M., et al., 2018, [MNRAS](#), 481, 894
- Raghavan D., et al., 2010, [ApJS](#), 190, 1
- Raidal M., Vaskonen V., Veermäe H., 2017, [J. Cosmology Astropart. Phys.](#), 2017, 037
- Rantala A., Pihajoki P., Mannerkoski M., Johansson P. H., Naab T., 2020, [MNRAS](#), 492, 4131
- Reines A. E., 2022, [Nature Astronomy](#), 6, 26
- Reipurth B., Clarke C., 2001, [AJ](#), 122, 432
- Rizzuto F. P., Naab T., Rantala A., Johansson P. H., Ostriker J. P., Stone N. C., Liao S., Irodotou D., 2023, [MNRAS](#), 521, 2930
- Rodriguez C. L., Chatterjee S., Rasio F. A., 2016, [Phys. Rev. D](#), 93, 084029
- Rosenblatt F., 1958, [Psychological Review](#), pp 65–386
- Ryu T., Krolik J., Piran T., Noble S. C., 2020a, [ApJ](#), 904, 98
- Ryu T., Krolik J., Piran T., Noble S. C., 2020b, [ApJ](#), 904, 99
- Ryu T., Krolik J., Piran T., Noble S. C., 2020c, [ApJ](#), 904, 100
- Ryu T., Krolik J., Piran T., Noble S. C., 2020d, [ApJ](#), 904, 101
- Ryu T., Perna R., Wang Y.-H., 2022, [MNRAS](#), 516, 2204



- Ryu T., Perna R., Pakmor R., Ma J.-Z., Farmer R., de Mink S. E., 2023a, *MNRAS*, **519**, 5787
- Ryu T., Valli R., Pakmor R., Perna R., de Mink S. E., Springel V., 2023b, *MNRAS*, **525**, 5752
- Ryu T., Seoane P. A., Taylor A. M., Ohlmann S. T., 2024a, *MNRAS*,
- Ryu T., de Mink S. E., Farmer R., Pakmor R., Perna R., Springel V., 2024b, *MNRAS*, **527**, 2734
- Ryu T., McKernan B., Ford K. E. S., Cantiello M., Graham M., Stern D., Leigh N. W. C., 2024c, *MNRAS*, **527**, 8103
- Salaris M., Weiss A., 2002, *A&A*, **388**, 492
- Sana H., et al., 2012, *Science*, **337**, 444
- Sand C., Ohlmann S. T., Schneider F. R. N., Pakmor R., Röpke F. K., 2020, *A&A*, **644**, A60
- Sandage A. R., 1953, *AJ*, **58**, 61
- Sandage A., et al., 1966, *ApJ*, **146**, 316
- Sasaki M., Suyama T., Tanaka T., Yokoyama S., 2016, *Phys. Rev. Lett.*, **117**, 061101
- Schmidt P., Ohme F., Hannam M., 2015, *Phys. Rev. D*, **91**, 024043
- Schneider F. R. N., Ohlmann S. T., Podsiadlowski P., Röpke F. K., Balbus S. A., Pakmor R., Springel V., 2019, *Nature*, **574**, 211
- Schödel R., Merritt D., Eckart A., 2009, *A&A*, **502**, 91
- Secchi A., 1866, *Astronomische Nachrichten*, **68**, 63
- Secunda A., Bellovary J., Mac Low M.-M., Ford K. E. S., McKernan B., Leigh N. W. C., Lyra W., Sándor Z., 2019, *ApJ*, **878**, 85
- Seppinsky J. F., Willems B., Kalogera V., Rasio F. A., 2007, *ApJ*, **667**, 1170
- Shevchenko I. I., 2017, The Lidov-Kozai Effect - Applications in Exoplanet Research and Dynamical Astronomy. Vol. 441, doi:10.1007/978-3-319-43522-0,
- Sigurdsson S., Hernquist L., 1993, *Nature*, **364**, 423
- Silber K., Tremaine S., 2017, *ApJ*, **836**, 39
- Sądowski A., Narayan R., McKinney J. C., Tchekhovskoy A., 2014, *MNRAS*, **439**, 503

- Smartt S. J., et al., 2018, *The Astronomer's Telegram*, [11727](#), 1
- Snow T. P. J., Marlborough J. M., 1976, *ApJ*, [203](#), L87
- Spera M., Mapelli M., Giacobbo N., Trani A. A., Bressan A., Costa G., 2019, *MNRAS*, [485](#), 889
- Springel V., 2010, *MNRAS*, [401](#), 791
- Stearns C. L., 1936, *AJ*, [45](#), 120
- Stein S. K., Elsner T., 1977, *Mathematics Magazine*, 50, 160
- Stone N. C., Leigh N. W. C., 2019, *Nature*, [576](#), 406
- Stone N. C., Metzger B. D., Haiman Z., 2017a, *MNRAS*, [464](#), 946
- Stone N. C., Küpper A. H. W., Ostriker J. P., 2017b, *MNRAS*, [467](#), 4180
- Stone N. C., Kesden M., Cheng R. M., van Velzen S., 2019, *General Relativity and Gravitation*, [51](#), 30
- Tagawa H., Haiman Z., Kocsis B., 2020, *ApJ*, [898](#), 25
- Tanvir N. R., Levan A. J., Fruchter A. S., Hjorth J., Hounsell R. A., Wiersema K., Tunnicliffe R. L., 2013, *Nature*, [500](#), 547
- Thompson T. A., 2011, *ApJ*, [741](#), 82
- Timmes F. X., Swesty F. D., 2000, *ApJS*, [126](#), 501
- Tokovinin A. A., 1997, *A&AS*, [124](#), 75
- Tokovinin A., 2017, *ApJ*, [844](#), 103
- Tokovinin A., 2018a, *VizieR Online Data Catalog*, [p. J/ApJS/235/6](#)
- Tokovinin A., 2018b, *ApJS*, [235](#), 6
- Tonry J. L., et al., 2018, *PASP*, [130](#), 064505
- Toonen S., Hamers A., Portegies Zwart S., 2016, *Computational Astrophysics and Cosmology*, [3](#), 6
- Tory M., Grishin E., Mandel I., 2022, *Publ. Astron. Soc. Australia*, [39](#), e062
- Udalski A., Szymański M. K., Szymański G., 2015, *Acta Astron.*, [65](#), 1
- Valtonen M., Karttunen H., 2006, *The Three-Body Problem*

- 
- Voges W., et al., 1999, [A&A](#), **349**, 389
- Volonteri M., Habouzit M., Colpi M., 2021, [Nature Reviews Physics](#), **3**, 732
- Voss R., Gilfanov M., 2007, [MNRAS](#), **380**, 1685
- Vynatheya P., Hamers A. S., 2022, [ApJ](#), **926**, 195
- Vynatheya P., Hamers A. S., Mardling R. A., Bellinger E. P., 2022, [MNRAS](#), **516**, 4146
- Vynatheya P., Ryu T., Pakmor R., de Mink S. E., Perets H. B., 2023a, [arXiv e-prints](#), p. [arXiv:2310.14852](#)
- Vynatheya P., Mardling R. A., Hamers A. S., 2023b, [MNRAS](#), **525**, 2388
- Walker M. F., 1954, [PASP](#), **66**, 230
- Wang Y.-H., Perna R., Armitage P. J., 2021, [MNRAS](#), **503**, 6005
- Webbink R. F., 1984, [ApJ](#), **277**, 355
- Weinberger R., Springel V., Pakmor R., 2020, [ApJS](#), **248**, 32
- Weisskopf M. C., Tananbaum H. D., Van Speybroeck L. P., O'Dell S. L., 2000, in Truemper J. E., Aschenbach B., eds, *Society of Photo-Optical Instrumentation Engineers (SPIE) Conference Series Vol. 4012, X-Ray Optics, Instruments, and Missions III*. pp 2–16 ([arXiv:astro-ph/0004127](#)), [doi:10.1117/12.391545](#)
- Wen L., 2003, [ApJ](#), **598**, 419
- Wheeler J. C., Hansen C. J., 1971, [Ap&SS](#), **11**, 373
- Xin C., Haiman Z., Perna R., Wang Y., Ryu T., 2024, [ApJ](#), **961**, 149
- Yao Y., et al., 2022, [ApJ](#), **934**, 104
- Zauderer B. A., et al., 2011, [Nature](#), **476**, 425
- de Kool M., 1990, [ApJ](#), **358**, 189
- de Mink S. E., Mandel I., 2016, [MNRAS](#), **460**, 3545
- van den Berk J., Portegies Zwart S. F., McMillan S. L. W., 2007, [MNRAS](#), **379**, 111
- van den Heuvel E. P. J., 1976, in Eggleton P., Mitton S., Whelan J., eds, *Vol. 73, Structure and Evolution of Close Binary Systems*. p. 35
- von Zeipel H., 1910, [Astronomische Nachrichten](#), **183**, 345



# Acknowledgements

First off, I want to give a big shoutout to MPA for granting me this incredible PhD opportunity and to Adrian for being an awesome supervisor. Huge thanks also go to Selma, who stepped in as my supervisor when Adrian had to move on from MPA. And of course, I cannot forget to thank Ruediger and Taeho for helping me make a smooth transition and always being there when I needed help at work. My time at MPA was made all the better by the supportive atmosphere.

Next up, a massive thank you to my parents and my sister, Pooja. Even though we have not all been in the same place together since before I started my PhD, their unwavering support has been my rock. I hope we can all catch up and enjoy during your Europe trip this year!

Thirdly, I am extremely grateful to all my friends in Munich – hanging out with you lot was the absolute best. Mahathi, Vijayaditya, Meghana, Vibha, Kanishk, Avani, Muhunden, Laia, Mrinmoy, Abhilash, Burak, Nandini, Raghav, Jason, Faik, Vickrant, Prateek, Rajdeep – you all made my time in Munich unforgettable. I really loved having many of you as my travel buddies, or just sitting around in a circle and chatting about life and all sorts of things. To my friends outside Munich – Srikrishnaa, Ashwin, Kasturi, Tannu, Anant, Sweta, Anupama, Arijeet, Nirmitee – thanks for staying connected and sharing your adventures from around the world.

Lastly, a massive thanks to all my friends and colleagues at MPA (and MPE) – you made the grueling journey in academia much more bearable. From Friday WAW beers to bouldering and board game sessions, weekend hikes, and attending Oktoberfest, you made Munich feel like home. Abinaya, Hitesh, Anshuman, Geza, Beatriz, Monica, Miha, Parth, Fulvio, Ruggero, Soumya, Andrija, Vyoma, Teresa, Jing-Ze, and many others – thank you. Munich, with its lively culture, proximity to the Alps, and fantastic public transport, will forever hold a special place in my heart. Being right in the center of Europe made exploring the continent quite easy. Thank you all for making my time in Munich unforgettable!